Techniques for Precision Interferometry in Space

Ewan D Fitzsimons

School of Physics and Astronomy,
University of Glasgow

Presented as a thesis for the degree of Ph.D.
in the University of Glasgow, University Avenue,
Glasgow G12 8QQ

December 16, 2010

Contents

List of Figures

List of Tables

Acknowledgements

First and foremost, I must express my deepest gratitude to Harry Ward for giving me the opportunity to work on this project. Searching for a Ph.D. was not an especially trivial activity and I feel extremely fortunate to have found not only a project that I enjoy immensely, but a group of people who are great to work with. Slowly but surely the transfer of his wealth of experience *via* Osmosis is converting me into something approaching a physicist, even if his attempts at transferring his equally impressive mastery of English grammar and punctuation have been less successful.

I am also hugely indebted to Dave Robertson. His perennially (and perhaps foolishly) open office door has meant he was always there to answer the hard questions, and discuss the multifaceted horrors of geometry (especially hexagons).

I must also say a huge thank you to Christian Killow: fellow caffeine addict, possessor of 'μm fingers' and the only person I've ever met for whom the graph of *alcohol consumed* against *ability at pool* has a positive gradient. His teachings in the ways of all things bonding, optics and interferometry were invaluable, even if the result was ridiculously late nights in the clean room together listening to "banging tunes" whilst building the flight model OBI.

Mike Perreur-Lloyd has been a huge help, providing much needed engineering expertise, and is always willing to entertain one of my weirder ideas, although his attempts at dampening my enthusiasm for over-engineering have yet to yield fruit! His schooling in the ways of *Solidworks* has also been invaluable.

Thank you to Johanna Bogenstahl who, with her crazy ramblings and love of post-work pints, never made the office a dull place and was always on hand to help and offer advice about bonding or optics. Also, thank you to Alasdair Taylor who recently jointed the group and was involved for the LISA work. And a big thanks to Russell Jones, the ever cheery odd-one-out in the office who must suffer our regular meetings and telecons.

Thank you to Jim Hough and Sheila Rowan for ensuring that the IGR is an enjoyable and rewarding place to work.

Thank you to Alan Latta, Neil Robertson, Steven Craig, Colin Craig and Steven O'Shea who have all helped me at one point or another over the past few years. Thanks also to Jean Greig, who somehow always manages to process my expenses claims with speedy efficiency (even when Harry had one of the receipts), and was a huge help after I was "volcanoed" in Paris.

I would also like to say thanks to everyone in the IGR and wider department that I know who have made it an enjoyable place to work, with random coffee time chats on subjects as diverse (and crazy) as hoovering up black holes and the merits (or lack thereof) of the film *Sunshine*.

I wish to acknowledge the support of the STFC (formally PPARC) and ESA for supporting me during the course of my Ph.D.

Finally, a big thank you to all my friends and family who have encouraged me to this point. Oh, and I should also say a huge thank you to Sara, not least for

your surprisingly benign attitude towards being ignored for the last 6 months whilst I was writing this!

Acronyms

Acronym	Definition
AM	Amplitude Modulation
AOM	Acousto-Optic Modulator
AU	Astronomical Unit
BS	Beamsplitter
CAD	Computer Aided Design
CCD	Charge-Coupled Device
CMM	Coordinate Measurement Machine
CNC	Computer Numerical Control
CQP	Coupled Quadrant photodiode Pair
DFACS	Drag Free and Attitude Control System
DMU	Data Management Unit
DWS	Differential Wavefront Sensing
EM	Engineering Model
ESA	European Space Agency
FIOS	Fibre Injector Optical Subassembly
FM	Flight Model
GW	Gravitational Wave

Acronym	**Definition**
LIGO	Laser Interferometer Gravitational wave Observatory
LISA	Laser Interferometer Space Antenna
LTP	LISA Technology Package
NASA	National Aeronautics and Space Administration
OB	Optical Bench
OBF	Optical Bench reference Frame
OBI	Optical Bench Interferometer
PAAM	Point Ahead Angle Mechanism
PBS	Polarising Beamsplitter
QPD	Quadrant Photodiode
rf	Radio Frequency
Rx	Received
TM	Test Mass
TNO	Netherlands Institute for Applied Geoscience
Tx	Transmitted

Preface

This thesis is an account of research carried out between October 2006 and September 2010, developing precision interferometry techniques intended for use in spaceborne gravitational wave detectors, and has been composed entirely by the author.

As with many projects in modern physics research, the work described in this thesis is part of a large international collaboration. In Glasgow, this collaboration consists of H. Ward, D. I. Robertson, C. J. Killow, M. Perreur-Lloyd, J. Hough, S. Rowan and the author. J. Bogenstahl was involved for the work relating to LISA Pathfinder, and A. Taylor was involved in the more recent LISA work.

Chapter 1 introduces the concept of gravitational radiation and discusses various postulated sources of gravitational waves, as well as giving an overview of gravitational wave detectors. This work is derived from published literature.

Chapter 2 introduces LISA, a planned space based gravitational wave detector, and its precursor technology demonstrator mission LISA Pathfinder. The operation of LISA Pathfinder is described in detail, with emphasis on the design and required performance of the interferometer. This work is derived from published literature.

Chapter 3 describes the development of a system for measuring the position and direction of a laser beam in free space, called the calibrated quadrant photodiode pair (CQP). The CQP was initially conceived of by the LISA team members. The calibration procedure was developed by D. I. Robertson and the author. The investigations into the CQP calibration issues were carried out by the author, with assistance from D. I. Robertson, H. Ward and J. Hough. The diffraction sensor was developed and constructed by the author, and the comparison between the diffraction sensor and the CQP led by the author with assistance from D. I. Robertson.

Chapter 4 describes methods for precision placement of optics to form a rigid ultra-stable interferometer. The precision actuator adjustment and template bonding methods were originally developed during prior experiments carried out at Glasgow. The template optimisation method was developed by the author with assistance from D. I. Robertson. Methods of integrating the precision alignment method with the CQP, especially alignment of the CQP to a nominal beam, were developed by the author with input from D. I. Robertson.

Chapter 5 describes the construction and testing of the flight model interferometer for LISA Pathfinder. The FIOS was developed by the entire LISA team in Glasgow. The flight model FIOS were constructed by C. J. Killow. The optical components were catalysis bonded to the OBI by C. J. Killow and the author. CMM programs for alignment of the CQP, control over dummy test mass mirrors and beam measurement were written and executed by the author and D. I. Robertson. The as-built Optocad model was developed by the author. Modelling and simulations for positioning of dummy test mass mirrors and components to facilitate path length matching were carried out by the author. The photodiodes were manufactured by the University of Birmingham and integrated onto the OBI by G. Dixon, D. Smith, J. Bryant, D. I.

Robertson and the author. Testing of the OBI was carried out by the author, C. J. Killow, D. I. Robertson and H. Ward.

Chapter 6 describes the DWS calibration of the flight model OBI. The calibration procedure was developed and performed by the author and D. I. Robertson. The read-out electronics and phasemeter were designed by H. Ward.

Chapter 7 discusses LISA in more detail, and describes the measurement principle with emphasis on the interferometer; this section is derived from published literature. The derivation of top level requirements from the LISA mission formulation study to the interface requirements on the optical bench was carried out by D. Weise. The concept for the LISA redundant fibre injector system was developed by the entire LISA team in Glasgow.

The analysis of the interface requirements in terms of OB alignment and manufacturability was carried out by the author. The optical design and optical model of the prototype LISA OB was developed by the author. The alignment plan and consideration of alignment tolerances was derived by the author.

Chapter 8 presents an outlook for future research based on the work presented.

Summary

Gravitational waves are an important prediction of Einstein's General theory of Relativity. Derived as a solution to the Einstein field equations, they are predicted to be produced in systems where there is an asymmetric acceleration of matter, and exist as a time varying quadrupolar distortion in spacetime.

Due to the rich variety of scientifically interesting astrophysical sources predicted to be producing gravitational radiation, there is significant international effort directed towards their detection. A large network of ground based interferometric detectors is in operation, with upgrades to increase sensitivity already in progress. They operate on the principle of measuring the time varying displacement in the interferometer path length an incident gravitational wave will induce. However, the predicted amplitude of gravitational waves requires the measurement to be made over several kilometres with a displacement sensitivity of less than $10^{-18}\,\mathrm{m}/\sqrt{\mathrm{Hz}}$.

Ground based detectors operate in the $\sim 10 - 10000\,\mathrm{Hz}$ region, and are fundamentally limited at the low frequency end by the noisy gravitational environment of the Earth. To enable detection of low frequency sources, LISA - the Laser Interferometer Space Antenna - is a planned mission to place an interferometric gravitational wave detector in space, sensitive to gravitational waves in the $0.1 - 1000\,\mathrm{mHz}$ region. Consisting of a triangular constellation of

three spacecraft, LISA will aim to detect gravitational waves by monitoring the fluctuation in the separation between free-falling test masses over a baseline of 5 million kilometres with an accuracy of around $10\,\mathrm{pm}/\sqrt{\mathrm{Hz}}$.

To demonstrate that LISA technology, such as the ability to place test masses into a suitably quiet gravitational free-fall, is viable, a precursor mission - LISA Pathfinder - will launch in the next few years. LISA Pathfinder will monitor the relative displacement between two free-falling inertial test masses using an interferometer, with the goal of verifying that the required quality of free-fall is achievable in LISA. This work presented in this thesis relates to the development of interferometry for LISA Pathfinder and LISA, the construction of the LISA Pathfinder flight model interferometer, and initial work on developing the interferometer for LISA.

The interferometers required for LISA and LISA Pathfinder must be constructed to be durable enough to survive launch and stable enough to measure displacements of a few picometres at frequencies down to a few mHz. Further, to help minimise noise from sources such as residual jitter of the test masses, the beams which probe the test masses must be aligned to within $\pm 25\,\mu$m of the nominal reflection point. Using ultra low expansion substrates like Zerodur®, and attaching optical components with hydroxide catalysis bonding offers one solution which can provide the durability and stability required.

To achieve the accuracy of beam positioning, a system which allows measurement of absolute propagation direction of a laser beam was developed. Combined with a coordinate measuring machine, this allows the absolute position of a mm-scale laser beam to be measured with an accuracy of around $\pm 5\,\mu$m and $\pm 20\,\mu$rad. This system can operate in two modes: first as a measurement system allowing measurement of an existing beam; and secondly as a target, where it can be positioned to a desired theoretical (such as the nominal re-

flection point of a test mass) and a beam can be aligned onto it. Combined with a method of precision adjusting optical components at the sub-micron and microradian level prior to hydroxide catalysis bonding, it enables absolute alignment of ultra-stable interferometers to micron level.

Using these techniques, the flight model interferometer for LISA Pathfinder was successfully constructed to meet the alignment and performance requirements. The control system that will maintain the test masses in near free-fall requires a very accurate measure of the attitude of the test masses. This measurement will be provided by the interferometer using differential wavefront sensing (DWS). The flight model interferometer was calibrated to establish the coupling factors between the DWS read-out and the attitude of the test mass to ensure maximum performance of the control system.

Building upon the experience gained in developing and building the LISA Pathfinder interferometer, a prototype of the LISA optical bench is in development. The LISA interferometer is significantly more complicated than that of LISA Pathfinder. Some of its features include: imaging systems to minimise coupling of beam tilt to displacement noise; a precision beam expander to generate a beam appropriate for the telescope; a redundant fibre injector system, creating two beams collinear to within a few microns and $10 - 20\,\mu$rad; and polarisation optics for beam steering. The development and current state of the design for the prototype optical bench is presented, along with an overview of its features.

Chapter 1

Introduction

1.1 Predicting the existence of gravitational waves

In 1915, Albert Einstein published his General theory of Relativity, a new theory of gravitation which explained it as a result of the curvature of spacetime. This relationship between gravity and curvature is derived mathematically through the Einstein field equations [1]. If we consider a spacetime in which there is a weak gravitational field, then the relationship between gravitation and curvature means that this spacetime must be nearly flat (*i.e.* almost described by the Minkowski metric of Special Relativity). If we represent this deviation from a flat spacetime by the metric perturbation $h_{\mu\nu}$, then working from the Einstein field equations it is possible to derive a solution [2] which will take the form

$$\left(\nabla^2 - \frac{1}{c^2}\frac{\partial^2}{\partial t^2}\right) h_{\mu\nu} = 0 \tag{1.1}$$

This is an important result. Equation 1.1 is a second order linear partial differential equation and has the same mathematical form as a wave equation. It shows that in General Relativity, solutions are possible which predict the existence of waves propagating through spacetime at the speed of light - these are gravitational waves and they are an important prediction of General Relativity.

The form of $h_{\mu\nu}$ can tell us about the exact physical nature of gravitational waves. The simplest solution to this wave equation that does not have zero luminosity is quadrupolar in nature, this leads to the prediction that gravitational waves will be quadrupolar plane waves with two polarisation states, h_+ and $h_\times$ which are 45° apart [2].

The real-world effect of a gravitational wave is to distort the local spacetime as it passes. This is best illustrated by considering a circular ring of particles, as illustrated in Figure 1.1. This shows how such a ring of particles will be effected as a gravitational wave passes, being stretched and squashed in orthogonal directions, for both polarisations.

The quadrupolar nature of gravitational waves also tells us something about their production. General Relativity shows that any acceleration of mass will produce a metric perturbation like $h_{\mu\nu}$, which will then go on to propagate as a gravitational wave. However, there is no quadrupolar contribution from spherically (or cylindrically) symmetric mass distributions (such as the rotation of a perfect sphere or disk), therefore we can say that only asymmetric accelerations of matter will produce a gravitational wave.

The Einstein field equations can also tell us about the strength of gravitational

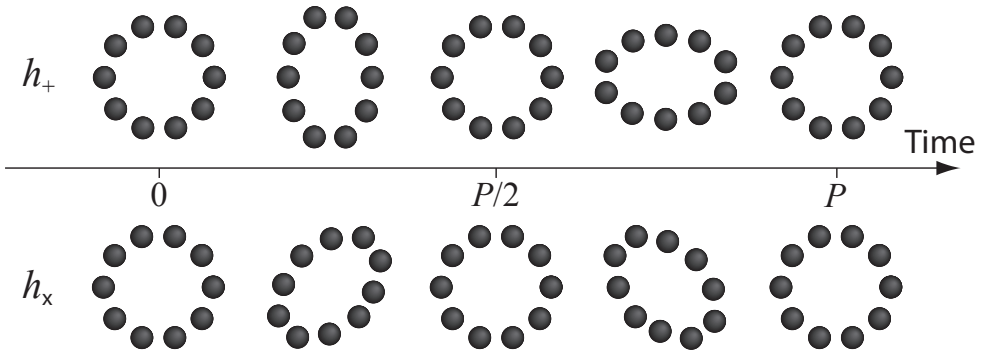

Figure 1.1: *Diagram showing the time varying effect of a gravitational wave, of period P, incident on a ring of particles. The direction of propagation of the wave is normal to the plane of the page.*

radiation by considering the medium in which they propagate. One of the important results of General Relativity was the realisation that the curvature of spacetime and the mass-energy content of spacetime are linked [2]. This is described mathematically in General Relativity by the equation

$$\mathbf{T} = \frac{c^4}{8\pi G}\mathbf{G}, \tag{1.2}$$

where $\mathbf{T}$ is the stress energy tensor, describing the mass-energy content of spacetime and $\mathbf{G}$ is the Einstein curvature tensor which describes the curvature of spacetime. What is interesting is that this equation can be regarded as analogous to Hookes law: $F = kx$. In this case, the constant relating $\mathbf{T}$ and $\mathbf{G}$ would be the 'spring constant' of spacetime. However, $c^4/8\pi G$ is $\sim 5 \times 10^{42}$, which indicates that spacetime is a very stiff medium. This tells us two important things, firstly that vast amounts of energy are required to produce gravitational radiation and secondly that the amplitude will be very small. The consequence is that the only practical sources of gravitational waves are astrophysical ones [3].

1.2 Gravitational wave astronomy

In the time since the formulation of General Relativity a wealth of potential sources of gravitational waves has been postulated, studied and modelled in great detail. Due to the weak interaction of gravitational radiation with matter, many events that are otherwise obscured in the electromagnetic spectrum (for example, due to interactions with charged particles) are potentially visible with gravitational waves, including the ability to see past the surface of last scattering into the very early universe. A full discussion of sources of gravitational waves is beyond the scope of this thesis and can be found in [3, 4, 5, 6]. What follows in this section is a brief overview intended to provide a context of the underlying physics, astrophysics and cosmology that drives the development of gravitational wave detectors.

Broadly, there are four main classes of sources: binary systems, asymmetrical spinning sources, bursts and stochastic backgrounds.

Binary systems are potentially the most numerous sources. Typically, any binary system of compact objects (such as neutron stars, stellar mass black holes and white dwarfs) will be a source of gravitational waves. These systems are continuous sources of gravitational radiation, the production of which takes energy away form the system, eventually leading to a merger event. Perhaps of even more interest are gravitationally bound super massive black holes. A binary pair of super massive black holes, for example in a galaxy merger event, will produce large amplitude gravitational waves in the mHz region, potentially providing a wealth of information about these extremely interesting sources. EMRIs - extreme mass-ratio inspirals - are another interesting binary system where a small star or compact object is gradually spiraling towards a super massive black hole. These systems provide excellent test-beds for theories on

strong gravitational curvature.

Any spinning system which is not perfectly symmetrical will emit gravitational radiation. This raises the possibility that spinning neutron stars could be interesting sources of gravitational waves. Indeed, current detectors are already placing upper limits on the ellipticity of known pulsars such as the Crab [7].

Burst sources, like core collapse supernova, are possible sources for an initial detection by ground based detectors. While an ideal supernova would be perfectly spherically symmetrical and so not produce gravitational radiation, 'real' supernova are likely to be anything but symmetrical producing significant amounts of gravitational radiation. Additionally, the radiation would emanate directly from the core collapse region where electromagnetic techniques cannot penetrate, providing a never before seen view of such an event.

A stochastic background of gravitational waves from the Big Bang is one exciting possibility. The detection of such a background would potentially be one of the most important observations in astronomy, as it would provide direct experimental evidence of the Big Bang, and present unparalleled information as to the nature of the early universe.

These sources are all ones that have been predicted and studied. There is, however, a fifth classification which is potentially of even greater interest; the unexpected sources. Our current understanding of the universe is mainly limited to measurements and observations in the electromagnetic spectrum. Given that we know over 90 % of the universe - the 'dark' universe - is potentially undetectable with EM radiation, the possibilities of detecting yet to be imagined structures in the dark universe with gravitational waves are intriguing.

Even then, it is very possible that there are as yet undiscovered sources of

gravitational waves that are visible with electromagnetic instruments as well, the discovery of which in the gravitational spectrum can inform on their investigation by other means.

1.3 Detection of gravitational waves

Due to the extremely stiff nature of spacetime predicted in equation 1.2, the amplitudes from even the strongest sources of gravitational waves are extremely small. Since the effect of a gravitational wave is to deform spacetime, as shown in Figure 1.1, the amplitude is best expressed in terms of a physical strain, $h = \delta l/l$ [8]. In the figure, the effect of the passing gravitational wave was greatly exaggerated, with an amplitude of $\sim h = 0.5$. In reality, the predicted amplitude of gravitational waves received on Earth from a typical source (such as a binary neutron star system) is 10^{-21} [5]. Measuring a strain of this magnitude presents an enormous technical challenge, and a direct detection of a gravitational wave has yet to be made. The current generation of ground-based detectors are very near to the sensitivity required, but the event rate for many observable phenomena (such as a galactic supernova) is of the order 1 per decade or less. Next generation detectors such as Advanced LIGO will increase sensitivity even further, to the point where the event rate for some sources is expected to be of the order of several per year [9].

Although no direct detection has been made, there is compelling indirect evidence for the existence of gravitational waves. In 1974, Russell Hulse and Joseph Taylor discovered a binary pulsar system (PSR B1913+16), the first to be discovered [10]. Measurements of the orbital decay of the system (now spanning over 30 years) match the predicted theoretical energy loss due to emission of gravitational waves as predicted by General Relativity to within

0.2% [11]. Hulse and Taylor were jointly awarded the 1993 Nobel Prize in Physics for their discovery.

1.3.1 Detection principles

The first gravitational wave detectors to be built were resonant bar detectors, designed by Joseph Weber over 50 years ago [12, 13]. Much of the early work was in this field, and there are still bar detectors operating today. The principle is to have a large, typically aluminium, cylindrical bar. The bar is designed such that its longitudinal resonant frequency is close to the frequency of a gravitational wave source of interest. When gravitational waves at the resonant frequency pass through the bar, they will excite the resonant mode and this can be detected with transducers attached to the bar.

In the 1970's, prototype gravitational wave detectors based on Michelson interferometers began to appear. If we imagine the two end mirrors of the interferometer as two of the particles in the ring depicted in Figure 1.1, then a passing gravitational wave will induce a time varying change in the *relative* path lengths of the two arms; this is detectable as a signal in the interference pattern. Interferometric detectors have an advantage over resonant bar detectors in that such an instrument has the potential to be broadband, rather than limited to narrow frequency ranges. Today, the vast majority of international effort to develop ground based instruments is focused on Michelson-type detectors. A review of the history of ground based detectors of all types and future prospects can be found in [14].

The sensitivity required in these detectors is extremely high: for a typical gravitational wave strain of 10^{-21}, an interferometer with an arm length of 1 km would have to be sensitive to length changes of $10^{-19}\,\mathrm{m}/\sqrt{\mathrm{Hz}}$. This sets

the scale and complexity involved in such a detector.

1.3.2 Ground based interferometric detectors

Following the successful short baseline prototypes, the current generation of long baseline detectors was constructed around the world. The network is well established and some recent scientific results from the detectors can be found in [3, 15, 16] and references therein.

The current detectors in operation around the world are:

LIGO, the Laser Interferometer Gravitational wave Observatory, consists of three interferometers located in the USA. There is a 4 km baseline detector in Livingston, Louisiana, and a 4 km and a 2 km detector (in a shared vacuum system) in Hanford, Washington.

VIRGO is a French-Italian collaboration operating a 3 km baseline interferometer located near Pisa in Italy.

GEO600 is a British-German collaboration with a 600 m baseline detector located near Hannover in Germany.

TAMA300 is a Japanese detector with 300 m baseline arms, located near Tokyo.

LIGO, VIRGO and GEO are scheduled to begin upgrades to second generation detectors in the near future, further increasing sensitivity. Research has also started on a potential third generation detector, the Einstein Telescope, intended to be operating around 2025.

1.3.3 Spaceborne detectors

The primary noise source in the ground based interferometric detectors at low frequency is gravity gradient noise. Changes in the mass distribution in the vicinity of the interferometer will couple through gravitational attraction to the mirrors into the detector, and this is the limiting noise source for all the detectors below $\sim 10\,\mathrm{Hz}$.

This is unfortunate, because there are a great many interesting sources at low frequencies. Super massive black hole inspirals and mergers are significant sources of low frequency gravitational waves, as are the massive population of galactic compact binaries which will present themselves as a potentially unresolvable noise signal in the few mHz region. The low frequency region also presents the best possibility of directly detecting stochastic gravitational waves from the Big Bang. These sources are of great interest scientifically, but are well outside the range of a detector on Earth. In order to be able to detect such low frequency sources we need to move to an environment without gravity gradient noise and this requires going to space.

This is the idea behind LISA - the Laser Interferometer Space Antenna. LISA is a joint mission of the European Space Agency (ESA) and the National Aeronautics and Space Administration (NASA), with the goal of placing an interferometric gravitational wave detector in space, sensitive to gravitational waves of frequency $0.1 - 1000\,\mathrm{mHz}$ [17].

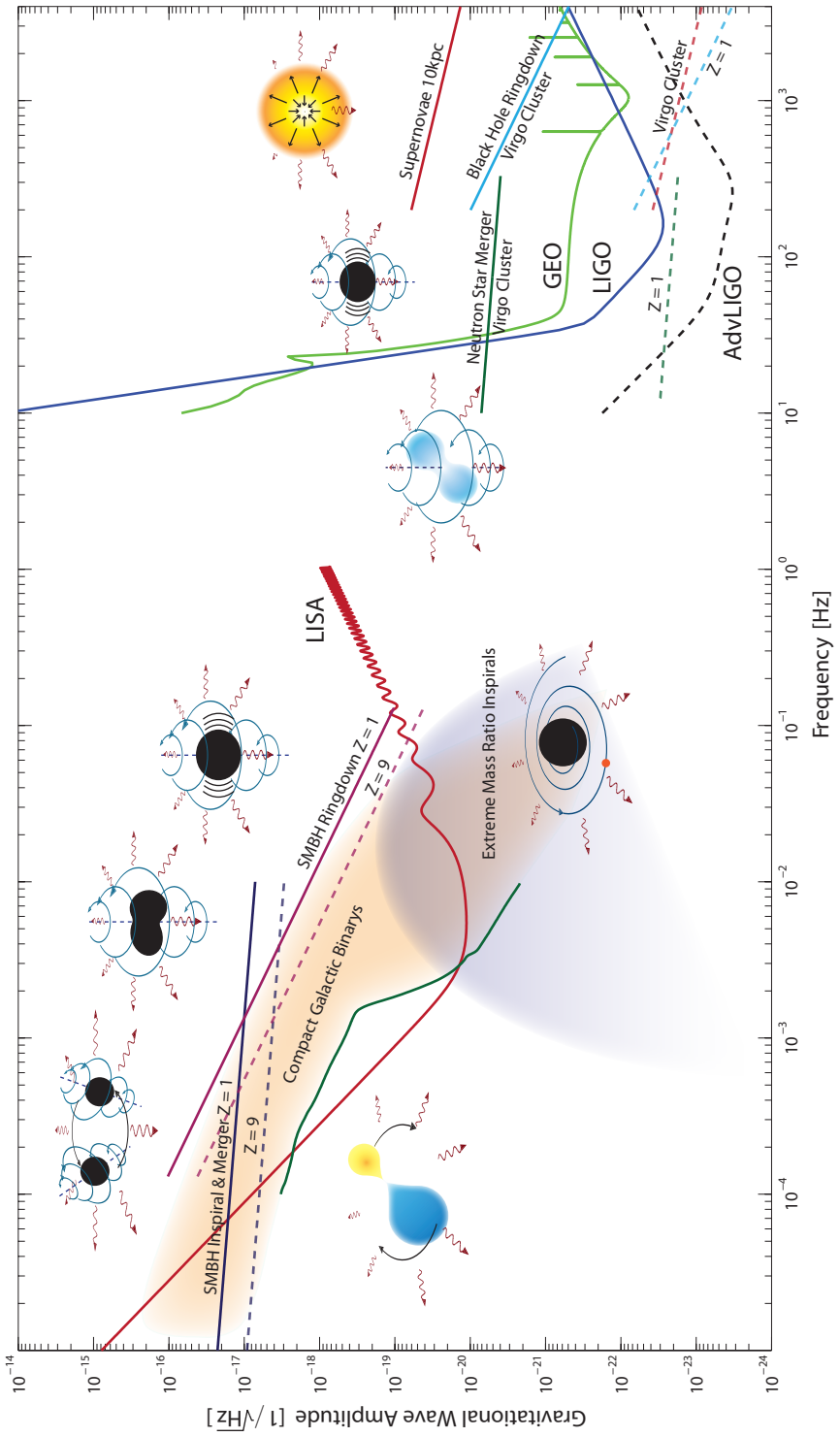

Figure 1.2: *Plot showing the sensitivities of ground and space based detectors, along with potential sources of gravitational waves. For source curves, solid lines represent upper limits, with dashed lines of the same colour representing equivalent sources at greater distances (as indicated). The plot is by the author, the source data are gathered from [18, 19, 20, 21, 22, 23]. An energy to GW coupling efficiency of* 10^{-3} *has been assumed.*

Chapter 2

Verifying the LISA measurement principle - LISA Pathfinder

2.1 LISA

LISA will consist of a constellation of three spacecraft, lying at the vertices of an equilateral triangle of side 5×10^9 m. As discussed in Chapter 1, a gravitational wave can be detected by looking for an induced oscillation in the separation of two points in space. In LISA each spacecraft will house two test masses, gold-platinum alloy cubes which will be maintained in near free-fall. These are analogous to the end mirrors in a ground-based detector, and their relative displacement will be measured between each of the spacecraft in the constellation using heterodyne interferometry [17]. The specifics of LISA are discussed in more detail in Chapter 7.

The scientific goal of LISA calls for a peak strain sensitively of $10^{-20}/\sqrt{\text{Hz}}$ at a few mHz. In order to meet this sensitivity, we must measure the relative displacement between two test masses, over the $5 \times 10^9\,\text{m}$ baseline to around $10\,\text{pm}/\sqrt{\text{Hz}}$. Further, the quality of the free-fall of the test masses must be such that the residual acceleration noise is $<\sim 3 \times 10^{-15}\,\text{m}\,\text{s}^{-2}/\sqrt{\text{Hz}}$. Demonstrating the free-fall requirement, especially, is extremely challenging on ground due to the presence of Earth's gravity. In order to prove that such sensitivity is realistically possible, the European Space Agency has commissioned a precursor mission, LISA Pathfinder [24, 25].

2.2 LISA Pathfinder

2.2.1 Mission concept

LISA Pathfinder is essentially a null experiment, demonstrating that two test masses can be placed in simultaneous geodesic motion and measured with the required precision and expected noise level. Compared with the noise performance required for LISA there is some relaxation and the frequency range has been relaxed to $1 - 30\,\text{mHz}$ for time and cost reasons [26]. Broadly, there are four main mission goals for LISA Pathfinder:

- demonstrate that a test mass can be placed into gravitational free fall with acceleration noise within one order of magnitude of that required for LISA, approximately $3 \times 10^{-14}\,\text{m}\,\text{s}^{-2}/\sqrt{\text{Hz}}$ at $1\,\text{mHz}$;
- demonstrate interferometric metrology of the test masses to the level required for LISA, around $10\,\text{pm}/\sqrt{\text{Hz}}$ at a few mHz;

- characterise all noise sources to the levels required for LISA to gain confidence in the overall system performance;
- demonstrate the space flight worthiness of many of the applicable technologies such as test mass caging mechanisms, micronewton thrusters, optical assemblies etc.

The core experiment of LISA Pathfinder is the LISA Technology Package (LTP), which will feature two LISA type test masses, positioned either side of an optical bench that will measure their relative displacement interferometrically. In this way, it is analogous to a single LISA arm, with the baseline reduced from 5×10^6 km to 376 mm [24]. A CAD rendering of the LTP core assembly is shown in Figure 2.1.

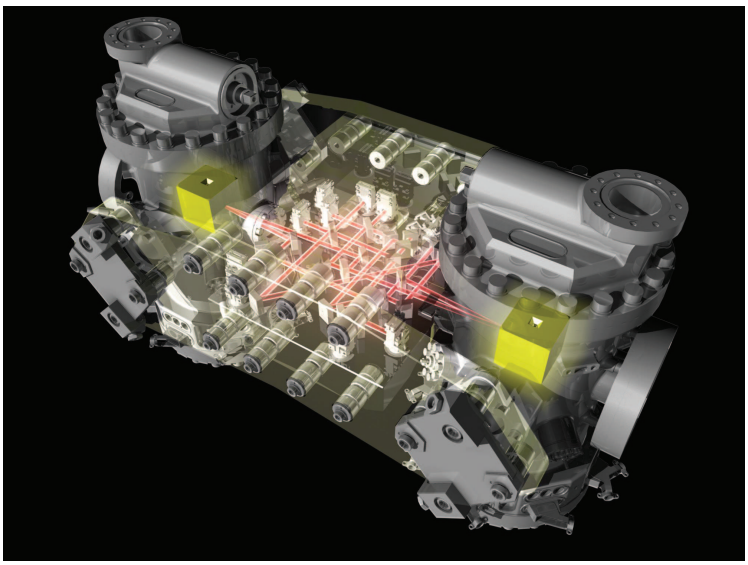

Figure 2.1: *CAD rendering of the LTP core assembly. The two cubical test masses are housed inside the inertial reference sensors at either end with the optical bench in between, connected by side walls (graphic courtesy of ESA).*

A schematic showing the principle of operation for LISA Pathfinder is shown in Figure 2.2. Like LISA, LISA Pathfinder will use Mach-Zehnder heterodyne

interferometry to read-out the test mass positions. For simplicity, it is a non-polarising scheme the result of which is that the beams probing the test masses must do so at a slight angle to allow separation of the incident and reflected beams. Light from the master laser, an Nd:YAG non planar ring oscillator operating at 1064 nm, is split and each beam is passed through an acousto-optic modulator (AOM) which frequency shifts the light by the drive frequency $\nu \simeq 80$ MHz. The difference between these two drive frequencies, $\nu_1 - \nu_2$, provides the heterodyne frequency. In LISA Pathfinder, this will be 1.6 kHz. Each beam is then coupled into a single-mode polarisation maintaining fibre and delivered to the optical bench.

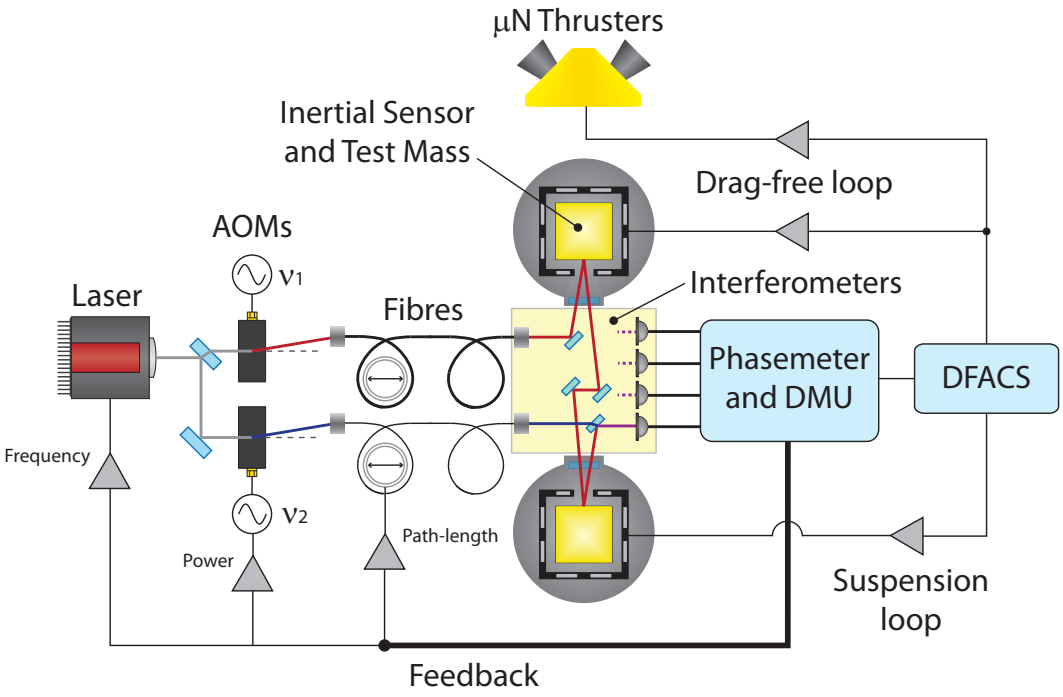

Figure 2.2: *Simplified schematic of the LISA Technology Package experiment on LISA Pathfinder. Only one interferometer path is shown on the optical bench for clarity.*

From the optical bench, the positions of the test masses are measured interferometrically. The optical bench houses four individual interferometers:

- the x_1 interferometer is a mix of a beam reflected from one test mass and a beam confined to the optical bench (the local oscillator), which measures the displacement between test mass 1 and the optical bench;
- the x_{12} interferometer is a mix of a beam reflected from both test masses and the local beam, which measures the relative separation of the two test masses;
- the *reference* interferometer is a mix of both beams, confined to the optical bench, and provides the phase reference for the measurements;
- the *frequency noise* interferometer, which has intentionally mismatched arm lengths to measure the frequency noise of the laser (see Section 2.2.2).

The interferometers are depicted in Figure 2.5 for clarity.

By comparing the reference phase to the phase of the two measurement interferometers, the relative displacements of the test masses can be measured. Any noise in the phase of the measurement signal which is not common mode with the reference phase will then determine the smallest displacement that can be measured, which for LISA Pathfinder must be in the 10 picometre region.

The interferometer outputs are connected to the phasemeter and data management unit (DMU). From the phasemeter/DMU, three stabilisation servos control the optical system: frequency noise is controlled at the laser, intensity noise is controlled through the drive signals to the AOMs and path-length noise is controlled at the fibres. This path length noise source was an unexpected one, discovered during early investigations into optical metrology for LISA Pathfinder at the University of Glasgow. Path-length noise had been expected to be induced inside the optical fibres and AOM's (which are not part of the stable optical bench), but it was predicted to be common mode between

the measurement interferometers and the reference, and so cancel out. In reality, there was some noise remaining after this cancellation, originating from parasitic beat notes caused by fluctuating cross-talk between the two AOM *rf* drive signals. The solution was to lock the reference phase signal to the electronic driver signal, by controlling the relative path lengths through the fibres [27, 28]. On board LISA Pathfinder, this control will be by means of a piezo which can apply stress to the fibre influencing the optical path length.

The output signals from the Phasemeter/DMU are also passed to the DFACS (Drag Free and Attitude Control System). DFACS is the control system responsible for placing - and maintaining - the test masses in geodesic motion. Each test mass is housed inside an inertial sensor housing, within which there are a series of electrodes which surround the test mass on all sides. These electrodes can be used either as capacitive sensors, to sense the position and attitude of the test mass (albeit with much reduced sensitivity compared to the optical measurement); or as electrostatic actuators with which the position of the test mass can be influenced in all six degrees of freedom. The inertial sensor housing and control systems developed for LISA Pathfinder are designed to be directly applicable to LISA, where control of the two test masses simultaneously is potentially slightly easier. This is because in LISA, the sensitive directions of the two test masses are 60° apart due to the equilateral formation (*i.e.* so that the sensitive direction of each test mass points towards the far spacecraft), where as in LISA Pathfinder the two test masses are collinear. This forces DFACS to actuate the test masses in the sensitive direction, potentially adding noise into the displacement measurement.

The DFACS operation principle is described in detail in [29, 30]. To survive launch, the test masses are locked in place with hydraulic launch-locks called the caging mechanism. Upon release of this system the exact position and

orientation of the test masses inside the inertial sensor housing is unknown, so DFACS must 'acquire' the test masses. In this initial mode, the electrostatic actuators are used to scan the test masses in a spiral pattern. The photodiodes of the interferometer are quadrant diodes, and so are position sensitive. As the test masses are scanned, the lateral position of the measurement beam on a photodiode is monitored and used as an error signal for the control to achieve a course alignment of the test masses. The system then switches to using the differential wavefront sensing (DWS) signal. DWS is a measure of the tilt of two interfering wavefronts, by taking the difference between the heterodyne phases on the different quadrants on a photodiode [31, 32]. It is an extremely sensitive discriminator for interference alignment, with resolution down to sub-μrad movements of one beam with respect to another. It is therefore an extremely effective means to control the attitudes of the test masses. DFACS will use the DWS read-out as an error signal to align and control the attitude of the test masses to as close to nominal as possible using the electrostatic actuators.

With the test masses aligned close to nominal, the so-called 'drift mode' can be implemented, where DFACS will keep the test masses as close to free-fall as possible. DFACS will monitor the position of one test mass using the capacitive sensors and the interferometric read-out and force the spacecraft to follow this test mass using the micronewton thrusters, this test mass is then considered to be drag-free. The displacement of this test mass to the spacecraft will be relatively noisy, dominated by the thruster noise. The second test mass is then controlled by the 'suspension' loop. DFACS will force it to follow the first test mass by applying a series of kicks using the electrostatic actuators. In this way, the test mass will drift between the kicks in free-fall motion. The displacement between the two test masses can then be measured, with the noise in the spacecraft motion cancelling out. The kicks are applied at a frequency

below the measurement band.

2.2.2 LISA Pathfinder interferometry

Since the main science read-out for LISA Pathfinder is an interferometric one, the design and construction of the interferometer is crucial to the success of the mission. Much work towards this end has already been completed, initially with a prototype interferometer built at the University of Glasgow [27, 28] and later with the engineering model (EM) of the LISA Pathfinder optical bench (also known as the optical bench interferometer, or OBI) constructed by the University of Glasgow and the Rutherford Appleton Laboratory [27, 33]. Figure 2.3 depicts both of these interferometers.

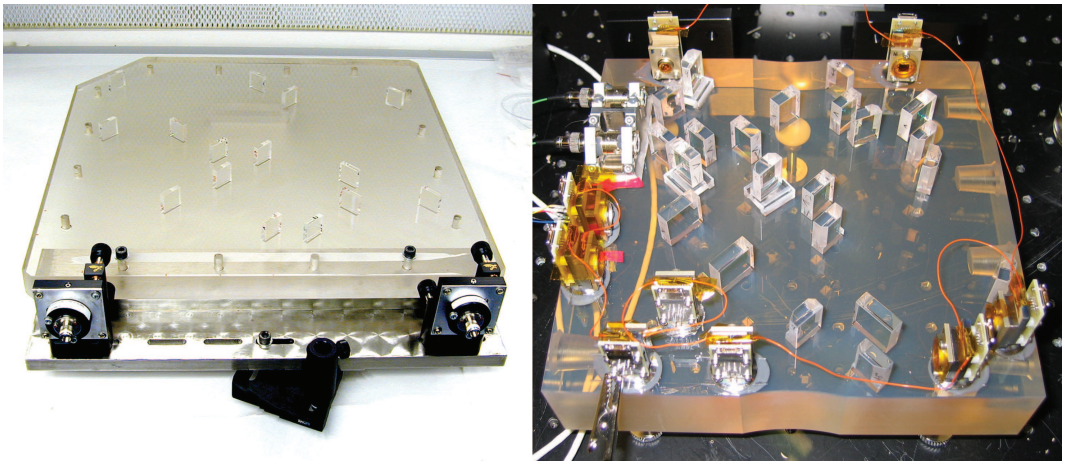

Figure 2.3: *Photographs of the Glasgow prototype optical bench which is of order* 400 mm × 400 *mm square (left) and the LISA Pathfinder OBI engineering model which is identical in size to the flight model at* 200 mm × 212 mm *(right, courtesy of Rutherford Appleton Laboratory).*

Since the OBI provides the fixed paths with respect to which the measurements are made, its intrinsic stability is of vital importance. For this reason ultra-low expansion ceramic substrates are required for such optical benches.

For the OBI, Zerodur® was chosen as the substrate since it has a coefficient of thermal expansion as low as 2×10^{-8}/K [34]. Coupled with the thermal stability of the spacecraft environment ($< 10^{-4}\,\mathrm{K}/\sqrt{\mathrm{Hz}}$ at 1 mHz [35]), this ensures good dimensional stability of the OBI. Due to its extremely good optical properties at 1064 nm, the optical components are made from fused silica with dielectric coatings for mirrors and beamsplitters. These are attached to the Zerodur® substrate using the hydroxide catalysis bonding technique [36, 37]. This method results in a bond which is strong enough to survive launch and provides high dimensional stability.

The optical layout for the flight model (FM) OBI for LISA Pathfinder is illustrated in Figure 2.4. It was initially developed by Gerhard Heinzel for the EM and later advanced by Felipe Guzmán Cervantes [38]. Further minor modifications were later made by Johanna Bogenstahl and the author. The Zerodur® baseplate has a surface area which measures 200 mm × 212 mm and there are 22 mirrors and beamsplitters forming the four Mach Zender heterodyne interferometers.

The interferometers are depicted individually for clarity in Figure 2.5. A CAD rendering of the OBI can be seen in Figure 2.6. The holes which can be seen in the side of the Zerodur® baseplate are for metal inserts, which allow the OBI to be integrated into the spacecraft structure.

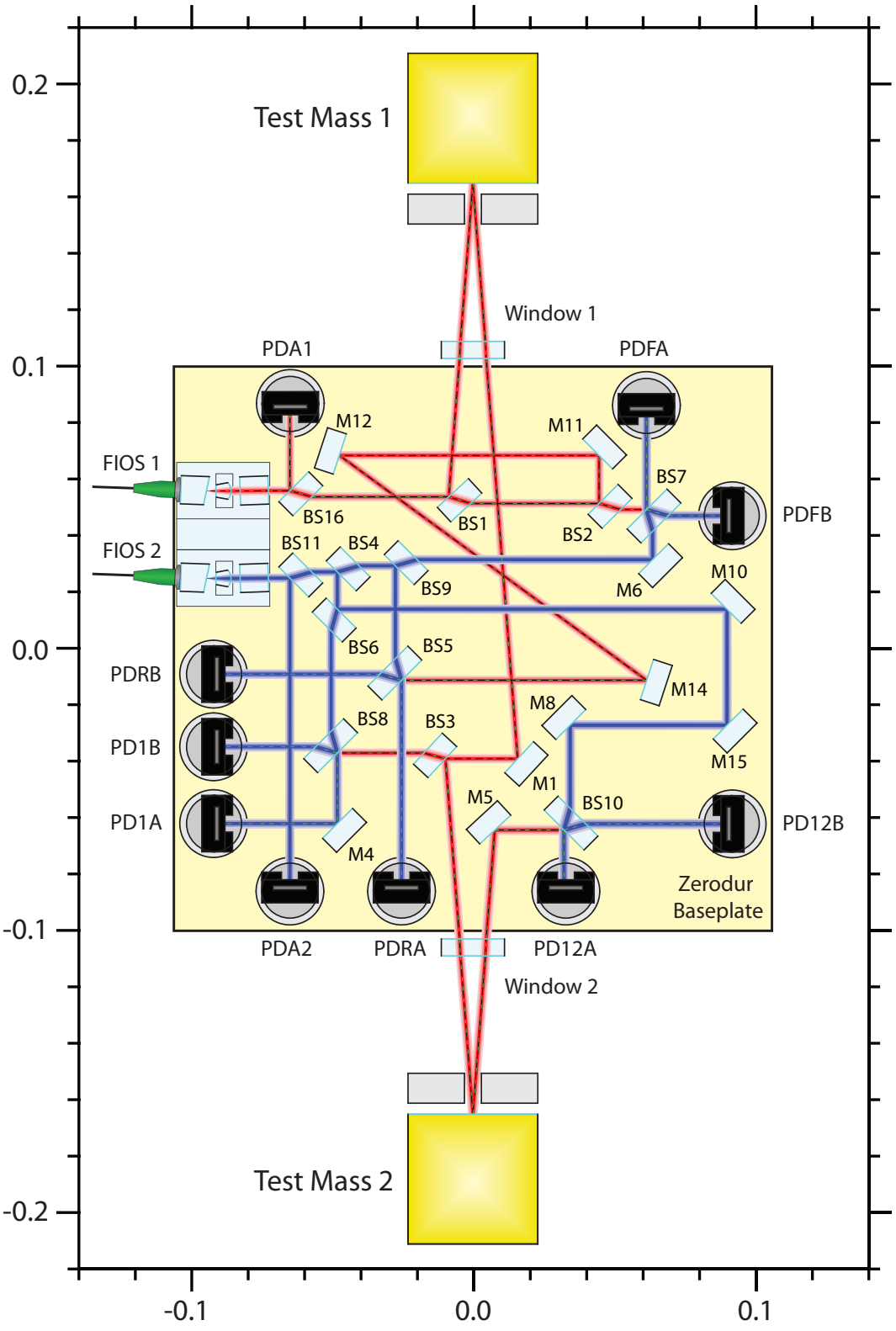

Figure 2.4: *OptoCad [39] model of the LISA technology package optical bench interferometer. Dimensions are in metres.*

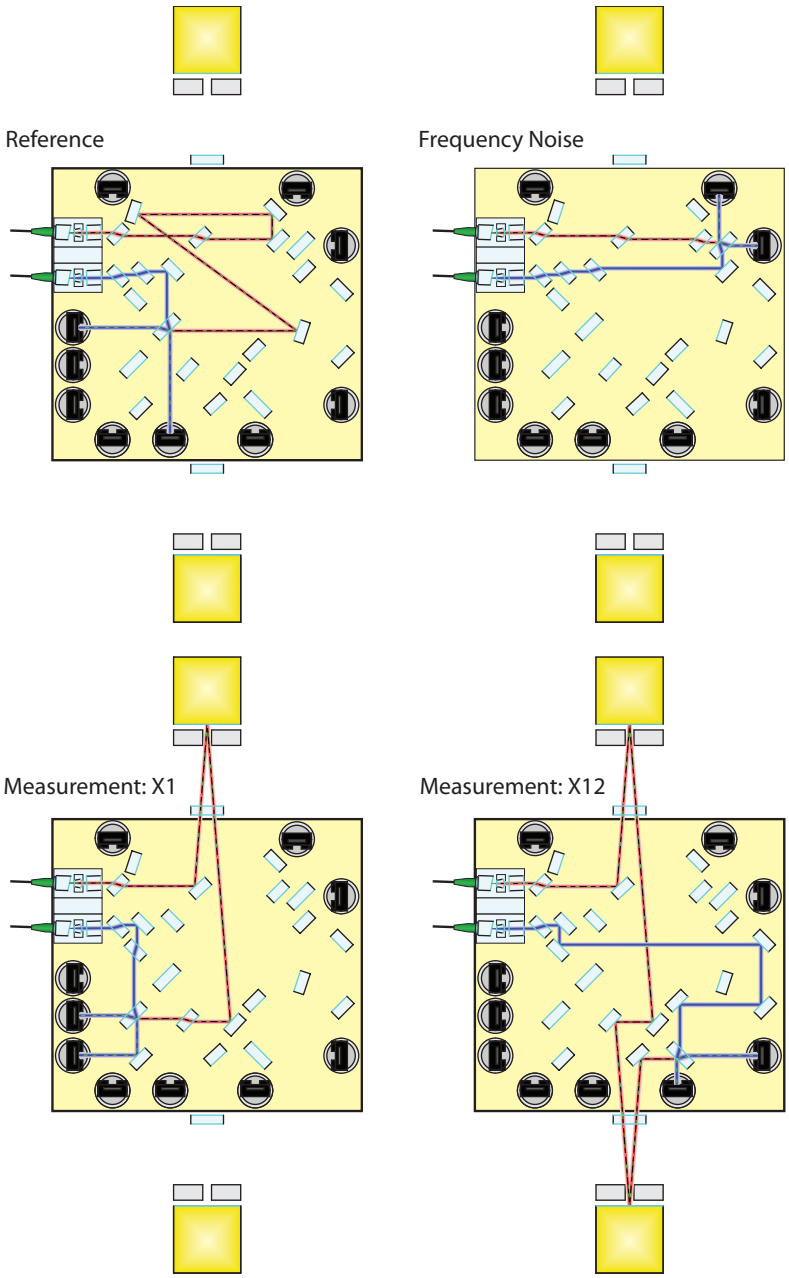

Figure 2.5: *OptoCad [39] models of each of the four interferometers on the OBI; reference (top left), frequency noise (top right), measurement of test mass 1 (bottom left) and measurement of both test masses (bottom right). The two feed fibres to the FIOS are of different lengths, which results in the end-to-end path lengths in the reference and measurement interferometers being approximately equal.*

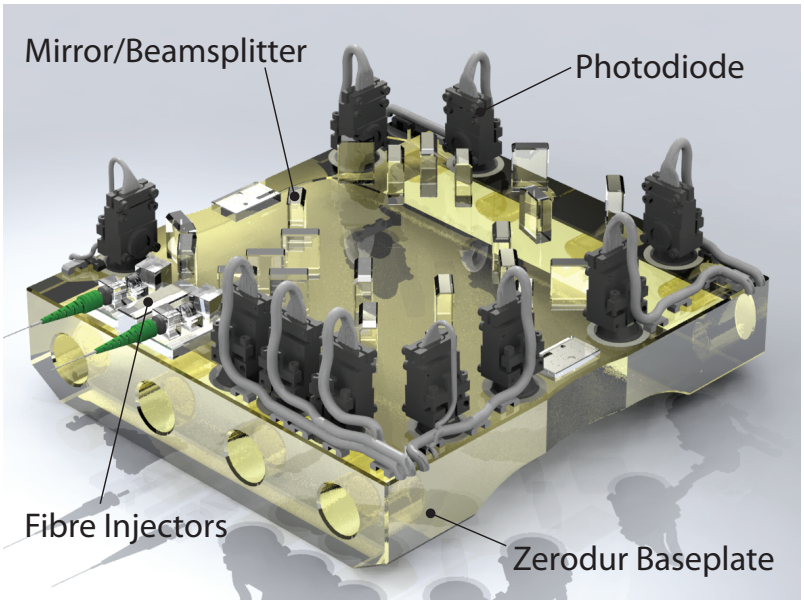

Figure 2.6: *CAD rendering of the FM OBI.*

To reach the design sensitivity of $10\,\mathrm{pm}/\sqrt{\mathrm{Hz}}$, there are several sources of noise which must be overcome, either by design or in the construction of the OBI; these are discussed below.

Intensity noise

Intensity noise (*i.e.* fluctuation in the power of the beam) can couple as noise into the interferometric measurement in two ways. Firstly, any intensity noise which is at the heterodyne frequency will couple into the measured heterodyne signal, producing random phase fluctuations. If we consider a relative fluctuation in the intensity of the laser $\frac{\delta P}{P}$, then we wish to limit the influence this has on phase to less than $2\pi \times 10^{-6}/\sqrt{\mathrm{Hz}}$ radians (or $1\,\mathrm{pm}/\sqrt{\mathrm{Hz}}$), *i.e.* [40]

$$\frac{\delta P}{P} \lesssim 2\pi \times 10^{-6}/\sqrt{\mathrm{Hz}}.$$

Secondly, since the beam which is incident on the test masses will impart a force due to radiation pressure, any variation in the intensity of the beam in the measurement band will then couple as detectable force noise into the test masses. For a test mass of mass m and light of frequency $\omega = 2\pi f$, the displacement δx induced by intensity noise of magnitude δP can be expressed as:

$$\delta x = \frac{2\,\delta P}{m\,c\,\omega^2}.$$

Again, we wish δx to be less than $1\,\mathrm{pm}/\sqrt{\mathrm{Hz}}$. Expressed in terms of a relative fluctuation in laser intensity this gives:

$$\frac{\delta P}{P} \leqslant \frac{m\,c\,\omega^2\,\delta x}{2P} \approx 3 \times 10^{-5}/\sqrt{\mathrm{Hz}}$$

To mitigate against these effects there will be two additional photodiodes on the OBI (PDA1 and PDA2 in Figure 2.4). These sample a pick off from each beam directly out of the fibre injectors, and are part of a feedback loop which servo controls the beam intensity by changing the *rf* drive power to the AOMs. By measuring each beam on the OBI itself and controlling at the AOMs, each beam is controlled individually such that any effects induced in the fibres or the AOMs themselves are attenuated. Neither of the two intensity stability requirements are considered to be challenging [40].

Frequency noise

Noise in the frequency of the laser can couple as noise in the displacement measured by an interferometer, if the interferometer has unequal arm lengths. For a laser with frequency noise $\delta\nu$ the apparent length change δx which will

be observed can be expressed as

$$\delta x = \Delta x \frac{\delta \nu}{\nu} \tag{2.1}$$

where ν is the frequency of the laser and Δx is the path length difference between the arms of the interferometer. For a simple interferometer (like a Michelson), rejection of frequency noise would require an identical round trip path length for both arms. On LISA Pathfinder however, we are making a comparison between the phase of two interferometers: a reference and a measurement. In this case it is then the relative path length difference between the reference and measurement interferometers which is important, *i.e.* that the frequency noise signal at the reference interferometer is the same as that of a measurement interferometer such that it can be subtracted out as a common mode signal. The nominal OBI layout has perfectly matched paths, but constructing an interferometer without path mis-match is difficult. For a relative path length mismatch of 1 mm (which is the upper limit for the FM OBI [35]), keeping the induced displacement noise δx to below $1\,\mathrm{pm}/\sqrt{\mathrm{Hz}}$ requires that the laser frequency noise is less than $300\,\mathrm{kHz}/\sqrt{\mathrm{Hz}}$. This level is several orders of magnitude below the noise level of the free-running LISA Pathfinder laser in the measurement band, and so some means of countering the frequency noise is required.

A standard technique is to lock the laser to a suitable reference, such as using Pound Drever Hall locking with a stable reference cavity [41]. LISA Pathfinder will use a slightly different technique to avoid the need to carry additional payload mass. The OBI has a dedicated interferometer with an intentionally large Δx to maximise the coupling of laser frequency noise in its read-out signal. Using this read-out the laser frequency noise can be directly controlled by stabilising the phase of the frequency noise interferometer to the reference interferometer in a servo which feeds back to actuate the laser frequency. The data from the frequency noise interferometer can also be used to correct for

laser frequency noise in post-processing of the data.

As an additional step, significant effort will be made in the construction of the OBI to ensure that the path length difference of the measurement interferometers is the same as that in the reference interferometer. The OBI has several components which can be used to correct for built up path length error; this is discussed in more detail in Chapter 5.

Test mass jitter

At some level, keeping the test masses in perfect geodesic motion is impossible: there will always be residual motion of the test masses. One component of this motion will be angular, expected to be of order $10^{-7}\,\mathrm{rad}/\sqrt{\mathrm{Hz}}$. At the reflecting surface of the test mass, this angular jitter could be converted into a longitudinal signal, contributing directly to the measurement noise, increasing with distance from the centre of the reflecting face. To keep the induced longitudinal noise to an acceptable level, the beam must be centred on the test mass to less than $50\,\mu$m. Half of this error is assigned to the construction of the OBI, requiring that the beam from the OBI towards each test mass be within $\pm 25\,\mu$m of the nominal reflection point [35].

Beam jitter

Jitter of the beam launched from the fibre injectors can result in a variety of noise contributions, including path length changes between reflective components and loss of phase information at quadrant photodiodes. For more severe beam jitter, loss of interferometric contrast is also a potential problem. To mitigate against these effects, fibre injectors with minimal beam jitter and long

term stability are required, they must also be sufficiently rugged to survive launch forces. Additionally, to prevent any loss of information at the photodiodes, the diameter of the diode element will be in the region of 3 to 4 times larger than the beam diameter.

Path length fluctuations

Fluctuations in the optical path length of the interferometers would clearly couple as measurement noise directly. There are two ways in which path length fluctuations can occur, the first is in the distance between reflective components changing (*i.e.* the baseplate dimensions fluctuating), and the second is the optical path of transmissive components fluctuating. The primary driver for both of these potential noise sources is temperature.

LISA Pathfinder will have a temperature stability better than $10^{-4}\,\mathrm{K}/\sqrt{\mathrm{Hz}}$, and this coupled with the extremely low coefficient of expansion of Zerodur® negates any effects induced from expansion of the baseplate.

Changes in the optical path of transmissive components can be induced from simple thermal expansion of the substrate material, and by thermally driven changes in the refractive index. The components are made of fused silica, which has a thermal expansion coefficient of $\sim 0.5 \times 10^{-6}\,/\mathrm{K}$ and a $\frac{dn}{dT}$ of $\sim 9.7 \times 10^{-6}\,/\mathrm{K}$ [34]. Although these values are low, especially the coefficient of thermal expansion, several successive transmissions through LISA Pathfinder sized components can produce effects at the 10's of pm level, far above the design sensitivity. In reality the temperature variations across the OBI will be extremely uniform. By ensuring that each beam path experiences a roughly balanced transmissive path in silica then much of the thermally induced path length variation will be common mode between the measurement and reference

interferometers and so cancel out. The OBI has been specifically designed with this approach in mind, and it has been experimentally verified in both the Glasgow prototype bench and the engineering model for the LISA Pathfinder OBI [27, 28, 33, 42].

Chapter 3

Measuring a beam in free space

3.1 The need for precision

Many of the requirements discussed in Chapter 2 necessitate extremely precise measurements of the physical position of a laser beam, and the ability to construct an equation to describe that beam and relate its position to some external geometry. A good example of this is the requirement that the beam incident on the test mass (for both LISA and LISA Pathfinder) must be centred to within approximately $\pm 25\,\mu$m of the centre of the test mass [35].

We can then define the following top-level requirements:

- the measurement system must have an absolute accuracy down to a few μm, and a few 10's of μrad and be repeatable to better than that;
- it needs to relate the optical measurement of the beam to some physical coordinate system;
- the practicality of alignment with the hydroxide catalysis bonding tech-

nique dictates that beam position read-out must be near instantaneous to be of any use; this requires that the system is capable of a 'live' read-out.

Determining the centre of a $\sim 1\,\mathrm{mm}$ or larger diameter beam to a few μm even at a single plane is not a trivial task. A real beam will not be gaussian or perfectly circular and is highly likely to have fine fringe structure resulting in multiple local intensity peaks at the centre. A typical beam as used for LISA Pathfinder is shown in Figure 3.1.

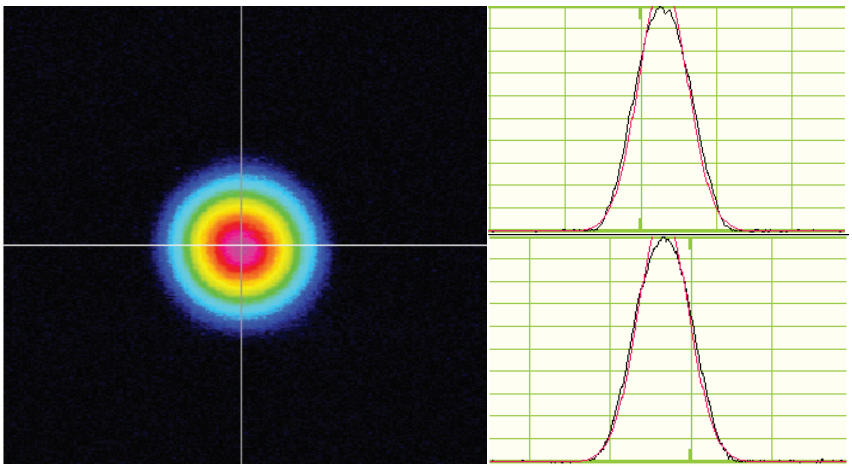

Figure 3.1: *Intensity profile of a typical beam from a fibre injector as used in LISA Pathfinder. 2D profiles of the x and y axis are shown on the right.*

Two possible approaches for defining the centre of a beam are the *power centre* and the *optical centre*. The power centre is defined based on measurements of the intensity of a beam, for example by balancing the powers in the four quadrants of a quadrant photodiode. The optical centre is defined by measurements based on optical properties, such as the centre of a diffraction pattern. In a theoretical beam these are perfectly coincident but the same cannot be expected in a real beam: they may be very well aligned but will almost certainly be different at the $\sim 10\,\mu$m level. Which of these definitions is most appropriate is not an easy question to answer and will depend on the intended

application. What is clear is that, internal to a system, the same definition should be maintained throughout to avoid systematic effects from a potentially shifting beam centre.

For construction of the LISA Pathfinder OBI, the power centre was chosen as the reference. It benefits from being significantly easier to measure and analyse than the optical centre, and by using a Quadrant Photodiode (QPD) to make the measurement, local imperfections in the beam are averaged out. It does require an underlying assumption that a beam will be rotationally symmetric, since the method of determining a beam centre with a QPD is to balance the powers in all four quadrants. If a beam is not rotationally symmetric, then the position determined from balancing the powers will not necessarily be the true centroid of the beam. In practice, beams such as the one shown in Figure 3.1 are sufficiently circularly symmetric that this effect is negligible, contributing less than 1 μm of uncertainty.

If two measurements of the centre of the beam are made using a QPD, spatially separated by a sufficient amount, this will give a line which will have an equation representing the beam. Inherent in this approach is the ability to relate the two measurements together in some reference frame, and to then relate this measurement to some other arbitrary reference frame (that of a test mass, for example). The tool best suited to this is a Coordinate Measuring Machine (CMM). The machine used for all measurements described throughout this thesis is a *DEA Global Image* [43]. It has a measurement volume of 1.0 m $\times$ 0.7 m $\times$ 0.5 m, and a certified absolute measurement accuracy of $\pm$ 1.5 μm at a single point plus 3 μm per metre length error. A photograph of the CMM, in situ in the ultra-clean laboratory can be seen in Figure 3.2.

Through its software interface (PC-DMIS [43]), features on an object can be measured and coordinate systems built around these measurements. Other

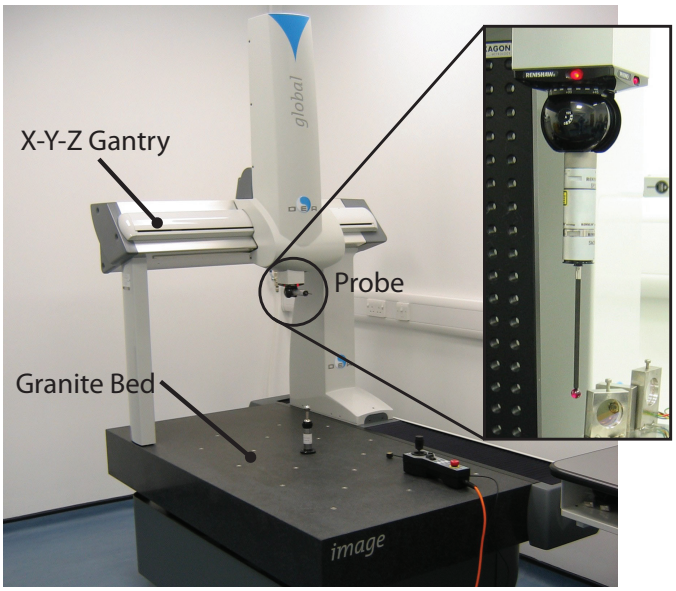

Figure 3.2: *Photograph of the Coordinate Measuring Machine (CMM).*

features can then be directly measured in this constructed frame. This allows easy and convenient measurement of the relative position of two objects.

3.2 The Calibrated Quadrant photodiode Pair

Measuring a QPD directly when positioned at the centre of a beam is clearly not feasible: a support structure is required to enable easy measuring with the CMM. The simplest device to imagine is a block with a hole in the middle, into which a single QPD is mounted. This block could be positioned such that the beam is centred on the QPD and the position of the block can then be measured with the CMM. Knowledge of the location of the photodiodes position within the block would then allow a single point on the beam to be measured in a particular coordinate frame. Two (or more) measurements along the beam axis would then yield enough points to construct a line which describes that beam.

This simple device has two main drawbacks: firstly, unless the actual plane of the diode is known to high accuracy small errors in the angular position of the block relative to the beam direction can give rise to uncertainties through projection effects; secondly it cannot ascertain the true position and direction of a beam instantaneously, a minimum of two measurements are required to get the beam direction. To be truly versatile, we need to make two measurements simultaneously, this is the idea behind the Calibrated Quadrant photodiode Pair (CQP).

3.2.1 CQP measurement concept

The basic idea of the CQP is to have a structure, incorporated into which is a beam splitter and two QPDs at different distances from each output port of the beam splitter. For this arrangement, there is only one vector for which a beam incident on the splitting surface will be centred on the QPDs at both output ports. This concept is illustrated in Figure 3.3.

If the equation describing this vector is known relative to the structure, then aligning the structure to the beam (by centring on the QPDs) and measuring with the CMM allows instant determination of the equation of the beam being measured. Moreover, if the position of the structure can be controlled to a fine degree, it can be pre-positioned to lie on a theoretical beam. In this way it can act as a live target. Any beam that is actuated such that it is centred on both QPD's while the structure is in this position, must have the same equation as the theoretical beam to which the structure is aligned.

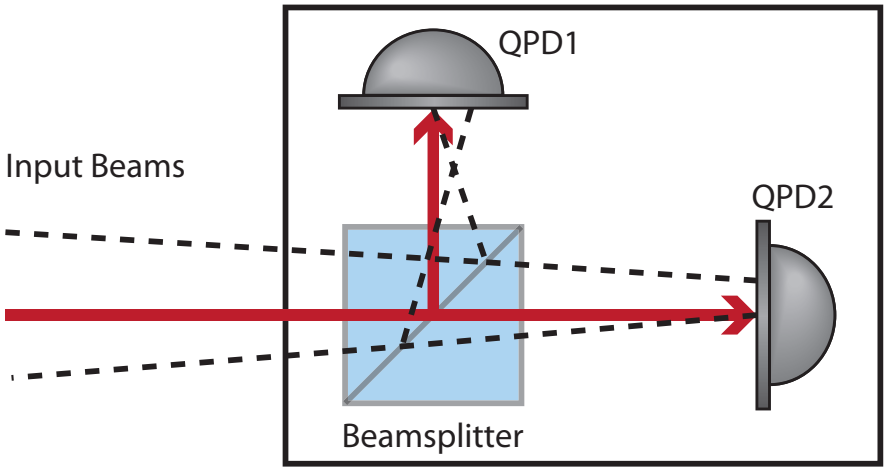

Figure 3.3: *Basic concept behind the CQP. The red beam is the only possible input beam to the beamsplitter which will be centred on both QPDs. Other beams that can be centred on one QPD are possible, but will always be off-centre of the other (shown as black dashed lines).*

3.2.2 Design choices

To turn this simple concept into a usable tool requires that a number of additional things be considered. The primary design drivers are accuracy and stability. Ideally, an accuracy of $< 5\,\mu$m and of order $20\,\mu$rad or better is required. The CMM measurement error of $1.5\,\mu\text{m} + 3\,\mu\text{m/m}$ results in an improving angular measurement with increasing baseline, at the expense of absolute positional knowledge. This is illustrated in Figure 3.4. Also of consideration is that to be of any use, it must be small enough to fit inside the CMM measurement envelope alongside the OBI or any other potential beam source, and be mountable on a movable stage so that it can be positioned accurately. The stages used here are 6-axis high precision Hexapods, model M-824 from Physik Instrumente [44] (see Figure 3.5), and can be actuated at the sub μm and $3\,\mu$rad level. They are in the region of 250 mm in diameter.

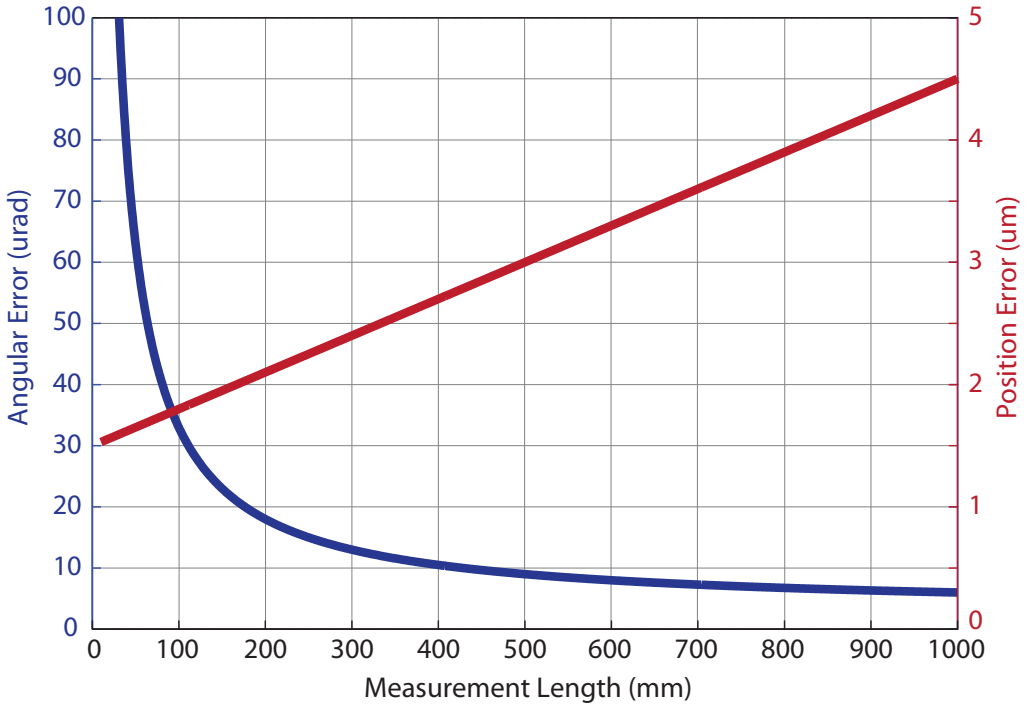

Figure 3.4: *Graph showing the accuracy of the CMM, both absolute position (in green) and angle (in blue) with increasing measurement baseline.*

Given these factors, baselines of $200 - 300\,\text{mm}$ are well suited for this purpose, giving a good compromise between overall size, and accuracy of CMM measurement.

As a result of the extremely tight accuracy requirement, the stability of the CQP is extremely important and it must be very resistant to both thermal expansion and mechanical vibration. The thermal expansion of aluminium over 200 mm is of the order $4\,\mu\text{m}$ per °C for example, which could add significantly to the positional and angular error of the CQP. Invar® was therefore chosen as a suitable material, which over the same range will have sub μm thermal expansion. Invar® is also strong and easily machinable allowing for rigid construction to help with mechanical stability.

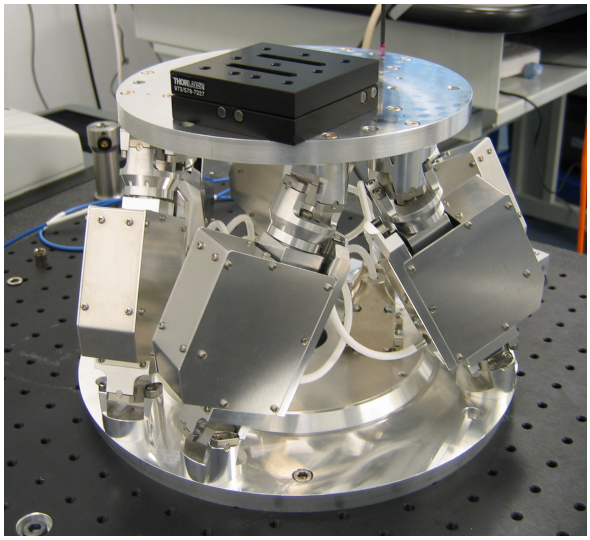

Figure 3.5: *Picture of a Physik Instrumente M-824 Hexapod.*

A further factor to consider is the *effective* distance between the photodiodes. In the simple schematic shown in Figure 3.3, this would be the optical path from the beamsplitter to QPD2, minus the distance to QPD1. This is the optical baseline, and it determines how accurately the CQP can be aligned to the beam. Since aligning a beam perfectly to the centre of a QPD is not realistically possible (factors like air currents will always cause beam jitter at some level, and actuators have resolution limits) some margin must be defined under which the beam can be considered centred. If this margin is taken to be $\pm 1\,\mu$m (a feasible number), then this defines an angular error of the beam centring over the optical baseline.[1] It is desirable to keep this as small as possible. Simply taking the optical baseline to be the same as the length scale of the CQP gives an additional angular error of $\sim 10\,\mu$rad. If the path is folded however, the baseline can be increased to over double this, bringing the error down to a level where it can be regarded as negligible (in comparison to other

[1] Clearly, there are other factors that can enter into this, such as a non perfect beam evolving over distance such that its intensity centre drifts a few μm. These effects are difficult to assign an error to, however, as they are unique to each situation.

errors present in the measurements).

3.2.3 CQP Construction

The CQP, as built, is shown in Figure 3.6. The optical baseline is of the order 44 cm which gives good angular resolution of the incoming beam. Due to the extreme sensitivity to mechanical deformation (which would change the calibration parameters), a single point mount is used; whereby a single bolt affixes the CQP to a Hexapod through a large washer. This minimises the chance of the mount deforming the CQP structure. To further increase the mechanical rigidity and durability of the CQP, the various components are secured with epoxy in addition to mechanical fasteners.

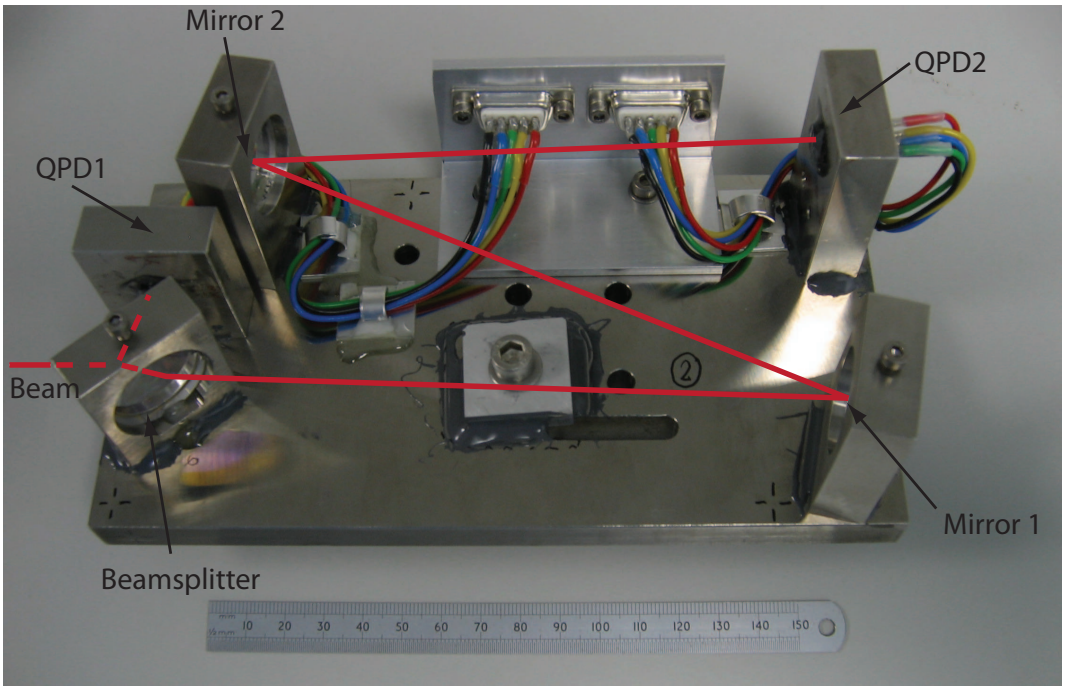

Figure 3.6: *Photograph of the CQP, with the beam path indicated in red.*

The mounts for the mirrors and the beamsplitter are designed to be isostatic 3-point mounts (similar to a commercial mirror mounts), and have 'blobs' of

glue added to give extra rigidity to the mount. The QPDs are also glued in place, located in counterbored holes, and are glued from the front and the back to minimise the possibility of movement.

The QPDs are Si quadrant diodes manufactured by Centronic (model QD7-5T) and have an active area of $7\,\mathrm{mm}^2$ and a dark current of $\sim 6\,\mathrm{nA}$. They are reverse biased with $-15\,\mathrm{V}$ and read-out through an 8 channel transimpedance amplifier into a simultaneously sampled 8 channel National Instruments 16 bit analogue to digital convertor at a sample frequency of $92\,\mathrm{kHz}$. A LabVIEW front end calculates the position of the beams on each photodiode, in microns, using equations

$$x = -\beta\left[(A + C) - (B + D)\right] \tag{3.1}$$

$$y = \beta\left[(A + B) - (C + D)\right] \tag{3.2}$$

where x and y are the cartesian coordinates of the beam centre on the QPD, A, B, C and D are the powers from each quadrant, as per the labelling convention shown in Figure 3.7, and β is a calibration factor, determined by translating the CQP a small amount and using the CMM to measure the relative displacement. This can then be used to derive the value of β to give an output in μm.

In practice, the CQP is used with amplitude modulated (AM) light (typically modulated at $230\,\mathrm{Hz}$) and a *single bin discrete Fourier transform* method is used to extract the signal amplitude at the modulation frequency. Using the CQP in this AM mode has the advantage of isolating the measurements from effects such as variable offsets caused by changing background lighting or DC drifts in electronics.

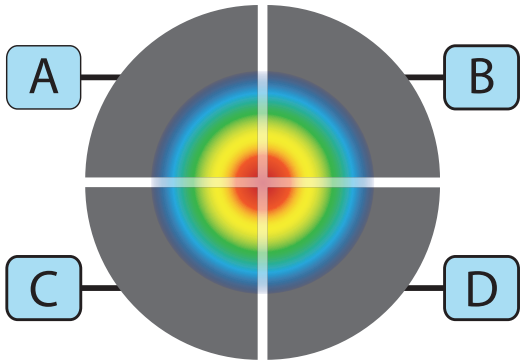

Figure 3.7: *Diagram showing the labelling convention for the quadrants on a QPD, looking at the active face.*

3.3 Calibration of the CQP

In order to be of any use, the CQP must be calibrated to establish the relationship between the physical structure (the Invar®) and the beam vector which is centred on both photodiodes. When the CQP is measured with the CMM, a fully defined reference frame is established which represents the position of the CQP in the measurement envelope. The frame is constructed by measuring a fixed set of points on the surfaces of the CQP baseplate with the CMM probe. Ensuring that the same points are measured each time is important, as this is the key to ensuring the repeatability of establishing the reference frame and thus the consistency of the beam measurements. The frame is centred at the front corner of the baseplate (next to the incoming beam), and has axes orthogonal to the Invar® baseplate. The calibration parameters describe the position and direction of the nominal beam within this reference frame.

3.3.1 2D calibration example

The procedure to obtain the calibration constants is best illustrated in 2D for clarity, and is shown in Figure 3.8. We wish to relate a beam centred on the CQP to the reference frame set up when measuring it. This can be described in terms of two offset parameters which we need to measure: distance d and angle θ, where d is the distance from the origin to the point where the beam crosses the y-axis of the frame, and θ is the angle between the x-axis of the frame and the beam. In the 2D case these two numbers fully define the beam vector in the CQP reference frame.

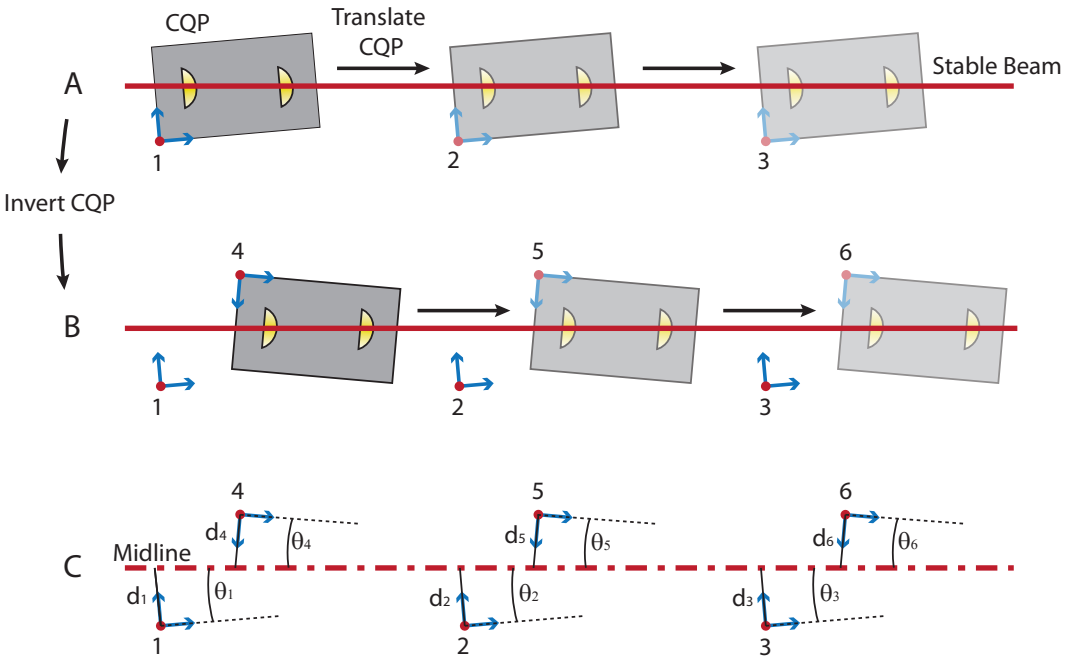

Figure 3.8: *Two dimensional example of the CQP calibration procedure.*

The solid red line represents a beam, which is known to be stable at the $\sim 1\,\mu$m and few μrad level over the duration of the calibration procedure. This is achieved by gluing a stable fibre injector (see Chapter 5) to a Zerodur® spacer which is mounted to the CMM bed with a kinematic mount. The position and orientation of the stable beam are arbitrary and unknown. In the first step,

'A', the CQP is aligned to this beam (position 1 in the diagram), measured and the resulting reference frame stored (shown as an origin with a red spot and axes as blue arrows). The CQP is then moved along the beam, realigned to it, and further measurements are taken (2 and 3 in the figure). This already gives enough information to obtain the direction of the calibration beam, and thus the θ calibration parameter but the offset distance is still unknown: more information is required.

In step 'B' the CQP is rotated 180° around the beam axis and re-aligned to the beam. A further set of measurements is then taken (positions 4, 5 and 6). This procedure gives us 6 separate reference frames all aligned to the same unknown optical beam. Due to the symmetry of the rotation we know that the calibration beam must follow the midline of the 6 origin points of the reference frames. This allows us to calculate the equation of the calibration beam, shown as a red dashed line in step 'C'. We can then take the equation of the calibration beam and for each of the measurements calculate the calibration factors d and θ. These results can then be averaged to give the best estimate. Note that provided the measurements are over constrained we can use the variation in the individual d and θ values (*i.e.* the residuals) to estimate the accuracy of the calibration.

3.3.2 3D calibration of the CQP

In practice, the CQP needs to work in a three dimensional envelope, and so the calibration procedure must be extended to three dimensions. Here, we require four parameters in order to fully define the beam with respect to the CQP reference frame; two distance parameters d_y and d_z and two angle parameters θ_x and θ_z. Having measured the CQP reference frame, these 4 numbers are

sufficient to construct the equation of the incident beam; this is illustrated in Figure 3.9.

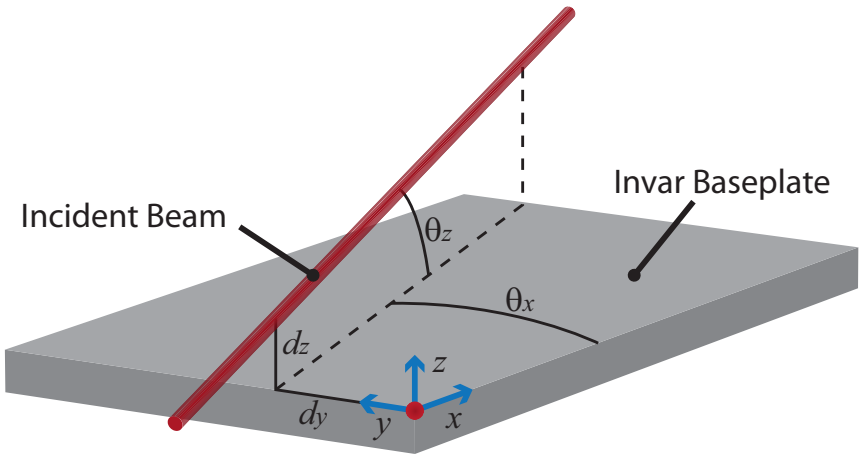

Figure 3.9: *Diagram showing the 3D coordinate system of the CQP, and the calibration factors required to define the beam relative to it.*

In extending to three dimensions, the basic procedure described in Section 3.3.1 remains. An incident stable reference beam is set up and multiple measurements are made along the length of the beam, recording the parameters that define the CQP reference frame for each measurement. In the 2D example, measurements of the CQP in two 'orientations' were required in order to fully define the system and obtain both d and θ. In three dimensions a similar approach was used only this time measurements in at least three orientations are required. The resulting CQP origin points will all lie on the surface of a cylinder with the axis of this cylinder having the same equation as the calibration beam. This is illustrated in Figure 3.10. The four parameters can then be determined relative to the axis of the fitted cylinder for each of the measured CQP reference frames and averaged as in the 2D example.

The minimum number of measurements required to construct the cylinder is

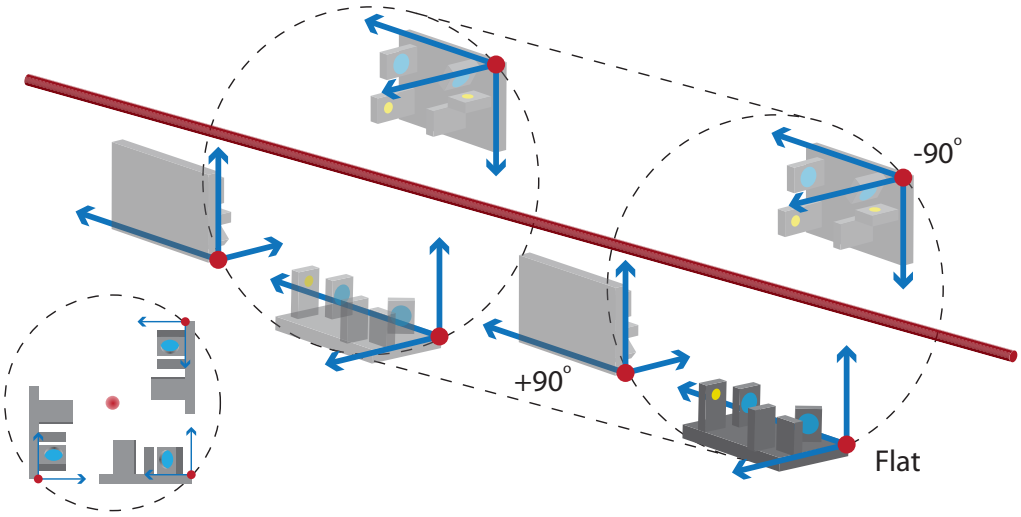

Figure 3.10: *Illustration showing the calibration of the CQP. The red centre line represents the calibration beam, with the dashed cylinder the fit to the measured CQP positions. A 2D cross section is inset. The CQP is not drawn to scale for clarity.*

5. In practice many more measurements are taken (typically 12 to 20), often in four or five orientations. This over defines the system and allows analysis of how good a particular calibration is through calculation of the residuals. The measurements in the initial orientation (typically flat) are repeated at the end of the calibration procedure to verify that the calibration beam has not moved during the procedure. A plot of typical residuals for a CQP calibration can be seen in Figure 3.11.

The figure shows that the CQP calibration is accurate to around $\pm 3\,\mu$m and $\pm 20\,\mu$rad. There are indications of small systematic errors between different orientations, this is most noticeable between $\pm 90°$ in 'Z'. Due to the complexity of the system and the measurement, the exact source of this error is unknown, but there are strong indications that is may be due to a calibration issue in the CMM. The probe head of the CMM (shown in Figure 3.2) is adjustable

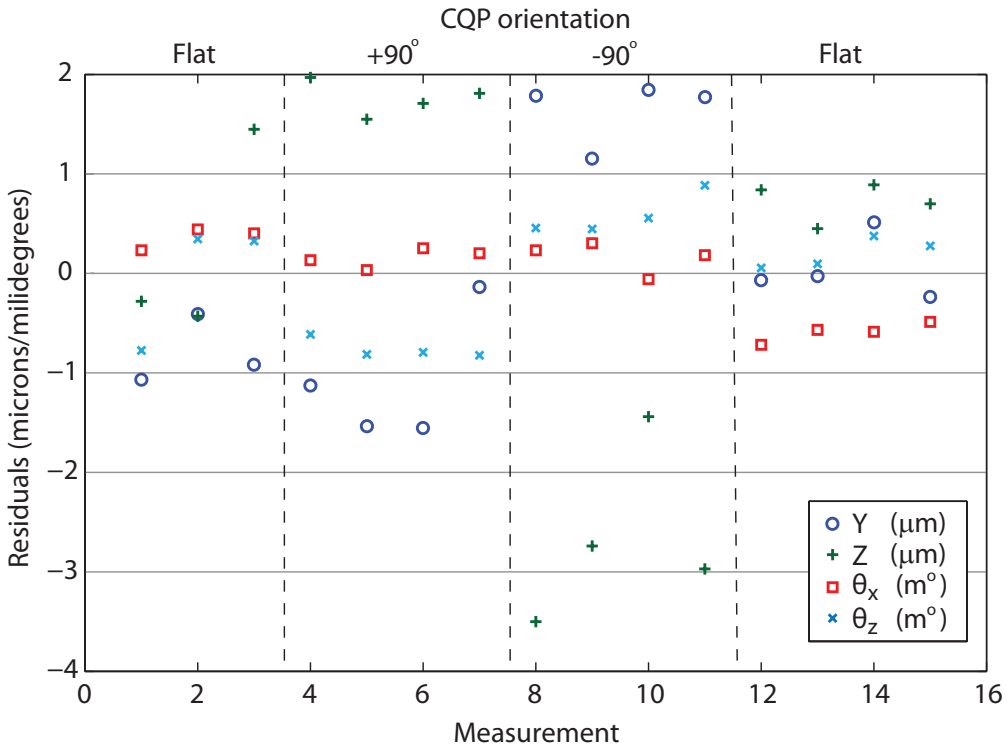

Figure 3.11: *Plot of the residuals from a typical CQP calibration, with a total of 15 measurements in three orthogonal orientations. One millidegree is equal to* 17.5 μrad.

in angle, and a different angle is required to measure the CQP in each orientation due to access restrictions. For each of these probe angles, there is an individual calibration of the CMM probe head. Systematic deviations between these CMM calibrations could couple into the CQP calibration, appearing as systematics between the measurement sets. This translation in angle is the leading candidate as the source of the systematics in the calibration, but the exact nature is unknown.

3.4 CQP accuracy

Given the critical nature of the alignment tasks for which the CQP is used (see Chapter 5), it is important that its accuracy and repeatability can be verified, preferably without resorting to a full recalibration which is time consuming due to the number of measurements required. There are two useful ways to verify that the CQP is performing as expected.

The simplest test that can be performed is to make two measurements of a single, stable, beam at two different positions along its length. For each measurement of the CQP, the CMM returns two points of the form $\mathrm{P}(x, y, z)$, separated by 300 mm along the beam calculated using the calibration parameters. These points are given in the measurement frame (the choice of which is essentially arbitrary). Joining the points will form the line of the as-measured beam. Taking two CQP measurements, with the CQP moved along the beam will provide four such points, with the measured beam being the best fit line of these points. Calculating the distance of these four measurement points from the best fit line gives a partial check on the accuracy of the CQP calibration parameters. For example if one of the CQP calibration parameters - say θ_z - were wrong, then this would result in each measurement having an angular offset from the real beam. The result would be two parallel lines, each systematically angled from the fit line. This is illustrated in Figure 3.12. The signature of this is typically that the values of D_2 and D_3 are large compared to D_1 and D_4. This is due to the baseline over which the measurements are made (typically $200 - 300$ mm), and the resulting spread of points as indicated in the diagram.

This quick method is useful, but gives limited information about what parameter might be wrong, and only gives a rough estimate of the value of the error.

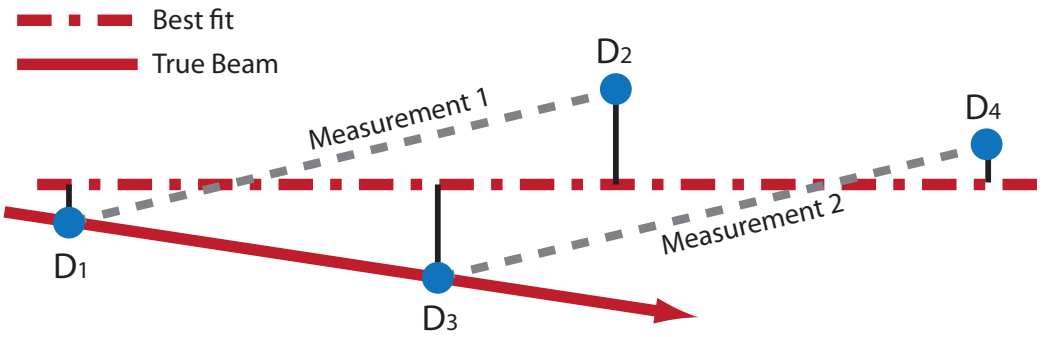

Figure 3.12: *Diagram illustrating how an incorrect calibration parameter can be detected using a double measurement of a beam*

Systematic effects of the CMM can also be masked. A more robust method, is to make two, or more, measurements of a single, stable beam in several orientations. This is illustrated in Figure 3.13. By rotating the CQP about the beam (much like in the calibration process) any error inherent to the CQP will rotate along with it. This method is akin to a part-calibration (and is therefore quicker), it provides a useful handle on separating effects due to the CQP, the CMM or even the measurement beam.

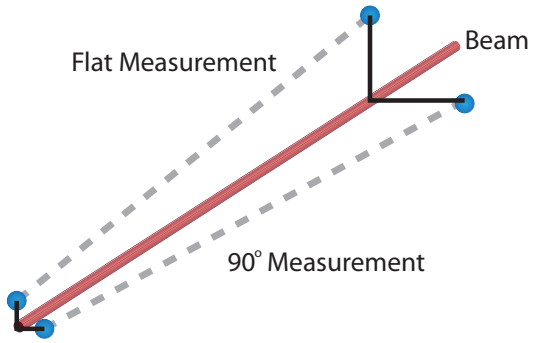

Figure 3.13: *Diagram illustrating checking the CQP accuracy by making measurements rotated about a beam.*

A plot showing the typical results from such a test of the CQP is shown in Figure 3.14. This test has four measurements of a stable reference beam, two with the CQP flat and two at $+90°$. The two measurements internal to each

orientation are spatially separated by $\sim 20\,\text{cm}$, such that the distribution of measurement points along the beam is similar to that depicted in Figure 3.12, which is about 500 mm between the front most and rear most point. The x axis of the figure (which points out of the page) is the fitted line of all 8 measurement points.

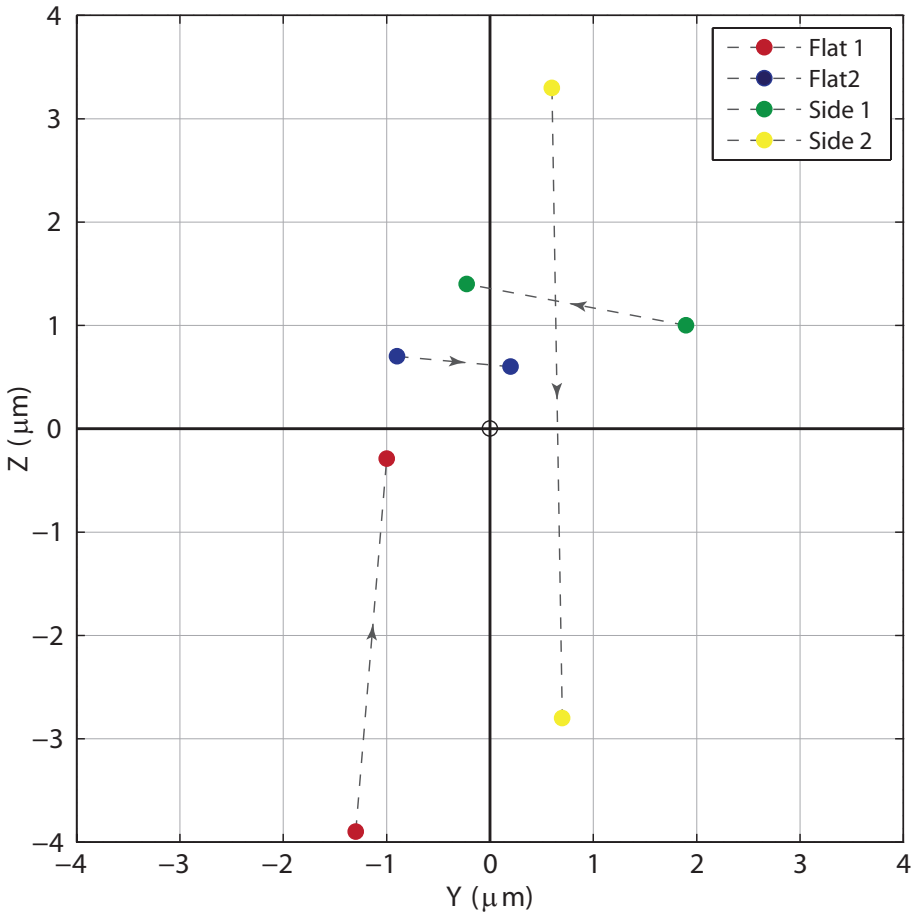

Figure 3.14: *Plot showing the results of a check of the CQP accuracy by making multiple measurements of a stable beam in two orientations.*

The arrows on the lines connecting the points for each measurement indicate the direction from the front point to the rear point, so if the plot were three dimensional, this would indicate the direction of slope. Any correlation between the direction of this slope, and the orientation of the CQP indicates a possible

error in the calibration parameters. From the plot, there is no obvious correlation of this type visible. Clearly at some level, there will be errors in the CQP calibration numbers, but they are not obvious from this measurement; CMM measurement error and movement of the beam are likely to be the dominant sources of error in this measurement. From the graph, we can draw reasonable estimates for the typical accuracy of the CQP of $\pm 4\,\mu$m and $\pm 20\,\mu$rad, which is compatible with the requirements outlined in Section 3.1.

3.5 Improvements to the CQP

3.5.1 Problems of the current design

During early testing of the CQP, one major issue discovered was with calibration parameters drifting over time. Checks, of the type detailed in Section 3.4, indicated large errors in the values of the calibration parameters. Subsequent re-calibration of the CQP would lead to improved performance, but only for a short period of time. In the course of investigating the source of the drift many calibration procedures were carried out. Figure 3.15 shows the drift in the measured calibration parameters as a function of time.

The most noticeable shift is a change in the value of θ_x between the 2^{nd} and 3^{rd} calibrations of over 8 millidegrees ($130\,\mu$rad). A large number of potential sources of the drifts were investigated including mechanical deformation of the CQP structure, drifts in the electronics, temperature sensitivity, systematics in the CMM, movement of the diode elements, possible birefringence of the beamsplitter and issues with the calibration procedure itself. Only negligible effects were found from any of these potential sources. One clue was in the fact that the drift in the distance parameters is noticeably less than the drift

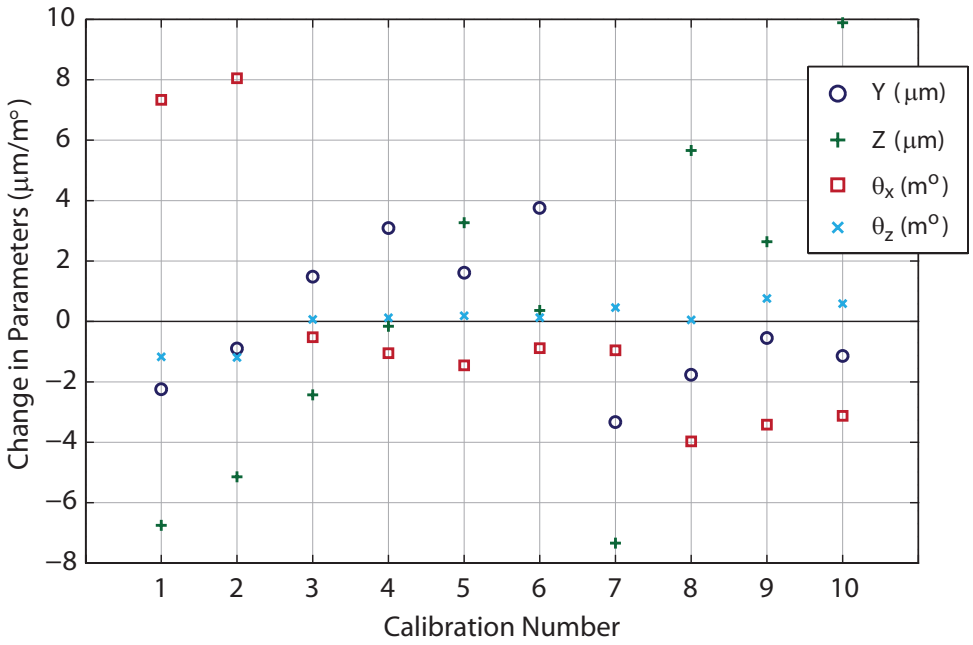

Figure 3.15: *Plot showing the drift in CQP calibration parameters over a time period of 2 months, values are residuals with respect to the mean calibration parameters. One millidegree is equal to* 17.5 μ*rad.*

in the angular parameters. Because the origin of the CQP is located beside the beamsplitter (and consequently QPD1), the effect of any change in the beam path to QPD2 couples significantly more to the angular calibration parameters than to the distance parameters. The drifts in the parameters then indicates that the source is probably somewhere in the path to QPD2, and not related to QPD1 or the beamsplitter.

The problem was eventually determined to be in the mirrors, with the most likely cause being expansion or contraction of the small spots of glue securing the mirrors to the Invar® mounts. Due to the path being folded, a change in angle of mirror 1 of 20 μrad will move the beam at QPD2 by $\sim$ 7 μm. This corresponds to expansion or contraction of one of the glue spots by only $\sim$ 500 nm. Schedule implications for the construction of the LISA Pathfinder

OBI (see Chapter 5) meant that little time was available to fully investigate this phenomenon or to implement a revised design of CQP. Instead, the two mirrors were removed from the CQP and QPD2 was moved to the location of mirror 1. The unavoidable side effect of this was to decrease the optical baseline from $\sim$ 44 cm to approximately 12 cm. This increased the angular uncertainty involved in centring the beam on the CQP to $15-20\,\mu$rad ($\pm 2\,\mu$m over 120 mm). Despite the drawbacks, it successfully solved the issues with drift in the calibration parameters and the reduced angular accuracy is still within the required range. A photo of the modified CQP can be seen in Figure 3.16.

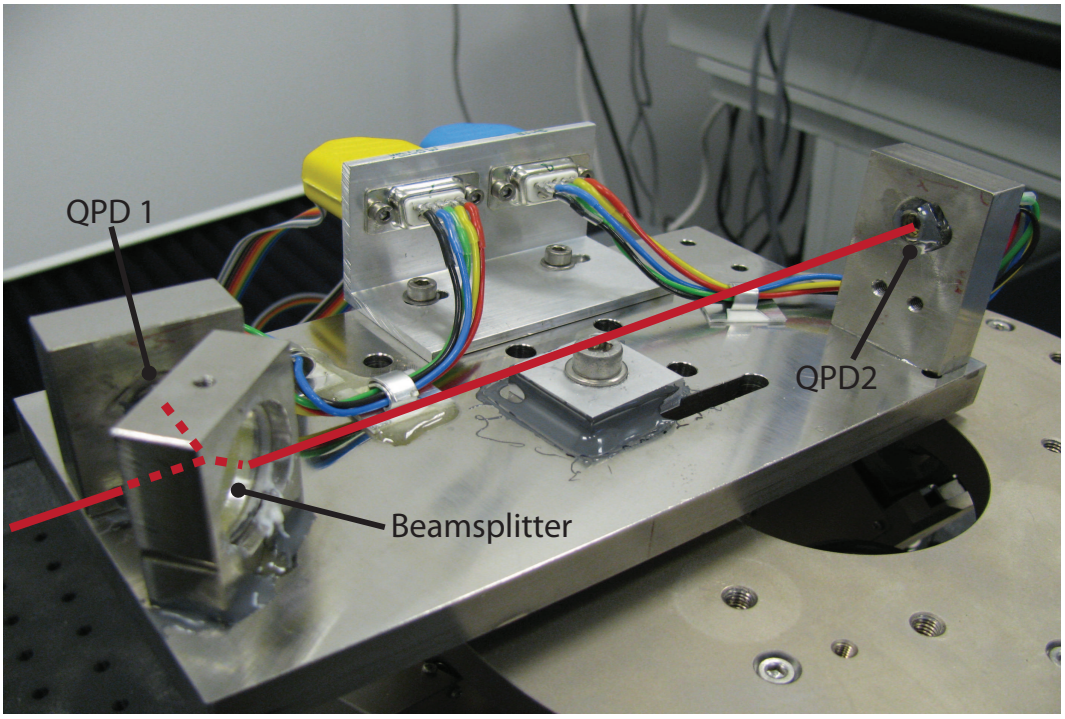

Figure 3.16: *Photograph of the modified CQP, QPD2 has been moved to the previous location of mirror 1.*

A similar effect will also be present in the beamsplitter, which is mounted in an identical way to the mirrors. However, since the path of the reflected beam is only about 20 mm to QPD1 the effect on the calibration parameters

is negligible, and the coupling of beamsplitter angle to lateral displacement of the transmitted beam is very weak.

3.5.2 The mkII CQP

One obvious way to improve the CQP is to revise the design to not be reliant on glue for securing components. This will allow a longer optical baseline and improved accuracy over the modified CQP. A new version of the CQP is currently being designed, and will be constructed from a Zerodur® baseplate and use hydroxide catalysis bonding to secure the mirrors and beamsplitter. The QPDs can be mounted in either Invar® and glued down or preferably fused silica or Zerodur® mounts which are also bonded.

3.6 A measurement of the optical centre of a beam

As was briefly discussed in Section 3.1, there are two obvious ways to define the centre of a beam; the power (or intensity) centre and the optical centre. The CQP uses the power centre as its definition, and this was adopted as the definition of beam centre for LISA Pathfinder. For a 'real' beam, the power centre and the optical centre are liable to be different. Information on the degree of how difference between these two definitions could be important for developing beam measurement systems for LISA.

3.6.1 The diffraction sensor

A precise measurement of the optical centre is difficult. One way to do it is to use the diffraction pattern of the beam made by a cross hair. Viewing the diffraction pattern on a CCD camera and symmetrising the diffraction pattern by moving the cross hair will place the cross hairs close to the optical centre of the beam. Since symmetrising the diffraction pattern involves an intensity measurement using the CCD, this is not technically a *pure* measurement of the optical centre, but it does closely approximate the optical centre.

A simple stable cross hair was constructed by mounting orthogonal wires into an aluminium block. These were glued in place, and a glass cover slip was glued over the top to protect the wires and ensure they were not disturbed. This diffraction sensor was then calibrated, in a manner very similar to the CQP as described in Section 3.3. Since there was only one cross hair however, there is no direction component and so only two distance offsets, describing the location of the centre of the wires in relation to the aluminium block are required. Measurement of the diffraction sensor with the CMM then allows a point to be constructed, which will represent the centre of the beam being measured. By making several spatially separated measurements of a beam, the fit to the centre points will give a line representing the beam. The diffraction sensor is shown in Figure 3.17. Using the 2D cross-section of the measured diffraction pattern, changes are observable for movements of the cross hairs (which are 210 μm wide) down to $\sim 1\,\mu$m for a beam with 1 mm diameter.

Measuring a beam with this tool requires that care is taken over projection effects of the measurement. It would be possible, for example, to have the body of the diffraction sensor at an angle to the beam (say 1°) and still produce a good diffraction pattern. When the sensor was measured, however, there is an

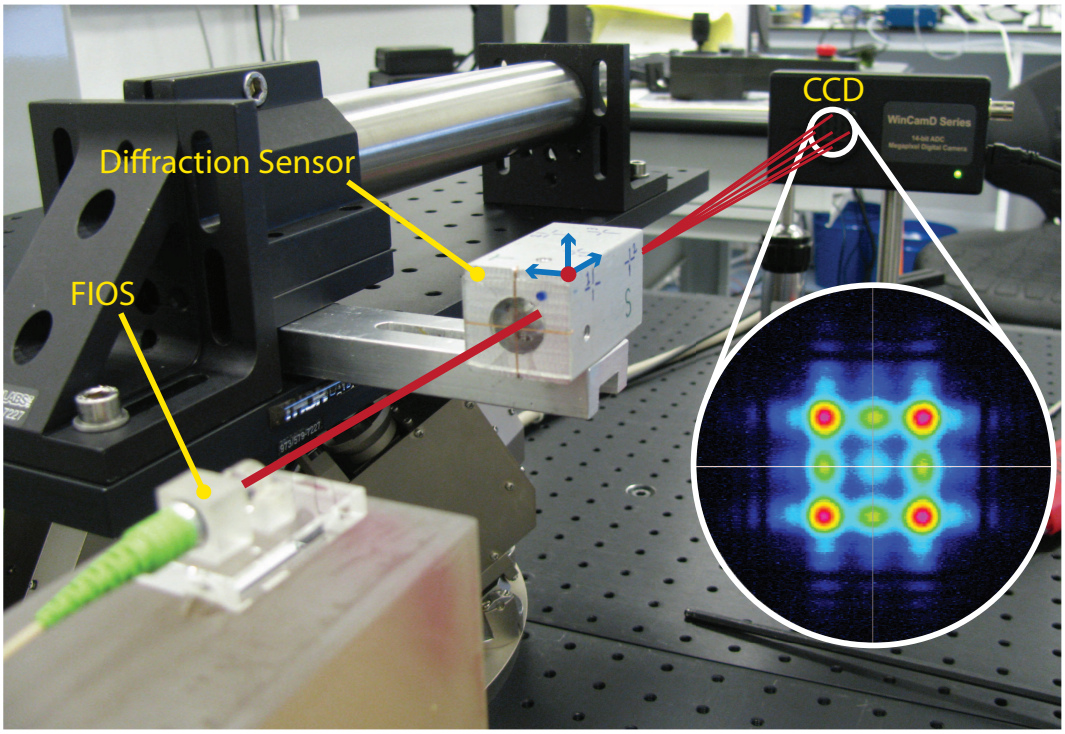

Figure 3.17: *Illustration of the diffraction sensor, shown measuring a beam with the typical diffraction pattern from a* 1 *mm beam inset.*

unavoidable internal assumption that the cross hairs are square to the beam so a rotation would lead to a point slightly offset from the true centre being constructed. This is a cosine effect though, so it is a weak function of angle. Requiring that this effect is $< 1\,\mu$m gives a constraint that the body of the diffraction sensor is kept to within 0.5° of the beam axis. In practice, the sensor is used with a rail system to slide it along the beam for multiple measurements. Using the CMM it is possible to align this to $< 0.1°$ to the beam with ease, thus keeping the projection effects at an insignificant level.

3.6.2 Comparing the diffraction sensor to the CQP

Using a stable reference beam, measurements of its position were made with both the CQP and the diffraction sensor as a means to assess the collinearity of the two measurement techniques. Two CQP measurements and four diffraction sensor measurements were made over a range of $\sim 300\,\mathrm{mm}$, giving four measurement points per device. Internal to each device, the points all lay $< 1.5\,\mu\mathrm{m}$ from the reconstructed beam line indicating a good fit to the beam for each technique. To asses the collinearity, the distance from one measured beam to the other was calculated at two spatially separated planes, 300 mm apart. This process was then repeated a number of times. The results are illustrated in Figure 3.18 in which the x-axis (pointing out of the page) is the specific measured beam from the diffraction sensor for each measurement. The relative position of the CQP measured beams are plotted at the two planes.

The plot shows that not only is there a spatial separation of the two beams, but also an angular separation too since the distance from one measured beam to the other changes along the length of the beam. From the figure, we can conclude that the two systems agree on the position and direction of a beam to $\lesssim 20\,\mu\mathrm{m}$ in position and $< 30\,\mu\mathrm{rad}$ in angle.

Some difference in beam position was expected when measuring a real beam with two different methods since a real beam will always have abberations that could give different values to the power and optical centres of that beam. The value of $20\,\mu\mathrm{m}$ is interesting, because it is similar in magnitude to some of the centring requirements that exist for alignment of the various beams for both LISA Pathfinder and LISA (see Chapter 2). This means that while a beam could be in specification under one definition, it could potentially be non-compliant under the other definition. The angular deviation is also interesting,

the good beam fits internal to each measurement suggest that is a systematic effect, possibly of the beam itself but more likely related to the CMM. The value of 30 μrad is below the combined CMM measurement accuracy for the CQP and the diffraction sensor, so it is difficult to conclude much from this.

The CQP was developed to enable construction of the LISA Pathfinder OBI, for which the power centre was chosen to define the beam centre. For LISA, which potentially has increased requirements on beam centring, further investigation of the differences between the definitions of beam centre and their relevance to LISA is required.

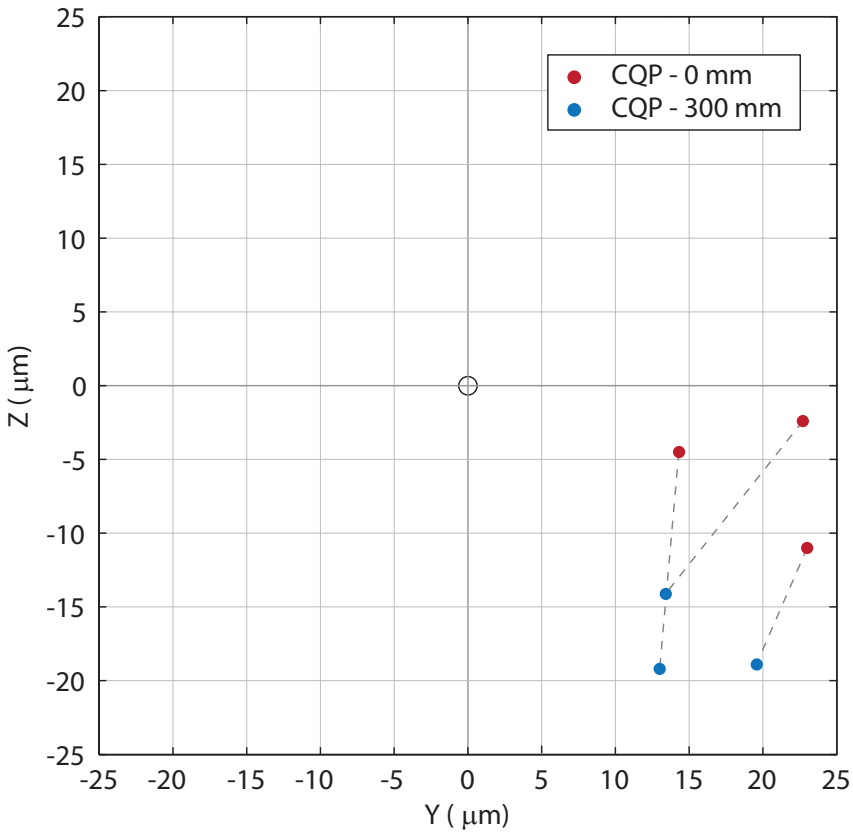

Figure 3.18: *Plot showing the relative coaxiality of multiple CQP measurements against diffraction sensor measurements of a single beam. For each of the three measurements shown, the stable beam was measured with both the CQP and the diffraction sensor, and the x-axis represents the specific diffraction sensor measured beam associated with each CQP measurement. Therefore, the uncertainty in the position of each of the CQP measurements is the combined error of the diffraction sensor and the CQP, around $\pm 10\,\mu m$ and $\pm 30\,\mu rad$.*

Chapter 4

Alignment and construction of precision interferometers

The construction of fully bonded monolithic interferometers like those introduced in Chapter 2 presents some challenging requirements. In addition to the ability to measure a beam to the few μm and μrad level as discussed in Chapter 3, we must also be able to manipulate the beam (or more accurately, an optical component which will affect the beam) at this level of precision.

Many of the alignment requirements (such as test mass centring for example [35]) require alignment in four degrees of freedom - two directional and two angular. Such control is extremely difficult to achieve simultaneously. One possible solution is to separate out the alignment into two stages with, in each step, two degrees of freedom (one directional and one angular) being controlled. This is illustrated in Figure 4.1. In this example a beam is incident on a mirror along the x axis and reflected through 90° along the y axis. In this case we restrict the beam to the x-y plane, eliminating the degrees of freedom θ and z. Actuation of the mirror around ϕ and along the line $y = x$ will then adjust the

beam in x and ϕ. These are designated as the 'in-plane' degrees of freedom.

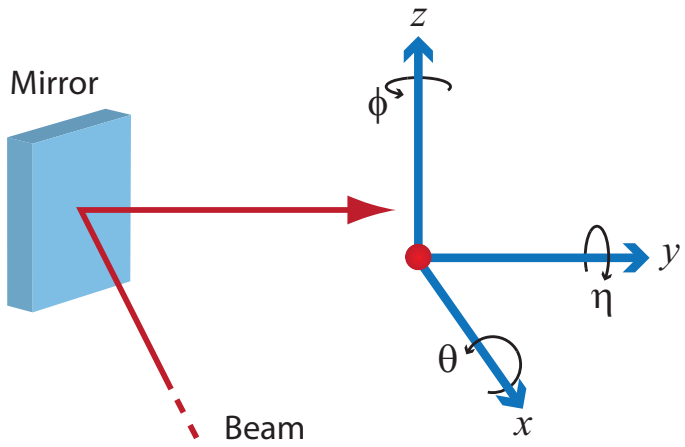

Figure 4.1: *Diagram showing the coordinate system and the degrees of freedom for adjustment of an optical beam.*

The z and θ degrees of freedom (the 'out-of-plane' degrees) can be controlled through manufacturing tolerances. By having a sufficiently flat baseplate, components which have their reflecting surfaces sufficiently perpendicular to the bonding surface, and a uniform bond layer, a beam which is injected into the interferometer with the appropriate alignment in z and θ will stay aligned in these degrees of freedom at all points.

The requirements on how perpendicular a component will need to be, and how flat a baseplate is required to be, depend on the layout of an interferometer and the beam alignment tolerances required. Typically, large surfaces can routinely be polished to have a global flatness of $\lambda/4$[1] over length scales of 100 mm and components can be created with perpendicular surfaces to sub-arcsecond accuracy. The hydroxide catalysis bonding process gives a bond layer which is typically ~ 100 nm in thickness and sufficiently uniform that any angular errors introduced through the bond layer being wedged are a second

[1]For specifications on optical flatness, the industry standard is to use a λ of 633 nm

order effect, contributing small fractions of an arcsecond to perpendicularity errors [36]. For most interferometers with beam path lengths of order 1 m, these manufacturing tolerances typically give out-of-plane errors of the order 20 μrad, which is broadly compatible with the typical alignment tolerances of LISA Pathfinder and LISA discussed in Chapter 2.

4.1 Allocating alignment tolerances

One approach to the alignment of an interferometer would be to precision manipulate every component, so that the final assembly was as close to the nominal design as possible. This approach is unattractive however, since the precision placement of components is time consuming. In many interferometers the tolerances can be redistributed among the various components, leaving a collection of components which can be placed with comparatively loose tolerances and another set which must be placed with increased accuracy. These are classified as 'non-critical' and 'critical' components respectively. The distinction is best illustrated with an example.

Figure 4.2 schematically depicts a pair of simple Mach-Zehnder interferometers. One, combined at BS4 and readout at PD2, is a reference interferometer and the other, combined at BS2 and read out at PD1, is the measurement interferometer which interrogates the Test Mass. If we require that the beam is to be centred to within $\pm 25\,\mu$m on the centre of the Test Mass, then clearly component M1 must be precision placed in order to achieve this. Further, we would wish for the two read-outs to have high interference contrast so the combination beamsplitters BS2 and BS4 must also be placed with high precision. The remaining components however are all non-critical. Errors in the placement of BS1 can be taken up by altering the position of M1 and BS4 while BS3

can be compensated by the location of BS2 and M2 similarly compensated by BS4. By placing the tight alignment tolerances on three of the components, we have halved the number of precision steps required to construct the interferometer. It should be noted that this argument only applies to in-plane alignment tolerances, the requirements on component perpendicularity and baseplate flatness remain unchanged.

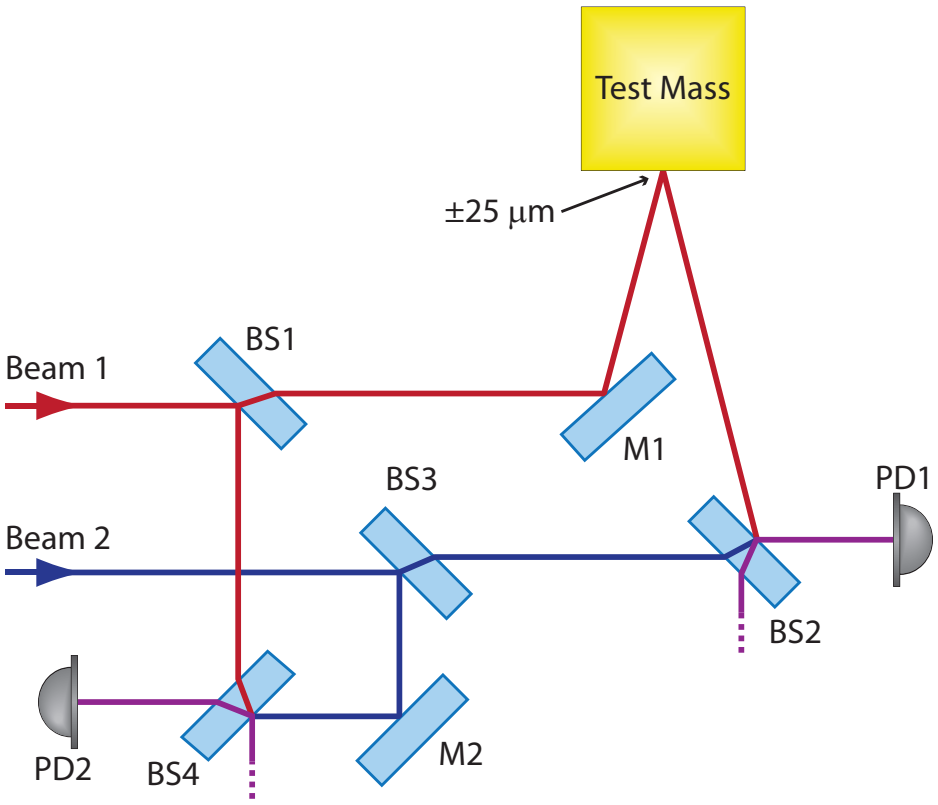

Figure 4.2: *Schematic layout of a pair of Mach-Zehnder interferometers. Component M1 steers the beam onto the Test Mass and components BS2 and BS4 combine the two input beams to give both a reference and a measurement readout signal.*

4.2 Template bonding

The tolerances on non-critical components is dependant on the alignment requirements and specific layout of the interferometer. In general, it is usually possible to use a metal template to define the location of such components. This has the added advantage that several components can be bonded at once, dramatically reducing the amount of time it takes to construct a bonded interferometer. Figure 4.3 shows an annotated photograph of such a template, used for part of the construction of the LISA Pathfinder OBI (see Chapter 5).

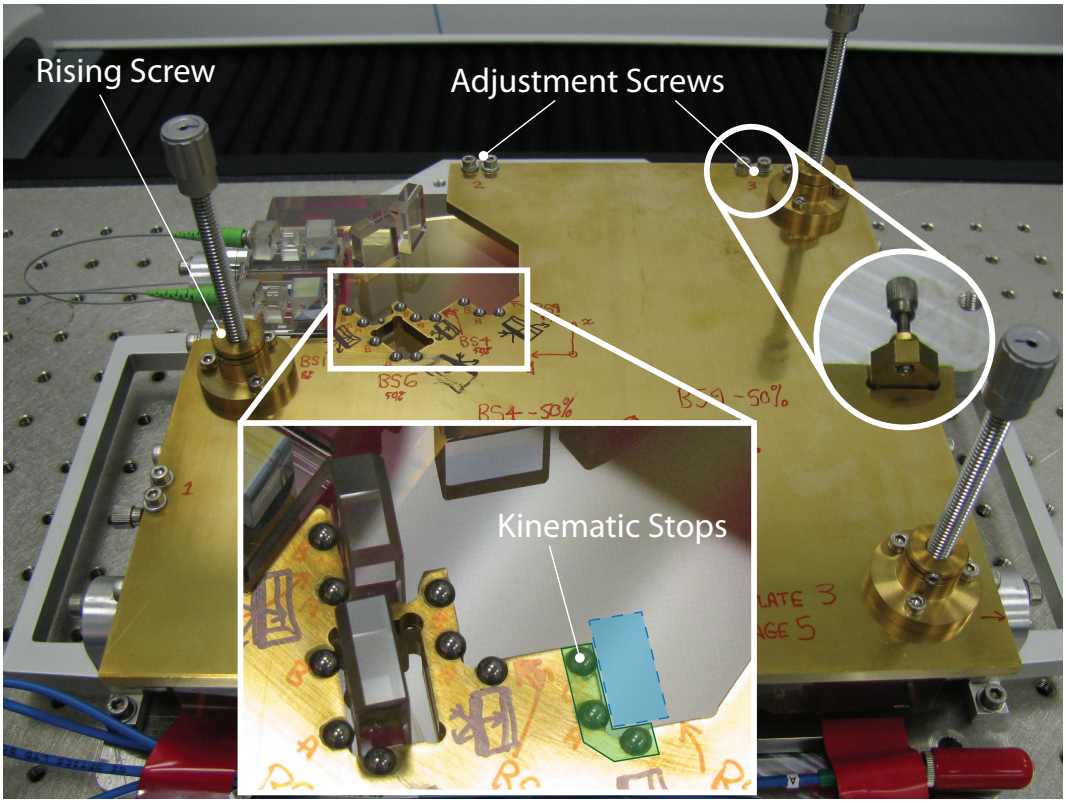

Figure 4.3: *Annotated photograph of a bonding template, used in the construction of the LISA Pathfinder OBI which can be seen underneath.*

The underlying principle is that the components are located against three ball bearings, which form a set of kinematic stops which define the location of the

component (shaded green in the figure). The reflecting/splitting surface sits against two ball bearings which are on the same side (the front locating ball bearings). These define the optical position of the component and the third ball bearing controls the component in the insensitive direction parallel to the surface. The template sits slightly above the baseplate surface on three ball bearings, and the entire assembly is inclined to an angle of $\sim 5^\circ$ so that the gravitational restoring force holds the component against the stops.

The x-y position of the template is set with another set of kinematic stops, which hang underneath the template and locate against the sides of the bench. Two are on the side which is raised to provide the inclination and they hold the template in place and one on an adjacent side. It is possible to have these as simple ball bearings, but in the case of the template shown in the figure, they are attached to fine pitch threaded screws. This provides adjustment of the entire template in the plane of the bench. Three additional screws can also be seen in the figure. These are to raise the template up from the surface of the bench once the bonds have cured to allow the template to be removed safely without risking damage to the optical surfaces.

4.2.1 Template alignment and accuracy

The template shown in Figure 4.3 was manufactured using a 5-axis CNC (Computer Numerical Control) vertical milling machine, manufactured by HAAS, model VM-2SW [45]. Flat bottomed holes were machined into the brass template body and tightly toleranced 4 mm stainless steel ball bearings were glued into these holes. The use of the high accuracy CNC mill already ensures a high degree of accuracy in the manufacture of the template, but further optimisation is possible.

The holes have to be machined with respect to the brass template, therefore tolerance errors in the size of the brass will couple systematically into the location of the holes. Angular systematics are also possible, and the machine itself has an associated error of $10 - 20\,\mu$m. Since the templates have adjuster screws defining the position in x and y, we have the ability to compensate for these errors.

By measuring the actual location of the ball bearings using the CMM, the true positions can be compared to the nominal positions which come from the master CAD model. This will give a set of projected angular and positional deviations. The angular deviations come from the combined error of the two front locating ball bearings. Coordinate rotations and translations can then be applied to the measured values, minimising the deviations to obtain a best fit of the manufactured template to the ideal model. For a specific template, it is also possible to again apply a critical and non-critical subdivision to the components, optimising the template position further to reduce errors on one component at the expense of another.

Using the optimised positions of the ball bearings, we can calculate a set of target coordinates in the reference frame of the optical bench. When the template is in place on top of the optical bench, the ball bearing positions can be measured in the bench frame and iteratively aligned to the correct position using the the CMM and the three adjuster screws. This can typically be done to an accuracy of a few μm.

Table 4.1 compares the projected positional and angular errors in the placement of components before and after the optimisation process. The template was used in the construction of the LISA Pathfinder OBI.

The baseline of the two front locating ball bearings in the LISA Pathfinder

Table 4.1: *Projected positional and angular errors of the components to be bonded by a template, before and after the optimisation process. The component names correspond to those given in Figure 2.4 on Page 20. In this specific case, BS11 was given a large angular deviation to reduce the errors on the other three components, since the beam reflected from BS11 propagates to a power monitor photodiode. This is a single element device and as such has extremely loose alignment tolerances.*

Component	Before optimisation		After optimisation	
Number	Position (μm)	Angle (°)	Position (μm)	Angle (°)
BS11	23.4	0.005	36.1	0.155
BS4	16.1	0.089	11.4	0.061
BS9	20.1	0.146	6.4	0.004
BS6	35.4	0.216	22.9	0.066

templates was 10 mm, which is why deviations of only $\sim 30\,\mu$m can couple to produce angular deviations at significant fractions of a degree. In the above example, the beam reflected from the first component only had a short baseline. This allowed it to have a larger angular error assigned to it to give the other components smaller angular deviations. If we take as a worst case typical deviation $\sim 0.1°$, this will result in a lateral beam deviation after a path length of 0.5 m of ~ 1.7 mm. Provided an optical layout has sufficient clear space around critical components to allow for movement to compensate for the accumulated deviations, this is an easily manageable error build-up.

4.3 Precision bonding

The bonding of critical components requires extremely fine control over the in-plane degrees of freedom, ideally adjusting the component down to the few μrad level of precision. As with template bonding, using a system of three kinematic stops is the preferred method to locate a component. For precision control, we can actuate the two front locating stops. This provides a mechanism for adjusting the component in place on the optical bench, provided it is free to move on the surface without optical contacting. However hydroxide catalysis bonding only allows adjustment of a component for $30 - 60$ seconds after application of the bonding fluid. This is insufficient time to align the component to the required accuracy. If a slowly evaporating buffer fluid (such as octane) is placed between the component and the baseplate then an iterative alignment is possible, applying the buffer fluid and adjusting, then reapplying and readjusting iteratively until the component is in its desired position. Once aligned, the bonding fluid can be applied and the component relocated against the stops. To prevent contamination to the bonding surfaces, the buffer fluid must have a very low evaporation residue. This technique was originally developed for construction of the prototype optical bench in Glasgow and for the engineering model of the LISA Pathfinder OBI, and has since been advanced at Glasgow for the building of the LISA Pathfinder flight model [27].

4.3.1 Control of the component

The adjustable kinematic stops used are ruby balls on carbon fibre shafts, these are attached to piezoelectric linear actuators which have 10 nm step size over a range of 30 μm. These actuators are then attached to manual translators which give course control at the 10 μm level over 10's of mm. The third stop (or side-

stop) is stationary since this only positions the component in the insensitive lateral degree of freedom. The actuators are shown in Figure 4.4.

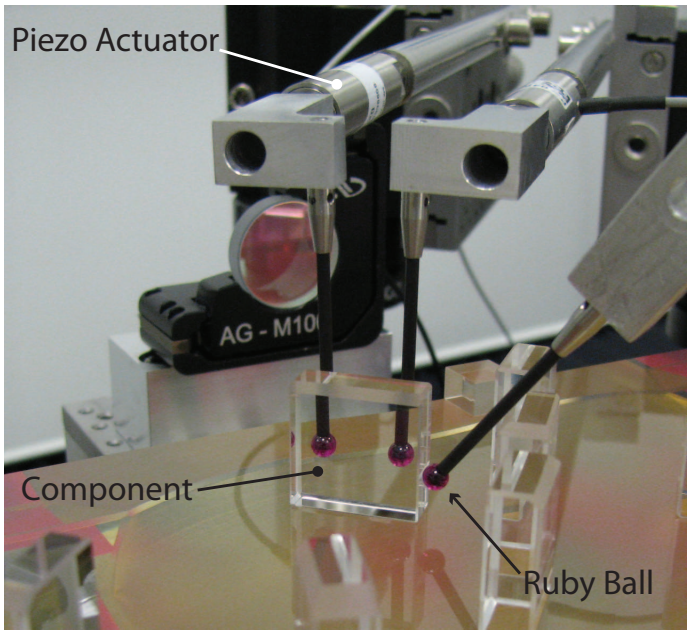

Figure 4.4: *Photograph showing the precision component actuators.*

The two front locating stops allow full control over the in-plane degrees of freedom of the component. See Figure 4.5. Common mode actuation of both stops will give a lateral translation of the beam, with the magnitude being $2/\sqrt{2}$ times the length of the stroke for a 45° reflection. Differential actuation will give an angular translation in ϕ, *i.e.* about z. The magnitude of this is dependant on the baseline between the stops. For LISA Pathfinder, the components were between 15 and 20 mm wide, and the stops were typically $10-12$ mm apart. This results in a 1 μm differential movement of the actuators rotating the component by 100 μrad, which is a beam rotation of 200 μrad. Achieving alignment requirements at the few μm and $\sim 20\,\mu$rad level therefore requires sub-micron control over the actuators.

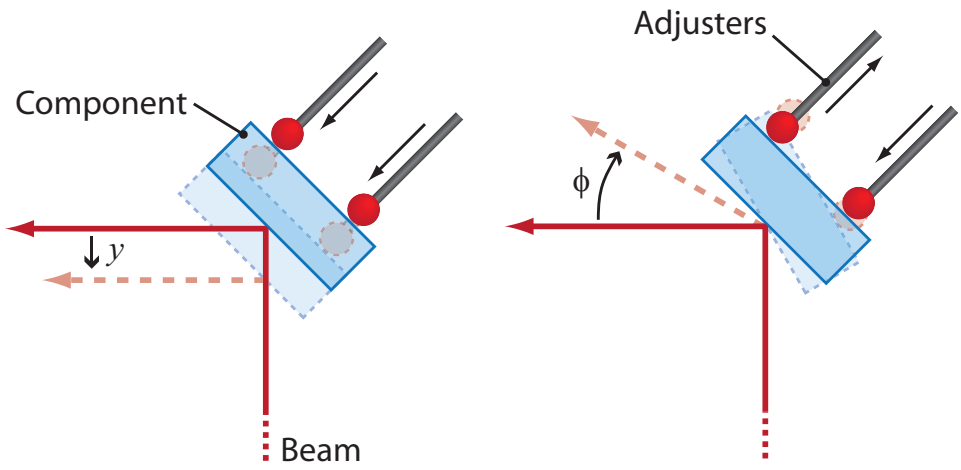

Figure 4.5: *Diagram illustrating control over the in-plane degrees of freedom of a component using two precision adjustable actuators.*

4.3.2 Alignment to a target

Broadly, there are two types of precision alignment: alignment of a beam to an ideal beam, such as aligning to a Test Mass nominal reflection point; and alignment of a combined beam.

For alignment to an ideal point or beam direction, the CQP is used. As discussed in Chapter 3, the CQP is calibrated with the result that the nominal beam vector which will be centred on both photodiodes is known with respect to the metal structure of the CQP. Figure 4.6 illustrates the alignment of a component to an ideal beam. The theoretical beam, shown as a black dashed line in the figure, is generated with respect to the baseplate geometry. The CQP nominal vector (shown as a red dashed line) is then aligned to be coincident with the theoretical beam through an iterative alignment process using the CMM. The transfer function of the hexapod coordinate frame (on which the CQP is attached) to the reference frame of the optical bench is then established, such that the deviations of the CQP nominal vector from the the-

oretical beam can be quickly derived into a set of translations and rotations of the hexapod in order to achieve optimal relative alignment.

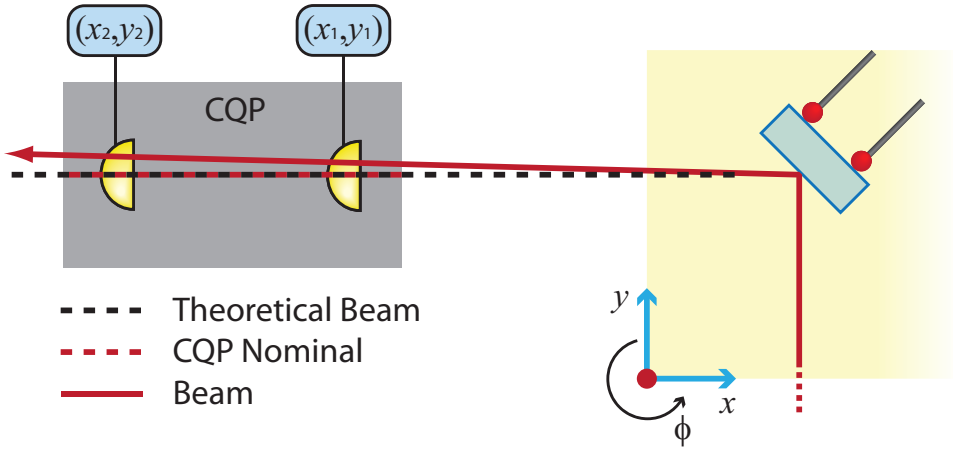

Figure 4.6: *Diagram showing the principle behind the precision alignment of a beam to a nominal beam, such as one which is to be incident on a Test Mass.*

The component - floating on the buffer fluid - can then be adjusted using the actuators. This will adjust the beam pointing towards the CQP, and consequently change the read-out position of the beam on the two photodiodes. These positions are read out as cartesian spot positions at the photodiodes, called (x_1, y_1) and (x_2, y_2) (see Section 3.2.3). Note that these x and y are *different* from the x and y of the reference frame. With the CQP nominal vector coincident with the theoretical beam, any beam which will read out as being centred on the two photodiodes (*i.e.* $x_1 = y_1 = x_2 = y_2 = 0$) will then have the same equation as the theoretical beam.

For alignment of a combination point, the interference contrast provides one possible error signal for relative beam alignment. This simply requires that a single element photodiode be placed on the beam in order to calculate the contrast value. Contrast is, however, a relatively weak function of beam properties. Differential wavefront sensing (DWS) signals are considerably more

sensitive, and are also very relevant for LISA Pathfinder (See Section 2.2.1 on Page 12 and Chapter 6). DWS is read out using a quadrant photodiode, and provides an error signal at a combination point that is sensitive to relative beam movements at the $\sim \mu$rad level, with the goal being to minimise the relative wavefront tilt. A single quadrant photodiode, centred on the recombined beam to a few 10's of μm is sufficient to provide a good DWS signal.

4.3.3 Achievable accuracy

The minimum increment of the piezoelectric actuators is of order 10 nm, which is sufficient to actuate the component angle down to sub μrad level. Typically, the repeatability of taking the component away and replacing it with more buffer fluid or bonding fluid determines the ultimate accuracy of the precision bonding technique. The repeatability is variable with specific set-up, but typically is better than 100 nm at a single stop, giving angular repeatability of a reflected beam at $< 20\,\mu$rad for a component which is of order 2 cm wide. A final 'tweak' of the component is possible once the bonding fluid has been applied, but the short time frame in which this can be achieved, combined with the possible risks, makes this an unattractive option in all but the worst-case circumstances.

A plot showing the CQP read-out during the final alignment stages of a component (specifically FIOS1 on the LISA Pathfinder flight model OBI, see Chapter 5) is shown in Figure 4.7. The two time series in the figure are the in-plane spot positions at the front and back photodiodes (x_1 and x_2). The CQP was positioned ~ 300 mm from the component, and the inter photodiode spacing is 12 cm. The accuracy of alignment was at the few μm and 10 μrad level, which is below the typical alignment requirements for LISA Pathfinder and

LISA optical alignment.

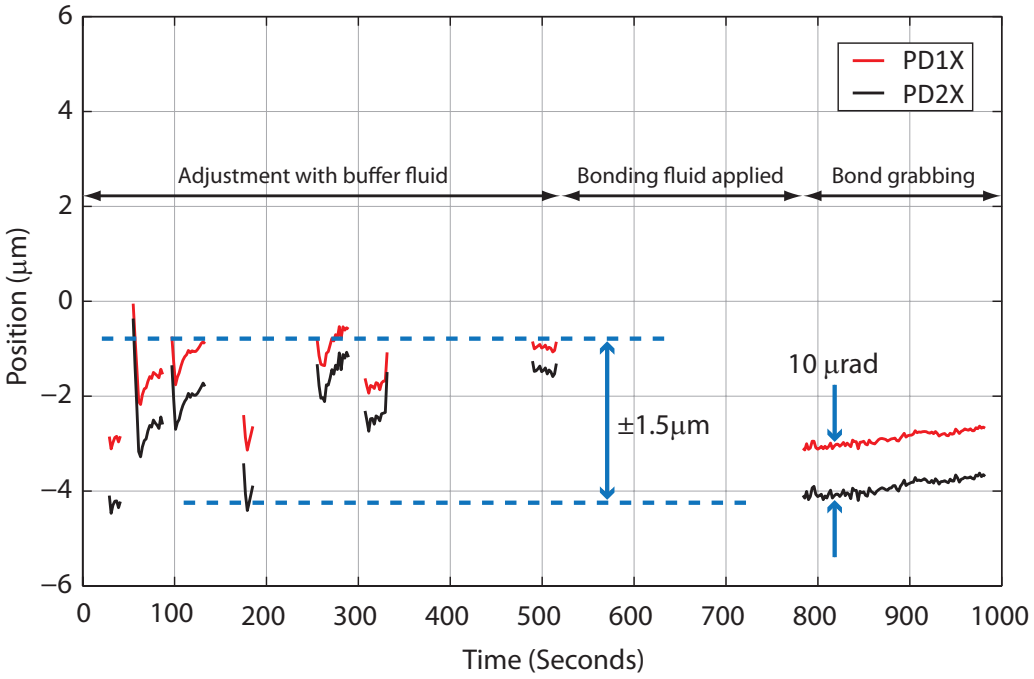

Figure 4.7: *CQP read out of the final alignment stages of a component with precision bonding. The two traces represent the in-plane spot positions of the beam on the front and back photodiodes of the CQP. During the adjustment phase, the peak-to-peak movement of the two traces ($\pm 1.5\,\mu m$) demonstrates the repeatability of placing the component back against the stops. The separation between the two traces, over the baseline of the QPD's (120 mm) then yields the angular deviation of the beam from the theoretical beam, in this case 10 μrad.*

Chapter 5

Construction of the LISA Pathfinder optical bench interferometer

The optical bench interferometer for LISA Pathfinder, introduced in Chapter 2, is one of the core components of the spacecraft. This chapter details the construction process of the Optical Bench Interferometer (OBI) and the accuracy achieved in relation to the requirements outlined in Section 2.2.2. Two OBIs were built, a flight model and a flight spare. The construction process detailed is identical for both OBIs, with the exception that, at the time of writing, the flight spare has not been fitted with flight photodiodes.

Throughout this chapter and also in Chapter 6, extensive references will be made to the coordinate frame of the OBI, the OBF (optical bench reference frame). The OBF is represented diagrammatically in Figure 5.1, but broadly is established such that the origin lies in the centre of the OBI, with the surface of the bench forming the x-y plane. The x-axis is in the direction of test

mass 1, and positive z points up from the surface of the OBI [35]. The OBF is defined by measuring a series of points on the surfaces of the OBI with the CMM. Care is taken with the measuring routine to ensure that the same frame is constructed each time as the repeatability of the frame is crucial to the alignment strategy.

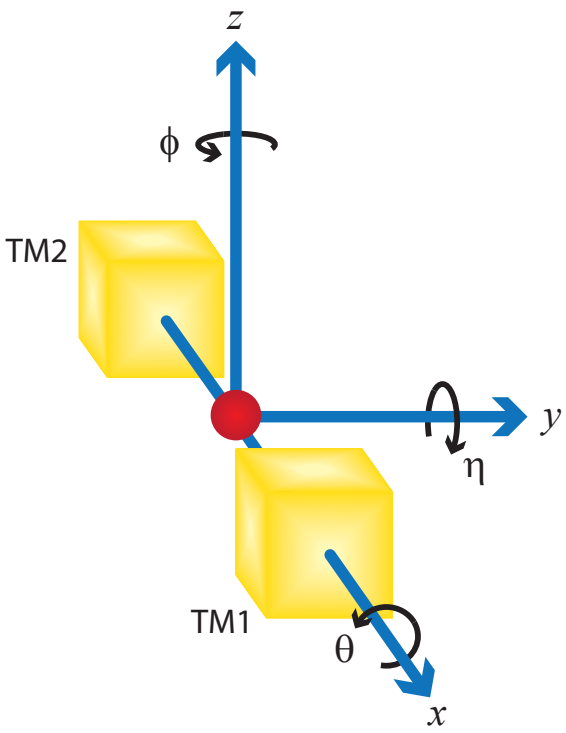

Figure 5.1: *Diagram illustrating the coordinate frame of the OBI.*

5.1 Alignment plan

Chapter 4 introduced the principles behind the construction of precision monolithic interferometers like the OBI. The exact sequencing of the construction, and the techniques used, is dependant on the specific layout. Extra care must

be taken to ensure that beams which may be critical to the alignment of one component are not inadvertently blocked by another previously bonded component. For the OBI a carefully conceived alignment plan was developed which separates the construction out into 17 individual stages. These are illustrated graphically in Figure 5.2, and summarised as follows:

- two stages to precision bond the fibre injectors using the CQP as a target;
- six template bonding stages, comprising a total of 14 components;
- two stages to precision bond the optics directing the beams to the two test masses, using the CQP as a target;
- three stages to precision bond components that together determine path length matching;
- four stages to precision bond the beam combiners for each of the interferometers.

5.1.1 Fibre injectors

To meet the beam stability requirements for LISA Pathfinder, custom quasi-monolithic fibre injectors were designed and constructed for the OBI, called the FIOS (fibre injector optical subassembly). Specific details of the design can be found in [46] and [47], but broadly it consists of a fused silica mounting block into which a single mode polarisation maintaining fibre is glued using an optical adhesive. Strain relief is applied and the front face of this block is then polished flat with an 8° angle to mitigate against back reflections. This block is then hydroxide catalysis bonded to a small fused silica baseplate, 20 mm × 33 mm × 5 mm. A collimating lens - itself glued into a silica U-groove

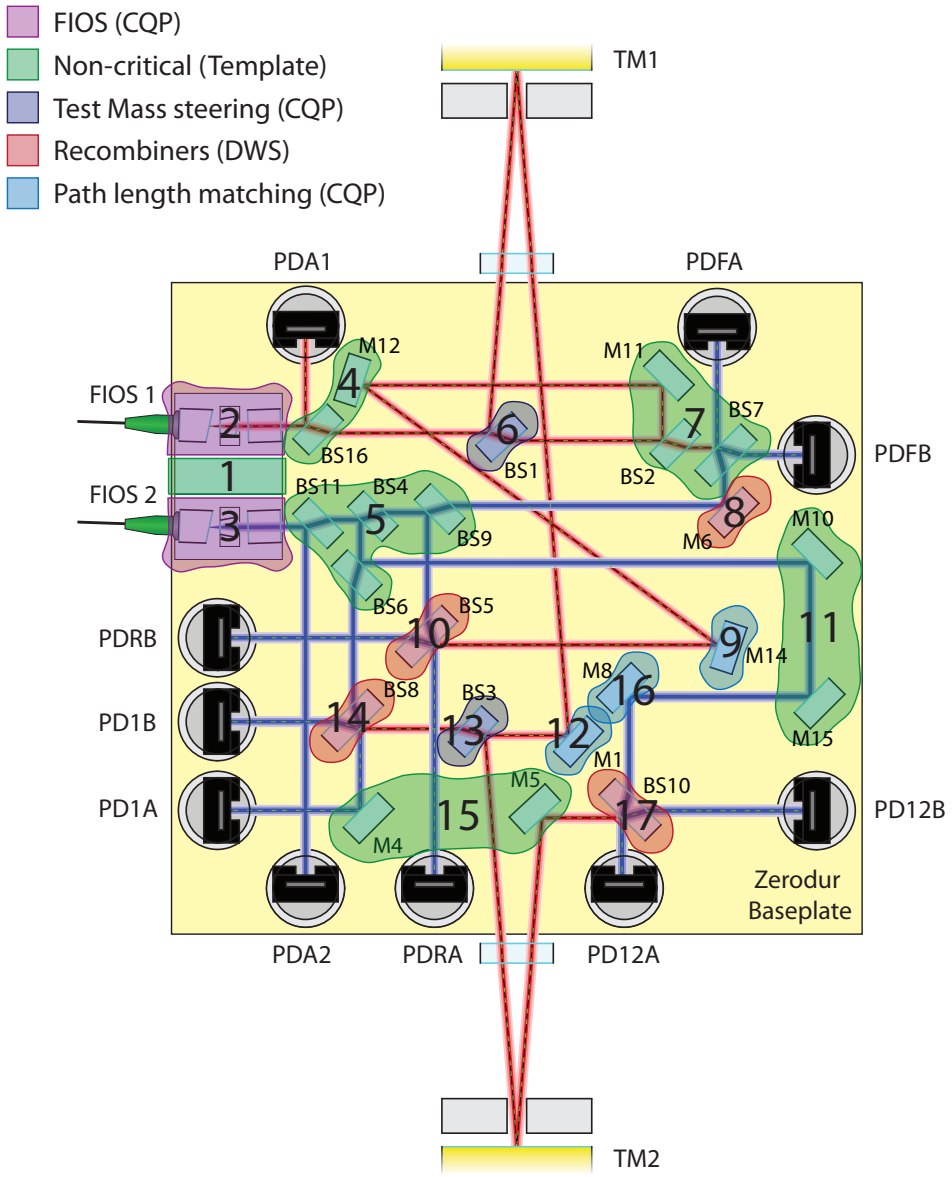

Figure 5.2: *Diagram showing the bonding order for the OBI components.*

- is then precision bonded to the baseplate to produce a collimated beam. Finally, a polariser is glued after the lens to clean up the output polarisation state from the fibre. This creates a small, stable and rugged subassembly which can then be bonded to the OBI. An annotated picture of a FIOS can be seen in Figure 5.3.

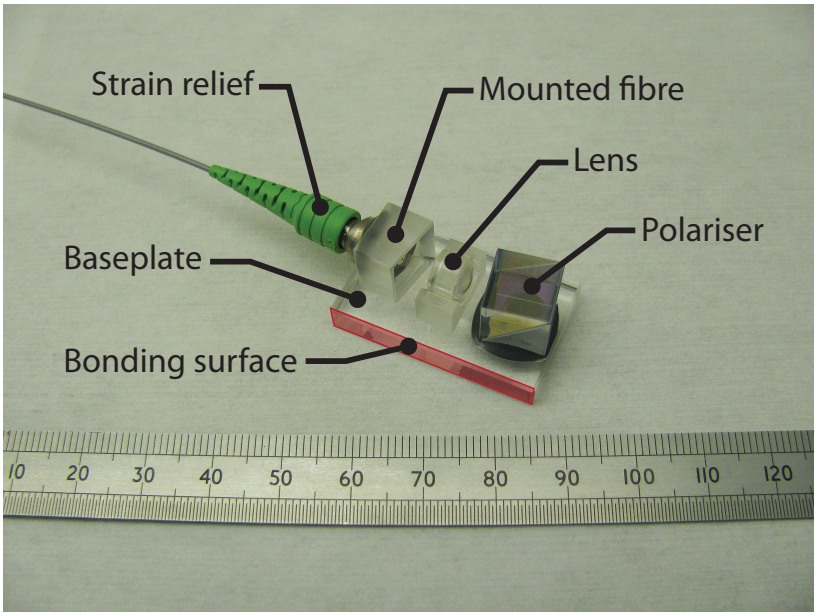

Figure 5.3: *Annotated picture of a qualification model FIOS.*

The alignment of the FIOS with respect to the optical bench is critical. In line with the philosophy outlined in Chapter 4, control over the out-of-plane degrees of freedom of the beam requires that the beams are launched onto the optical bench parallel to the x-y plane to within $\sim 25\,\mu$rad and within $20\,\mu$m of the nominal beam height. The rapidly diverging beam from the fibre creates a situation where the beam angle is a very sensitive function of the lateral lens alignment, the result is that creating a FIOS where the beam emerges parallel to the baseplate through tolerancing alone is virtually impossible.

The solution is to bond the FIOS to an intermediate post *via* its side. In this way, the height and out-of-plane angle of the beam can be controlled through precision bonding. The intermediate post is a template bonded component and is the first item to be bonded to the baseplate. Once cured, the entire OBI can be oriented vertically which presents the side of the post as a horizontal bonding surface. The CQP is positioned on the theoretical beam and the FIOS aligned to it, ensuring the correct beam height and angle. This is illustrated

in Figure 5.4.

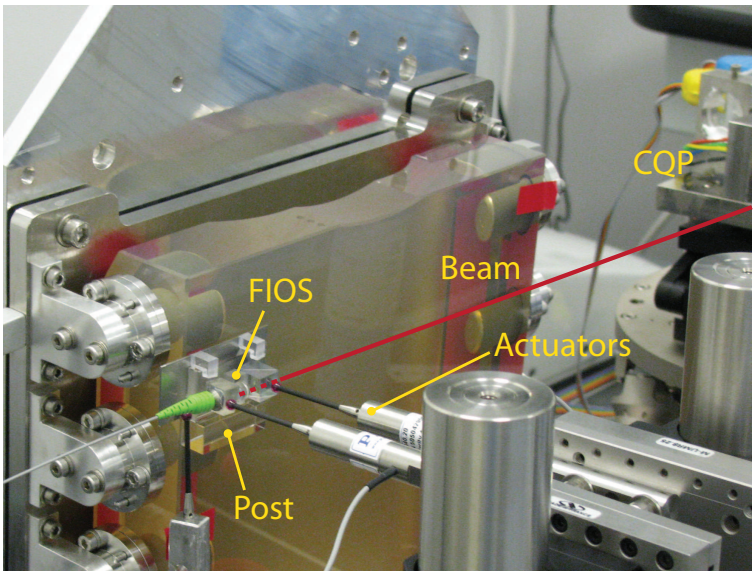

Figure 5.4: *Annotated picture of the FIOS bonding procedure.*

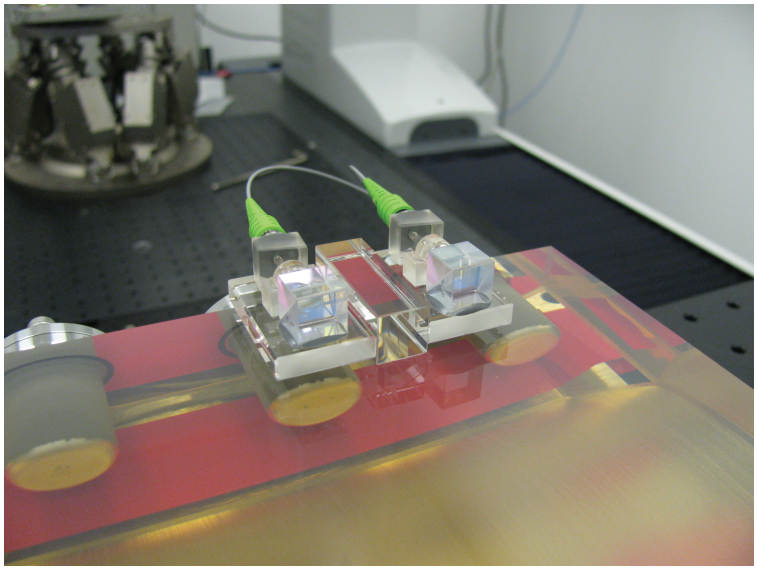

Figure 5.5: *Photograph of a bonded FIOS pair on the flight model OBI.*

With the first FIOS bonded in place and cured, the bench can be rotated through 180° and the second FIOS can be bonded in place. A completed FIOS pair is shown in Figure 5.5.

The in-plane alignment of the beams from the FIOS is largely dictated by the control over the lens during precision alignment and the orientation of the central mounting post which is bonded using a template. This is a non critical degree of freedom and is corrected by components further down the optical chain (BS1 for example).

5.1.2 Template bonding

Over half of the components on the OBI were bonded using templates of the type introduced in Chapter 4. While it would have been possible to bond all the template components with a single template, the decision was made to separate it out into 5 separate templates (originally 6, as indicated in Figure 5.2, but stages 7 and 11 were later amalgamated into a single template). The reasoning behind the use of multiple templates was twofold. Firstly, by use of the optimisation process described in Chapter 4, it allows extra control over the template components to avoid a potential build up of errors through the optical layout. Secondly, the more components bonded in a single step the longer the time required, increasing the risk of particles contaminating the cleaned bonding surface which could potentially lead to a failed bond.

5.1.3 Alignment to the test masses

The centring of the beams on the test masses is the most critical alignment on the OBI. The z centring is governed by the FIOS alignment (which must be parallel to the x-y plane throughout), and the y centring by the position of BS1 and BS3 for test mass 1 and test mass 2 respectively.

Within the core assembly of LISA Pathfinder, there are multiple reference

frames, most notably the OBF (the reference frame of the OBI) and the two frames of the test masses IAF1 and IAF2. Importantly, the OBF frame defines the master reference. That is, during integration of the spacecraft the test masses will be positioned with respect to the interferometer as opposed to vice-versa. This means that the two test masses have an *exact* theoretical position with respect to the OBI (front face centred on the x-axis, at the beam height and at $\pm 165\,\mathrm{mm}$ in x). The CQP can then be placed on this theoretical beam to act as the target for the alignment.

In reality, there is a small change. The two 'windows' depicted in the optical layouts are the optical windows which allow the beam to propagate into the housings containing the test masses. These windows were not available during the construction of the OBI and so their effects on the beam had to be compensated. To maximise accuracy, the actual flight windows were profiled by the manufacturer and the nominal optical model was adjusted to use the properties of the real windows (as opposed to the nominal windows). With no windows in place, the alignment can be (geometrically) compensated by moving the test masses forward by $\sim 2.3\,\mathrm{mm}$. This defines a slightly altered position to which to align the CQP.

For alignment of the beam to test mass 1, everything preceding BS1 in the optical chain was fixed requiring only the CQP to be positioned to the theoretical location. For alignment to test mass 2 however, the beam needs to be reflected from a dummy test mass 1. This requires that the dummy test mass 1 be aligned normal to the OBI, since any angular deviation in this mirror will couple as a positional error in the beam aligned to test mass 2. The nominal optical distance between the two test masses is $\sim 364\,\mathrm{mm}$, resulting in a $7\,\mu\mathrm{m}$ shift of the beam at test mass 2 for a misalignment of the dummy test mass 1 of just $10\,\mu\mathrm{rad}$. Compared to the test mass centring requirement of $\pm 25\,\mu\mathrm{m}$

this places tight requirements on the alignment of dummy test mass 1.

In practice, the way this was achieved was by carefully measuring the positions of the components and beams as the OBI was constructed. Using this data, an 'as-built' optical model was created which resembles the actual interferometer as closely as possible. This model can predict where the beam reflected from M1 should be for a well aligned test mass 1, providing a target location for the CQP to be positioned to align the dummy test mass 1; this is shown schematically in Figure 5.6. This same method was used to align the dummy test mass mirror for the bonding of M1 itself; see Section 5.1.5.

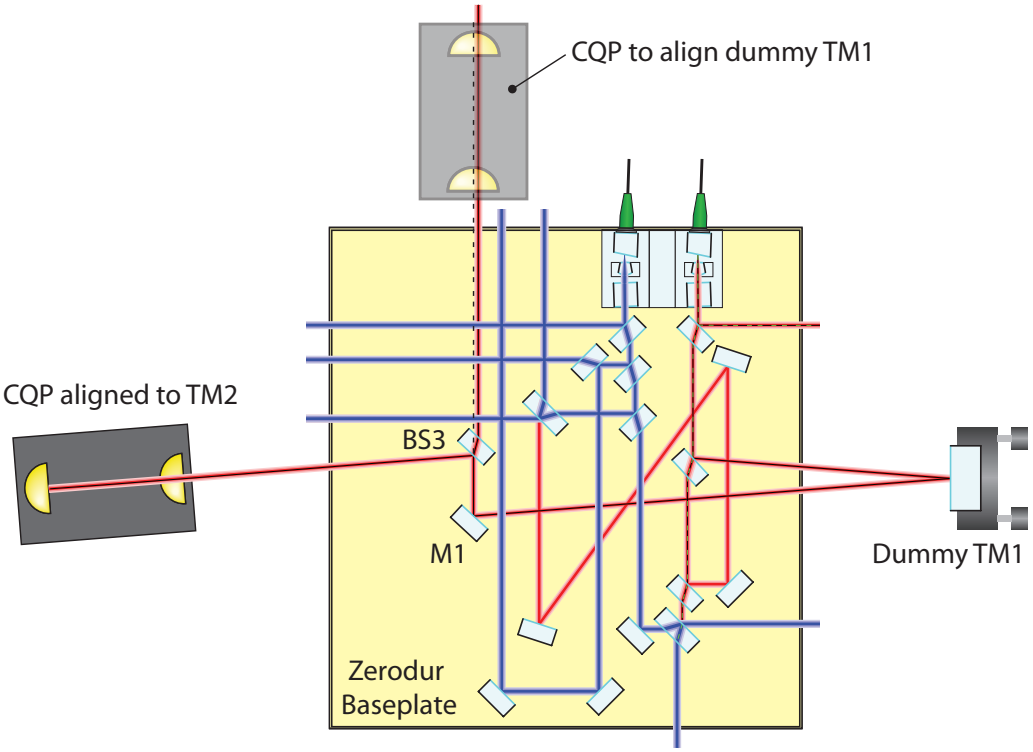

Figure 5.6: *Schematic showing the bonding of BS3, aligning the beam onto test mass 2.*

5.1.4 Beam combiners

The alignments of the beam combiners for the four interferometers are also precision bonding steps. To aid with phase measurement, we wish to maximise interferometric contrast at the photodiodes. This, however, is a relatively weak function of the overlap and tilt between the two combined beams. Of equal interest is the differential wavefront sensing signal. As discussed in Chapter 2, the DWS signal will be used for attitude control of the test masses by the DFACS system, however underlying the DFACS algorithm is an assumption that the DWS signal is linear with test mass angle. This is not generally true, but for the FIOS beam size of $\omega_0 = 650\,\mu$m is a good approximation for wavefront tilts of less than $\sim 400\,\mu$rad (the linear range can be estimated by calculating the angle subtended by $\lambda/2$ over the beam diameter). To allow DFACS as much range as possible, the nominal DWS signal (*i.e.* for nominally aligned test masses) should be as close to zero as possible, requiring that the beam combiners be positioned to combine the two beams ideally to within a few 10's of μrad of each other. Although use of the DWS signals are only required for the X1 and X12 interferometers, in practice all four interferometers are aligned this way. The DWS readout at the reference and frequency noise interferometers, while not essential for the science performance, is useful for system verification and to ensure that the interferometer and phasemeter are performing normally and that alignment has been maintained through launch.

For the bonding of BS10, the X12 combiner, both of the dummy test mass mirrors were required. This was achieved in much the same way as described for the alignment of the dummy test mass 1 for the alignment of BS3. For test mass 2 the as-built optical model was used to generate the predicted beam vectors for the nominally aligned test mass mirrors, and the CQP used to align the mirrors to this. For test mass 1 however, an easier approach was possible.

Since BS8, the X1 combiner was in place, it was possible to measure the DWS bias value at the X1 interferometer for an aligned test mass mirror. With this the test mass mirror could be aligned using a single quadrant photodiode at one port of BS8, adjusting the mirror to get the expected DWS value.

5.1.5 Path length matching

There are three components on the OBI that are precision adjustable to facilitate path length matching between the reference, X1 and X12 interferometers; these are M14, M1 and M8 respectively. As outlined in Chapter 2, matching the relative path length differences between the reference and measurement interferometers is desirable to minimise the coupling of laser frequency noise to displacement noise, and a requirement was placed on the OBI that the path length mismatches should be less than 1 mm [35].

The path length matching is achieved using the as-built optical model. With the model, the desired position of a component can be optimised to provide the required path length matching, taking into account the actual positions and optical thicknesses of all the preceding components, including the optical windows as described in Section 5.1.3 and the position of the test masses (the test masses are aligned to the optical bench, therefore their exact location with respect to the optical bench is known). Using this optimised position, a theoretical reflected beam can be established to which the CQP can be aligned, providing a target for bonding the component. In this way, path length errors built in with the initial components can be compensated for in each interferometer. Note that no such requirement is necessary for the frequency noise interferometer. It has a deliberate path length mismatch (of order 0.3 m) compared to the reference interferometer and the main requirement is that

this mismatch is sufficiently large to provide a sensitive measure of frequency noise. The precision of the mismatch is not important (although its value is still known to high accuracy from the as-built model).

5.1.6 Photodiodes

In total there are eight quadrant photodiodes detecting the light from both output ports of each of the four interferometers, and two single element photodiodes to provide error signals for the intensity noise servos. The photodiodes were designed and constructed by the University of Birmingham, and integrated onto the OBI by University of Birmingham staff on-site in Glasgow. The photodiodes are made from Indium Gallium Arsenide (InGaAs) due to its superior responsivity at near infrared wavelengths compared to comparable Silicon devices. The active area is 5 mm in diameter with 50 μm gaps between the quadrants to minimise fluctuations in phase read-out due to beam jitter.

Figure 5.7 shows the OBI after the completion of all bonding steps but prior to the integration of the photodiodes and Figure 5.8 shows the completed OBI ready for transport.

5.2 Accuracy achieved

As discussed in Chapter 2 and specified in [35] and [48], there are a significant number of key requirements that the OBI must fulfil in order to ensure the performance of LISA Pathfinder.

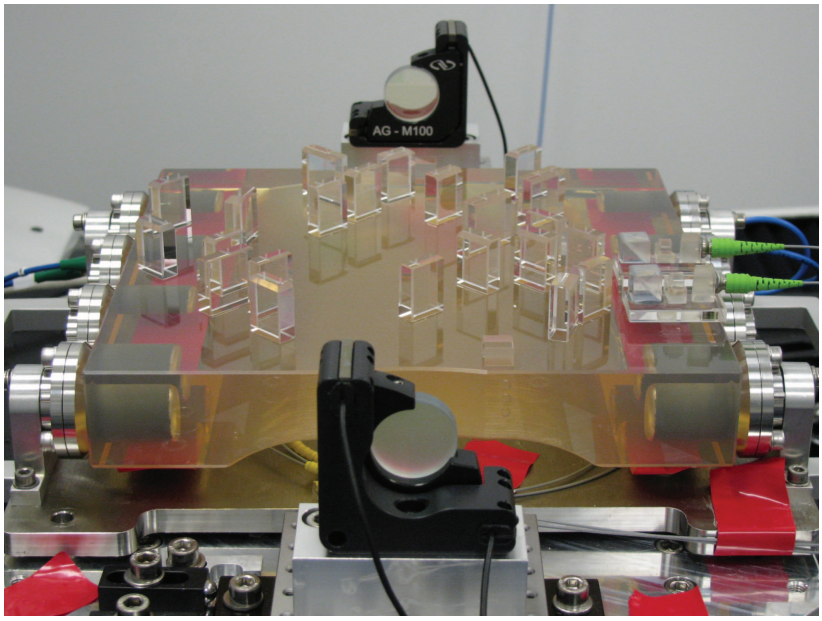

Figure 5.7: *Photograph of the OBI after the completion of all 17 bonding steps, ready for integration of the photodiodes.*

5.2.1 Test mass alignment

One of the most crucial requirements is that the beams incident on the test masses are centred to the nominal position to within $\pm 25\,\mu$m. The out of plane (z) centring was defined by the alignment of the FIOS and the manufacturing tolerances of the components, and the in-plane (y) centring by the bonding of BS1 and BS3 for TM1 and TM2 respectively.

The alignment values for the flight model and the flight spare are detailed in Table 5.1, as deviations from the nominal reflection point. These values were measured using the CQP, compensating for the optical window numerically as described in Section 5.1.3. For test mass 1, the measurement is dominated by the measurement errors associated with the CQP, of the order $\pm 4\,\mu$m. For test mass 2 there is an additional error in the angular positioning of the dummy test mass 1 which couples to a displacement error in the alignment at test mass

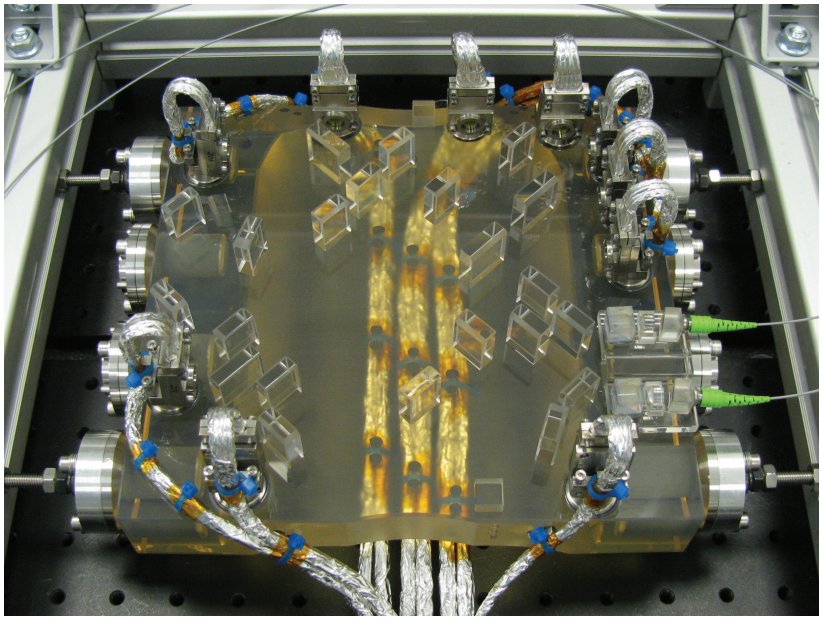

Figure 5.8: *Photograph of the completed OBI, ready for integration into the shipping container.*

1; this will contribute an additional $\sim 5\,\mu$m uncertainty.

Table 5.1: *Alignment of the beams to the test masses for the flight model (OB serial number 3) and flight spare (OB serial number 2) OBIs.*

	Flight Model (OB3)		Flight Spare (OB2)	
	y (μm)	z (μm)	y (μm)	z (μm)
TM1	-6	-15	-15	-6
TM2	-16	-7	0	-5

In practice, since the deviations from the nominal test mass reflection points are known they can be compensated for during spacecraft integration. By shifting the midline of the two test masses to the midpoint of the as-measured reflection points the deviations from nominal can be further reduced.

5.2.2 Interferometric performance

As described in Section 5.1.4, the four interferometer read-outs require to be well aligned to ensure high contrast ($> 80\,\%$) and a small differential wavefront signal (beam co-alignment less than a few 10's of μrad). The accuracies achieved on the flight model and flight spare are detailed in Table 5.2. The 'overlap' column gives the distance between the two beam centres at the photodiodes, 'DWS' is the in-plane and out-of-plane differential wavefront signals in degrees of phase difference (a full explanation of DWS, how it is calculated and how these values were measured can be found in Chapter 6) and 'Beam Angle' is the angle between the interfering beams as inferred from the DWS values (and confirmed with measurements of the beams using the CQP). Note that since the flight spare has not yet been fitted with photodiodes, the results presented were measured with different photodiodes and at a different position (off the bench due to access restrictions). Further, since this off-bench position would not yield representative beam separations at the intended QPD locations, these were calculated from CQP measurements and using the as-built model. While not adding a significant error, these values could change slightly once flight photodiodes have been integrated.

5.2.3 Path length matching

To assess the accuracy of path length matching, two techniques were employed. The first involved applying a frequency modulation to the laser. A sinusoidal signal was applied to a piezo transducer in the laser, resulting in a modulation of the laser frequency by $\pm\,100\,\mathrm{MHz}$ at a rate of $20\,\mathrm{Hz}$. By subtracting the reference phase from the phase of the frequency noise, X1 and X12 interferometers we can gain a measure of the relative frequency noise rejection between

Table 5.2: *Interferometric performance of the flight model (FM) and flight spare (FS) OBIs. DWS is the differential wavefront sensing signal, in degrees of phase difference and Beam Angle is the angle between the interfering beams. 'In' and 'Out' represent the in-plane and out-of-plane components of these measurements.*

Bench	Interferometer	Contrast	Overlap	DWS		Beam Angle	
				In	Out	In	Out
FM (OB3)	Reference	95 %	8 μm	$-2°$	$-4°$	8 μrad	16 μrad
	Frequency	90 %	2 μm	$-5°$	$-5°$	20 μrad	20 μrad
	X1	95 %	5 μm	$5°$	$-2°$	20 μrad	8 μrad
	X12	92 %	5 μm	$-18°$	$6°$	70 μrad	24 μrad
FS (OB2)	Reference	95 %	7 μm	$2°$	$4°$	8 μrad	16 μrad
	Frequency	89 %	8 μm	$3°$	$5°$	12 μrad	20 μrad
	X1	94 %	11 μm	$6°$	$-5°$	24 μrad	20 μrad
	X12	91 %	15 μm	$8°$	$-5°$	32 μrad	20 μrad

the interferometers. Since the reference and frequency noise interferometers have a deliberately large relative path length mismatch, the modulation will couple strongly as an apparent large displacement peak at 20 Hz whereas the frequency modulation should be largely rejected for well matched X1 and X12 interferometers. From Equation 2.1, frequency noise coupling is directly proportional to path length difference, and thus the ratio of the amplitudes of the displacement noise signals is the same as the ratio of path length differences. Since the path length mismatch in the frequency noise interferometer is large compared to the expected mismatch in the X1 and X12 interferometers, we only require to know the frequency noise path difference to a few mm to infer the other path differences to a potential accuracy of less than 100 μm.

Only the flight model was measured with this technique. The measurement was performed in air, with dummy test mass mirrors aligned to within $\pm 2\,\mu$m of their nominal x position using the CMM and with the EM model optical windows in place. The plot of the frequency noise rejection between the interferometers is shown in Figure 5.9. From the plot, it can be seen that there is just under 3 orders of magnitude of frequency noise suppression between the frequency interferometer and X1 and X12. For the flight model, the path length mismatch between the frequency noise and reference interferometers is 382.18 mm from the as-built model, giving a measured upper limit for the path length mismatch between the X1 and X12 and the reference interferometers of $\sim 400\,\mu$m, below the requirement of 1 mm.

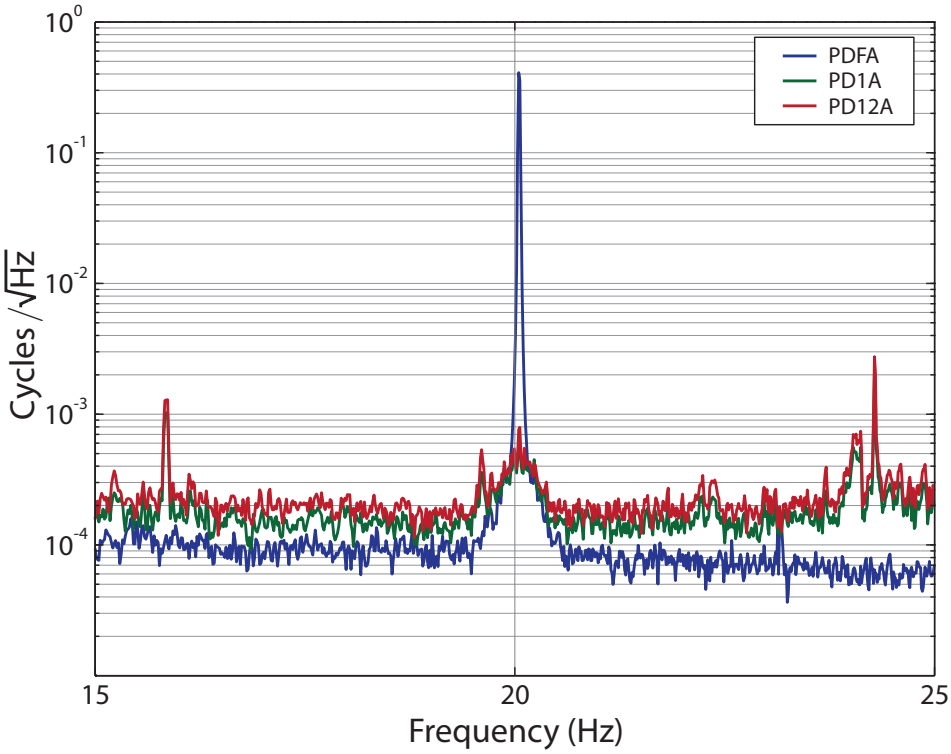

Figure 5.9: *Plot showing the relative frequency noise suppression between the frequency noise, X1 and X12 interferometers for the flight model OBI.*

It should be noted that this measurement is almost certainly noise limited, probably due to a number of factors including the ambient environment and the coupling of intensity noise into the measurement, which would not be rejected in the same way as frequency noise.

The second method used to gauge the accuracy of path length matching was the as-built Optocad model. Since the model is based around CMM measurements of both the physical components and the beams (using the CQP) it is a very accurate representation of the optical bench. Looking at the numerical outputs from the completed model, it suggests that the mismatch in path length between the reference and both the X1 and X12 interferometers, for the both flight model and the flight spare, is around 10 μm. This is an extremely small path length difference and one that is difficult to confirm by other means. Assigning an error to the Optocad prediction is also difficult due to the complicated build up of errors from successive CMM and CQP measurements. A somewhat simplified error analysis of CMM tolerances suggests that the figure should be correct to within approximately 40 μm however.

Chapter 6

DWS Calibration of the OBI

The concept of differential wavefront sensing (DWS) and its importance in LISA Pathfinder was briefly introduced in Chapter 2 and again in Chapter 5. This chapter will describe the DWS technique in more detail and go on to describe the DWS calibration process for the flight model OBI (OB3) and the results obtained.

6.1 Differential wavefront sensing

Differential wavefront sensing is a method for determining the relative tilt of two interfering wavefronts using only a quadrant photodiode. If the two beams are centred on the diode, and there is a relative tilt between the two wavefronts, then there will be a difference between the measured phases of the interference signal across the diode. This is illustrated in Figure 6.1, which simplifies the example to two dimensions using a two segment photodiode. On the top of the diode, the red beam is leading the blue, tilted, beam. This produces a

positive phase on that segment while on the bottom the red beam trails the blue beam producing a phase of the same magnitude, but negative in sign.

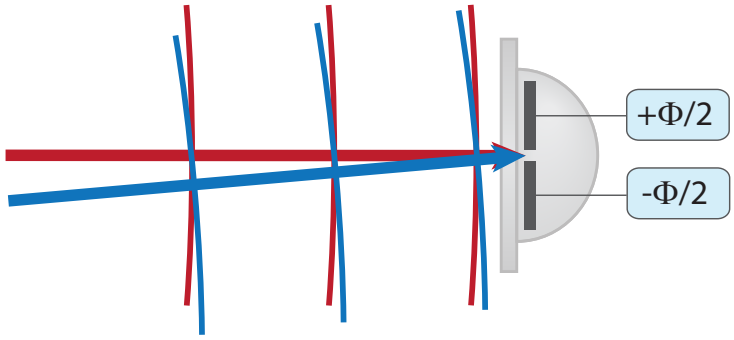

Figure 6.1: *Diagram illustrating the principle behind differential wavefront sensing.*

Since we can resolve Φ to small fractions of a wavelength, it is a very sensitive read-out of the relative wavefront tilts, and therefore of the angular alignment of the two beams. For LISA Pathfinder, the DWS signal is used to read-out the angular positions of the test masses. These angular signals will be used by the DFACS as the error signal for attitude control over the test masses in the science mode (the drift mode discussed in Chapter 2). Key to this is the assumption that the DWS signal is linear with changing beam angle (and thus changing test mass angle), while not quite true it is a good approximation for beam angles of less than 400 μrad for beams of the size used on the OBI. To ensure accurate control over the test masses, it is crucial for DFACS that this system is calibrated end-to-end, and that the linear approximation is tested over the measurement range. This requires that the calibration factors (called *k-coefficients*) between test mass angle and DWS readout are known for both test masses at all possible measurement photodiodes. These numbers are dimensionless, expressed in terms of degrees of DWS per degree of test mass rotation.

In total there are 12 k-coefficients to fully describe the system: two coefficients to describe the ϕ and η angles of test mass 1 at the X1 interferometer, another two to describe the orientation of test mass 1 at the X12 interferometer and then a further two for test mass 2 at X12 to total six. However each interferometer is read out twice for redundancy (each has two photodiodes labelled 'A' and 'B') so we define these coefficients at both photodiodes for a total of 12 coefficients. These can be described by

$$k^{\alpha}_{x,y} = \frac{\mathrm{DWS}^{\alpha}_{\mathrm{y}}}{\zeta^{\alpha}_{x}} \tag{6.1}$$

where DWS is the differential wavefront signal at photodiode y, ζ is the angle of test mass x and α is the orientation (*i.e.* ϕ or η). So, the coefficient describing the in-plane coupling between test mass 1 and the 'B' photodiode of the X12 interferometer is $k^{\phi}_{1,12\mathrm{B}}$ for example.

For a quadrant photodiode with quadrants labelled A-D as shown in Figure 6.2, the two DWS signals can be computed from the individual complex amplitudes, Φ, as follows

$$\mathrm{DWS}_{\phi} = \langle \left[\frac{\Phi_{\mathrm{A}} + \Phi_{\mathrm{C}}}{\Phi_{\mathrm{B}} + \Phi_{\mathrm{D}}} \right] \rangle \tag{6.2}$$

$$\mathrm{DWS}_{\eta} = \langle \left[\frac{\Phi_{\mathrm{A}} + \Phi_{\mathrm{B}}}{\Phi_{\mathrm{C}} + \Phi_{\mathrm{D}}} \right] \rangle \tag{6.3}$$

6.2 Calibration procedure

In order to calibrate the DWS signal, we need to be able to measure independently the angle of the dummy test mass mirrors with respect to the optical

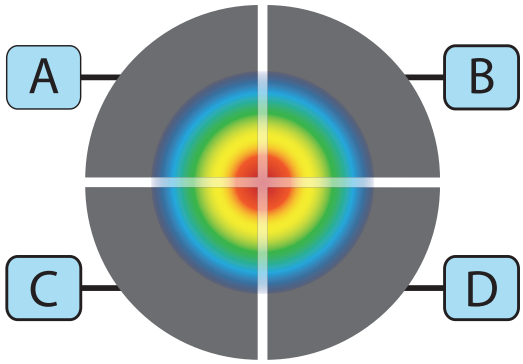

Figure 6.2: *Diagram showing the labelling convention for the quadrants on a QPD, looking at the active face.*

bench. To simply determine the slope of the relation between test mass angle and DWS, it is possible to do this with a well calibrated piezo controlled mirror. However, this method would make determining the operating point difficult and would also require good alignment of the pivot point to the OBI to avoid piston effects. DFACS needs to know where the operating point is, *i.e.* for what values of DWS signals are the test masses aligned normal to the optical bench. Nominally this would of course be zero, but for a real system there will be imperfections in the optical alignment resulting in a non-zero DWS signal for orthogonally aligned test masses. By performing an absolute calibration, and relating the angle of the dummy test mass mirror to the optical bench reference frame we can additionally define a set of DWS bias values, to form the zero points for the DFACS control algorithm.

The chosen method was to use a very large mirror, mounted on top of a hexapod and to measure its position and angle directly with the CMM. A relatively large mirror is required to reduce the angular measurement uncertainty to acceptable levels. The mirror used was $\sim 120\,\mathrm{mm}$ in diameter which reduced the CMM angular measurement error to less than $20\,\mu\mathrm{rad}$, with the hexapod allowing actuation of the mirror at μrad level. Approximately, the angular

measurement accuracy of 20 μrad over the $\sim$ 300 μrad DWS range should be sufficient to estimate the k-coefficients to within a few percent.

In operation LISA Pathfinder will have optical windows between the OBI and the test masses. The presence of the optical windows (see Chapter 5), will have an effect on the DWS bias values (*i.e.* the DWS values that will be used by DFACS as the zero point for orienting the test masses) and k-coefficients. The effect comes both from the extra optical path length introduced by the windows and from the lack of parallelism of the windows. The windows are manufactured from a special glass, OHARA S-PHM52 [49], chosen for its very small $\frac{\mathrm{dn}}{\mathrm{dT}}$. This glass is extremely difficult to polish, however, and the result is that the windows are parallel to a few arc-seconds at best. This wedge angle introduces a static change in angle to the beam on transmission that is dependant on the magnitude of the wedge and on the rotation of the window. The engineering model windows available are comparable to the flight windows in thickness and refractive index, so can effectively replicate the path length effect of the flight windows. However the rotational orientation of the flight windows is unknown, therefore it is impossible to fully replicate the effect of the wedge angle with the EM windows. The wedge angle will have greatest effect on the DWS bias values (since it imparts a static, absolute, shift in beam angle) whereas it will have minimal effect on the scaling which has a relatively weak coupling to small shifts in beam angle. The path length effect will change the beam parameters at the photodiode. This should have minimal effect on the magnitude of a DWS value, but can effect the coupling of DWS to beam angle. In light of this, the DWS bias values were determined without optical windows (using the numerical correction for test mass x position), whereas the k-coefficients were measured with the EM windows in place.

So far we have described the determination of the DWS operating points and k-

coefficients. These are vital for science operation but are not the whole story. In the initial acquisition phase the test mass angles may be far outside the linear operation range of DWS, and possibly so far offset from their nominal position that a DWS signal may not be detectable. In this situation the DC beam position on the photodiodes will be used for an initial, coarse, alignment. It is therefore sensible to test this alignment by characterising the DC beam position read-out as a function of test mass angle over a large range. The full calibration procedure then consists of four distinct parts:

1. Measurement of the DWS bias values for nominally aligned test masses - without optical windows.

2. Measurement of the 12 k-coefficients, varying the dummy test masses by small amounts out to around $\pm\,100\,\mu$rad ($\pm\,6$ millidegrees) - with optical windows.

3. Check the limit of DWS linearity by varying the dummy test masses by larger increments out to around $\pm\,700\,\mu$rad ($\sim\pm\,40$ millidegrees) - with optical windows.

4. Test of DC alignment, sweeping the dummy test mass mirrors until light is no longer visible on the photodiodes - with optical windows.

The set-up used for the measurements is illustrated in Figure 6.3, with the optical windows located in tip-tilt mounts to enable them to be aligned with a 2.5° inclination, as they will be in the spacecraft. The large mirror is mounted on a hexapod, with the other test mass being replaced by one of the small dummy test mass mirrors where necessary.

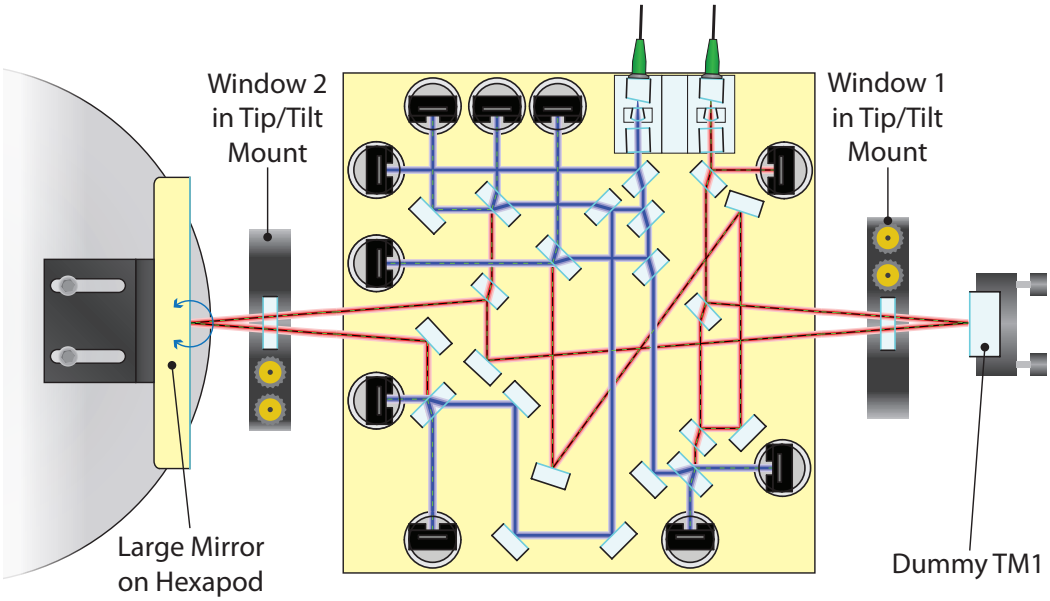

Figure 6.3: *Diagram showing the set-up for the DWS calibration of the OBI.*

6.3 Results

The DWS calibration took place in-air, with the OBI located on the CMM bed to allow measurement of the mirrors and windows (which were placed in their nominal position) to take place.

6.3.1 DWS bias values

The DWS bias values, measured without windows in place, are shown in Table 6.1. The dominant source of uncertainty for measuring the values in the X1 and X12 interferometers will be the angular measurement error of placing the dummy test mass mirror normal to the OBI. Taking this to be $\sim \pm 30\,\mu$rad and taking the DWS to angle coupling factor to be around 5000 (a reasonable approximation, see Section 6.3.2) we can derive an uncertainty on the measured bias values of around $\pm 9°$ of phase difference. Note that, as discussed

in Chapter 5, the DWS values for the reference and frequency noise interferometers are also given. Since both of these interferometers are static (*i.e.* they have no moving components in either beam path) the DWS values should also be static. This means they are a useful check of the integrity and functionality of the OBI, especially to ensure that beam pointing from the FIOS has been maintained to a suitable level during launch and in the final operating environment of LISA Pathfinder on orbit. The dominant uncertainty in these values is likely to be beam deviation through air currents, which can effect a beam at the few μrad level, or around $1 - 2°$ of phase difference.

Table 6.1: *DWS bias values for DFACS alignment of the test masses.*

PD1A		PD1B		PD12A		PD12B	
ϕ	η	ϕ	η	ϕ	η	ϕ	η
5°	−2°	5°	−1°	−18°	6°	18°	6°
PDRA		PDRB		PDFA		PDFB	
ϕ	η	ϕ	η	ϕ	η	ϕ	η
−2°	−4°	2°	4°	−5°	−5°	5°	−6°

The derived uncertainty of $\pm 9°$ is large compared to the majority of values in the table. There is reason to believe, however, that the actual uncertainty on these measurements is significantly better than the rough value calculated above. This value is calculated based on the basic CMM measurement error of $\pm\,(1.5\,\mu\text{m} + 3\,\mu\text{m/m})$. The mirror is measured by taking probe hits at various points on its surface. In a worst case approach where the error is randomly distributed, the maximum angular error would then be the full magnitude of the CMM error, with signs in opposite directions, over the 120 mm baseline. This gives around 28 μrad. However, under certain circumstances it is suspected that much of this error is not randomly distributed, but has the same sign and

magnitude. This component will then cancel as a common mode error when calculating the angle. This is believed to be the case when making measurements of very flat surfaces where the probe always approaches normal to the surface, as was the case for measuring both the mirror and the OBI. Due to the proprietary nature of the CMM and its software, verification of this is difficult. Some confidence can be gained, however, by remeasuring the DWS bias values for the X1 and X12 interferometers. These results, shown in Table 6.2, were measured in an identical manner to the original values. The results show that the change in DWS values between the measurements was only a fraction of the error calculated above, suggesting that a significant component of the measurement error is not random.

Table 6.2: *Original and remeasured DWS bias values for the four interferometers of the Flight Model OBI.*

	PD1A		PD1B		PD12A		PD12B	
	ϕ	η	ϕ	η	ϕ	η	ϕ	η
Original	5°	−2°	5°	−1°	−18°	6°	18°	6°
Remeasured	6°	−6°	6°	−6°	−18°	7°	18°	8°
	PDRA		PDRB		PDFA		PDFB	
	ϕ	η	ϕ	η	ϕ	η	ϕ	η
Original	−2°	−4°	2°	4°	−5°	−5°	5°	−6°
Remeasured	−2°	−6°	2°	6°	−5°	−4°	5°	−5°

6.3.2 Determination of the k-coefficients

To measure the k-coefficients, the large mirror was initially situated at the location of test mass 1. The mirror was actuated, in steps of around 20 μrad

over $\pm 100\,\mu$rad ($\sim 6\,\mathrm{m}^\circ$), verified by CMM measurement, first in-plane (ϕ) and then out-of-plane (η). The smaller dummy test mass mirror was situated at the location of test mass 2, using the DWS bias values from Table 6.1 to align it to the nominal location. The DWS signals from all X1 and X12 photodiodes were recorded as the mirror was actuated. The two mirrors were then swapped, with test mass 1 in the nominal location and test mass 2 varied in the same manner, recording the X12 interferometer DWS values.

All DWS signals were found to be highly linear over the full measurement range. An example plot showing one data set, with a linear fit, is shown in Figure 6.4. This is for the ϕ motion of test mass 1 at photodiode PD1B ($k^{\phi}_{1,1\mathrm{B}}$). The fit was a least squares regression and the R^2 statistic value was greater than 0.99, as it was for all the fits.

The full results of the DWS calibration are detailed in Table 6.3. Additionally, as part of the LISA Pathfinder project, simulations of the DWS performance have been carried out by Gudrun Wanner from the Albert Einstein Institute at the University of Hannover. The simulations are detailed in [50], and a comparison of the simulated values and the actual values is given in Table 6.4. Since the simulation was ideal and symmetric, only 3 k-coefficients are modelled. The differences in sign are due to the use of a different handed coordinate system in the simulation.

Agreement between the simulations and the measured values is within 10 %. Given the ideal nature of the simulation (in terms of both geometric alignment and beam properties) this is a good agreement.

Properly we expect an uncertainty, resulting from the CMM measurement error associated in measuring the mirror. Strictly, this would be error bars of $\pm 1.5\,\mathrm{m}^\circ$ on the $x-$axis of the points in Figure 6.4. As discussed in the

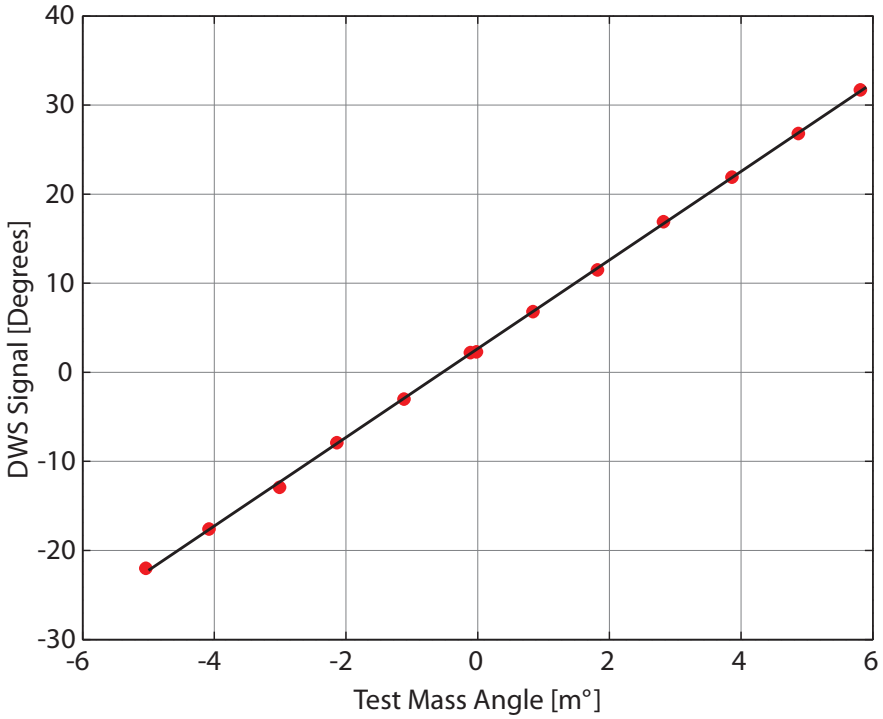

Figure 6.4: *Plot showing the measurement data and least squares fit for one of the k-coefficients.*

preceding section, however, there are indications that much of the CMM measurement error is common mode and cancels when measuring angles in this manner. If the measurement error in the CMM was randomly distributed (*i.e.* there was no common mode rejection), we would expect to see a large scatter of the points in Figure 6.4 around the $x-$axis. Since we see a very linear grouping of points - which is what we expect to see from simulation - we can conclude that there is a high probability that the suspected common mode error cancellation is taking place in the CMM for these situations.

Table 6.3: *Measured values of the k-coefficients for the OBI, in dimensionless units of degrees/degree.*

$k^{\phi}_{1,1A}$	$k^{\phi}_{1,1B}$	$k^{\phi}_{1,12A}$	$k^{\phi}_{1,12B}$	$k^{\phi}_{2,12A}$	$k^{\phi}_{2,12B}$
4928	4977	4578	−4570	−5171	5211
$k^{\eta}_{1,1A}$	$k^{\eta}_{1,1B}$	$k^{\eta}_{1,12A}$	$k^{\eta}_{1,12B}$	$k^{\eta}_{2,12A}$	$k^{\eta}_{2,12B}$
−4891	−4922	−4601	−4598	5220	5257

Table 6.4: *Comparison of the measured k-coefficients with simulated values from [50]*

Coefficient	Measured	Simulated
$k^{\phi}_{1,1B}$	4977	−4900
$k^{\phi}_{1,12B}$	−4570	4353
$k^{\phi}_{2,12B}$	5211	−5619

6.3.3 DWS linearity tests

The DWS values are expected to be linear with test mass angle for test mass angles of less than 150 μrad (*i.e.* beam angles of less than 300 μrad). Verification of this is important since applying the linear approximation outside of the actual linear range could lead to unexpected behaviour of DFACS. An identical procedure to that used to derive the k-coefficients was used, only this time actuating the mirror in steps of 175 μrad out to $\pm$ 700 μrad ($\sim 0.04^{\circ}$).

An example plot, again for the ϕ measurement of test mass 1 at photodiode PD1B is shown in Figure 6.5. The fit line in the figure is derived from the k-coefficient. From the figure it can be seen that the system is linear in the centre section out to at least 0.01° or 175 μrad of test mass rotation, confirming

that the DFACS approximation is valid. All 12 tests of the linearity produced similar results.

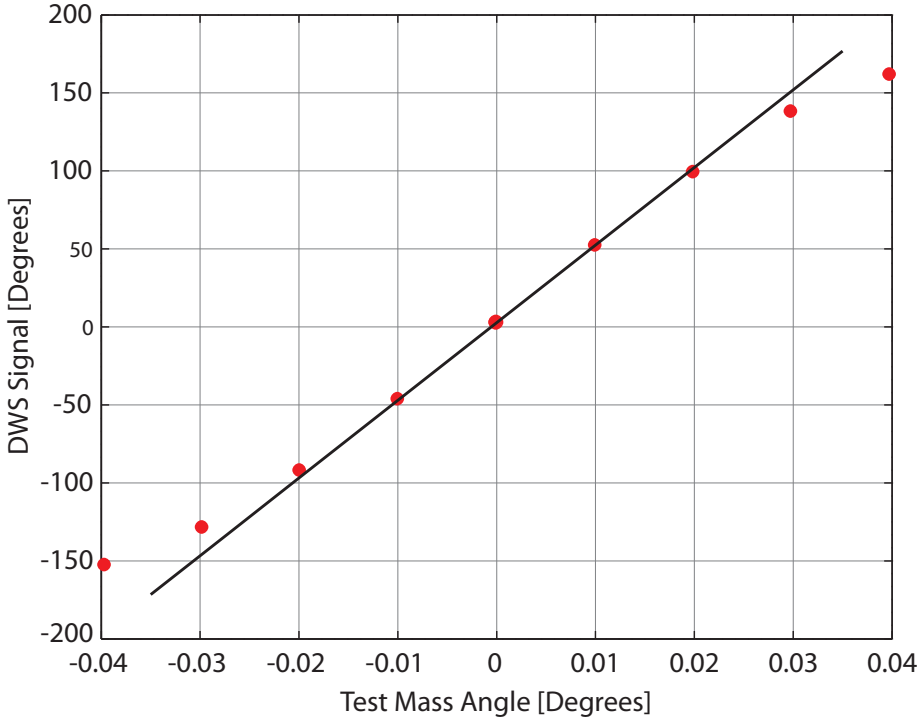

Figure 6.5: *Plot showing a check of the DWS linearity with test mass angle for test mass 1 at PDRB. The fit line is derived from the measured k-coefficient.*

6.3.4 DC alignment tests

The check of DC beam position was conducted in an identical manner to the previous two tests, this time varying the mirror by 0.05° increments out to $\sim \pm 0.5°$. The normalised DC beam position was recorded as the mirror was varied. This is a dimensionless number, normalised against the full power of the beam, calculated such that a position of 0 corresponds to a perfectly centred beam, with ± 1 being a beam entirely on one side of the diode. The results, also for the ϕ motion of test mass 1 at PD1B, are shown in Figure 6.6.

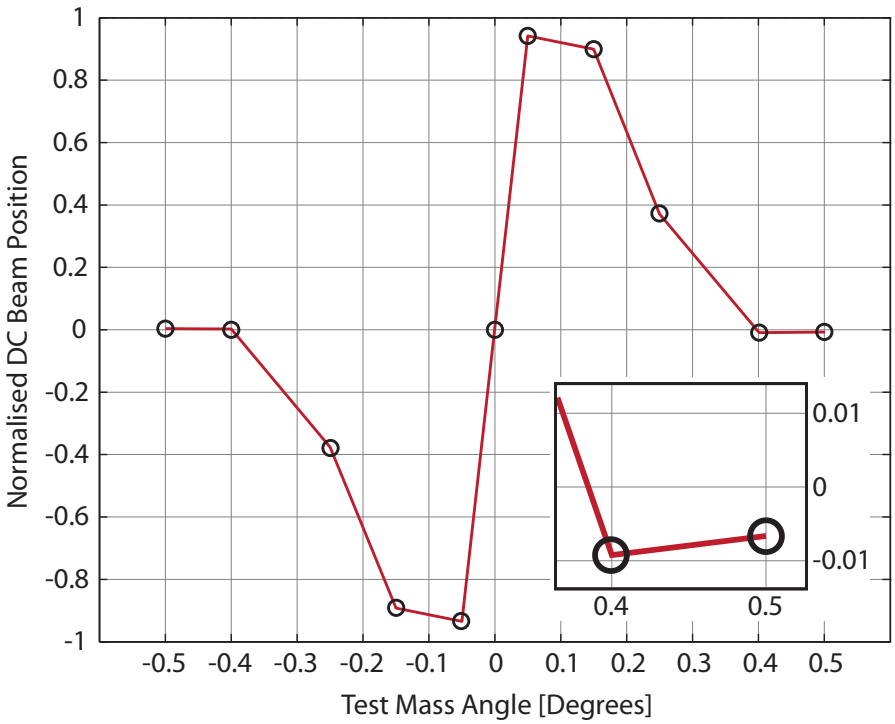

Figure 6.6: *Plot showing a test of the DC beam read-out for large test mass angles, the mode used for coarse alignment in LISA Pathfinder after initial release of the test masses. Inset is a blow-up of the region between* 0.4° *and* 0.5°*, highlighting sign change in the DC beam position. The dark level for the measurement is less than 0.001.*

The central region shows a clear linear relationship between beam angle and test mass position, this is the region for which all (or virtually all) of the light power is on the diode. Beyond this, some of the light power falls off the diode, creating the non-linear change in DC beam position for test mass angle. In the acquisition mode DFACS spiral scans the test mass, with the DC read-out of the lateral position of the beam on a photodiode as the error signal for the control system. One interesting point to arise from the test was that at very large test mass angles the DC signal does not rise monotonically as would be expected in a simple model but briefly decreases below zero before rising as

expected. The scaling of Figure 6.6 is too coarse for this to be visible as it is a small effect, but in the flat regions of the plot between $0.4° - 0.5°$, for example, the signal is measurably below zero, corresponding to a test mass angle of $-0.5°$ rather than the true angle of $+0.5°$. This is the region where the beam is only just missing the diode, so it is incident on the structure immediately surrounding the diode itself. This is a significant result, as the incorrect sign of signal could potentially confuse a simple control system and so is something which is of importance for DFACS during the acquisition phase. One likely explanation is that the beam is scattering from the case surrounding the diode and the diode bond wires onto the opposite side of the QPD, giving rise to the incorrect sign of DC signal.

Chapter 7

LISA optical bench development

With the successful completion of the LISA Pathfinder flight model interferometer, work can now begin on developing the alignment, construction and metrology techniques used to the level required for LISA. This chapter gives an overview of LISA and describes the interferometry principle in detail before looking at the specifics of progressing towards the LISA optical bench. Finally, it concludes with the current state of development of a prototype of the LISA OB being developed under contract from the European Space Agency.

7.1 The LISA mission

7.1.1 Mission description

LISA will have a solar orbit, at a distance of 1 AU from the sun and trailing approximately 20° behind earth (70 million km). The plane of the constellation will be inclined at 60° to the ecliptic, and will rotate through 360° in this plane

over one solar orbit. This orbit provides high dimensional stability of the inter-spacecraft distance in the measurement band without the need for additional thruster burns [51] and allows determination of the direction of some constant sources to within ~ 10 arcmin over the course of the solar orbit, depending on the signal to noise ratio [6].

The end points to which the inter-spacecraft distances are ultimately measured are the test masses. Like LISA Pathfinder, they are gold-platinum alloy cubes which are kept as close as possible to free-fall in the sensitive direction (*i.e.* they follow geodesics). Each spacecraft has two test masses, such that there are six in total, forming the ends of the three arms of the interferometer. The projected sensitivity curve for LISA is shown in Figure 7.1. At frequencies below ~ 3 mHz, the residual acceleration of the test masses is the main limiting noise source. Above 3 mHz the noise inherent to the metrology system is limiting and at frequencies above 30 mHz this metrology noise is combined with limitations from the arm length. This is because when the wavelength of an incoming gravitational wave nears an integer multiple of the arm length, sensitivity is reduced [52]. To reach the design strain sensitivity of $10^{-20}/\sqrt{\text{Hz}}$ in the mid band, the end-to-end precision of measuring the test mass separation must be around $10\,\text{pm}/\sqrt{\text{Hz}}$, and the residual acceleration noise of the test masses must be of order $3 \times 10^{-15}\,\text{m}\,\text{s}^{-2}/\sqrt{\text{Hz}}$ [52, 53].

7.1.2 LISA interferometry

The LISA science read-out is a combination of various interferometric measurements, which combine to measure the fluctuations in the separation of the two test masses at the end of each arm. Like LISA Pathfinder, the interferometers are located on an optical bench (OB). The large distance between the

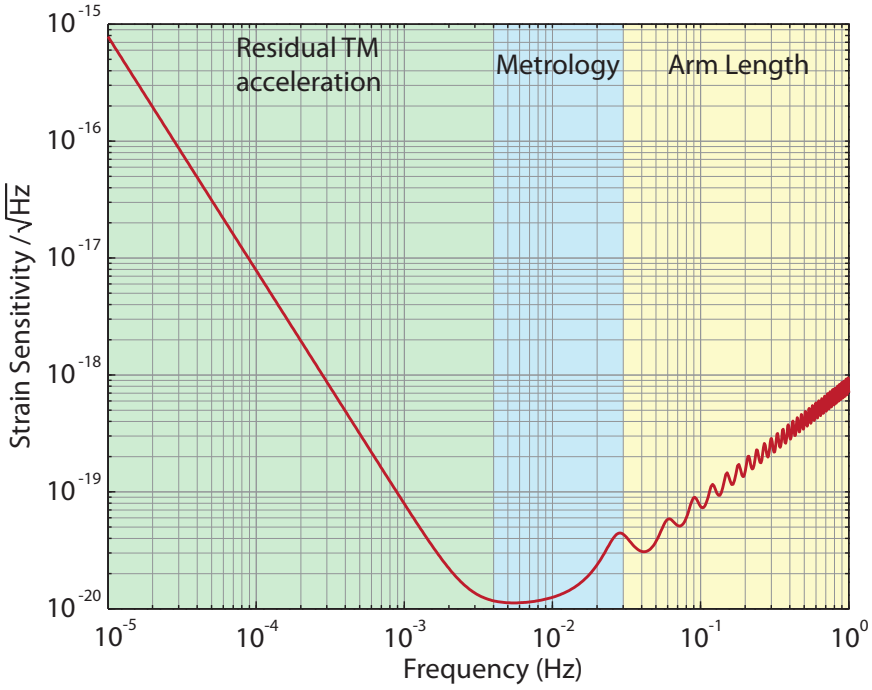

Figure 7.1: *Plot showing the LISA sensitivity curve, with the main limiting noise source indicated for each frequency band [52, 21].*

spacecraft necessitates a somewhat more complicated interferometric scheme to that found in ground based detectors. For a single LISA arm, light from the optical bench is sent through a $\sim 400\,\text{mm}$ diameter telescope towards the far spacecraft. Over the $5 \times 10^9\,\text{m}$ baseline, this beam will have expanded to several km in diameter and only around 100 pW of light will enter the telescope at the far spacecraft. The result of this is that the beam from the far spacecraft cannot easily be reflected back to the originating spacecraft like a traditional Michelson interferometer. Instead, the measurement is separated out into thee components; the distance between the two optical benches (*i.e.* the inter-spacecraft distance) and the distance between each optical bench and its local test mass. This is known as a *strap down* scheme [52, 54, 55].

The interferometry uses multiple heterodyne interferometers. On each OB,

there is light of three different frequencies: one from the local OB, one from the other OB in that spacecraft, and one from the far spacecraft. The two OBs on a single spacecraft are linked with a single mode optical fibre (called the 'backlink' fibre), and light from the main laser associated with each optical bench counter-propagates down this fibre providing each OB with the two local beams at different frequencies. One possible operational mode, which negates the need for absolute frequency references such as locking to iodine transition lines [56], is to phase lock the lasers together in a chain. The two local lasers on a space craft can be locked with a frequency offset of a few MHz. The two lasers at the ends of an arm can also be phase locked together, again with a frequency offset in the region of 10 MHz. Since this is repeated for all arms, all the lasers in the entire constellation are then phase locked together, referenced against an arbitrarily chosen master laser [52, 55].

The exact nature of the interferometry is best illustrated with a diagram, shown in Figure 7.2. If the three spacecraft are designated A, B and C, then a nomenclature $x_{i,j}$ can be defined where x is something we wish to describe *e.g.* an OB, or light of a particular frequency or a test mass, i is the spacecraft to which it is associated and $j \in \{1, 2\}$, since there are typically two of each item on a single spacecraft, one for each arm. Using this nomenclature, everything in the constellation can be uniquely identified. The isolation and control of the test masses is identical to that of LISA Pathfinder, as described in Chapter 2.

On spacecraft A, $\mathrm{OB}_{\mathrm{A},1}$ is aligned with $\mathrm{OB}_{\mathrm{B},2}$ on the far spacecraft. The two OBs at each end of an arm are subtly different. A polarisation multiplexing scheme is used to separate out the transmit and return beams at each OB with a polarising beam splitter (PBS), shown as a cube in the figure, providing the separation. A single half-wave plate on one bench creates the polarisation mismatch with the counter propagating beams between the spacecraft being

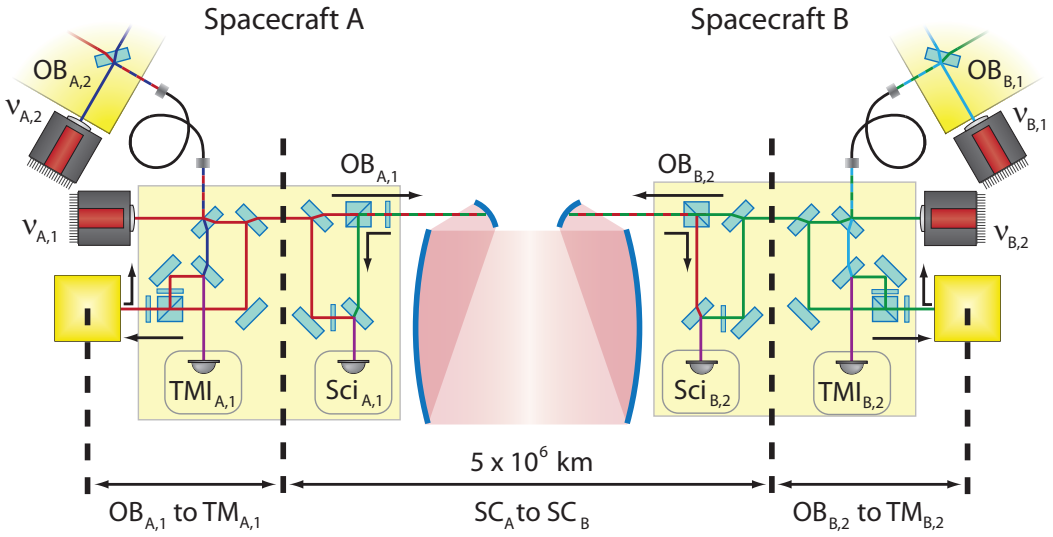

Figure 7.2: *Schematical representation of the interferometry in a single LISA arm.*

in orthogonal polarisation states. A polarisation steering system is also used for the test mass read-out. The input vertically polarised light is first completely reflected by a PBS towards the test mass, a quarter-wave plate between the PBS and the test mass first creates circularly polarised light (which reflects from the test mass at normal incidence) and then horizontally polarised light as it passes back through the quarter-wave plate towards the PBS. This light can then be transmitted through the PBS (separating it from the incident beam), with a final half-wave place rectifying it to vertical polarisation before the interference point.

On $\mathrm{OB}_{\mathrm{A},1}$, light from its primary laser at frequency $\nu_{\mathrm{A},1}$ is transmitted to the far spacecraft and interfered with a small portion of the return frequency $\nu_{\mathrm{B},2}$ on $\mathrm{OB}_{\mathrm{B},2}$. Similarly, on $\mathrm{OB}_{\mathrm{A},1}$ the received light at frequency $\nu_{\mathrm{B},2}$ is interfered with a small portion of the transmit beam $\nu_{\mathrm{A},1}$. The interference between $\nu_{\mathrm{A},1}$ and $\nu_{\mathrm{B},2}$ provides the signal $\mathrm{Sci}_{\mathrm{A},1}$ on spacecraft A, and a similar interference forms the signal $\mathrm{Sci}_{\mathrm{B},2}$ on spacecraft B. These two signals combine to provide

the read-out of the spacecraft separation (the *Science Interferometer*). The error signal for the offset phase locking of the two lasers is also derived from these signals. The primary beam is also used to probe the test mass, and is interfered with the swapped light from the other OB, $\nu_{A,2}$ providing the read-out of the test mass displacement relative to the optical bench at interferometer $TMI_{A,1}$ (the *Test Mass Interferometer*). In addition there is a *Reference Interferometer*, which is not shown in the figure for clarity. This is also an interference between the two local beams, *i.e.* between $\nu_{A,1}$ and $\nu_{A,2}$ on $OB_{A,1}$. It provides two things, firstly an error signal with which to phase lock the two local lasers and secondly the main phase reference for each optical bench which is required for the displacement measurements. Movement of, *e.g.* $TM_{A,1}$ will change the phase of the heterodyne signal at $TMI_{A,1}$. Just as in LISA Pathfinder, phase measurements of the signal with respect to that of the stable reference signal $REF_{A,1}$ creates an output signal proportional to the test mass movement.

7.2 LISA design challenges

A prototype version of the LISA optical bench is currently being developed with a contract funded from the ESA Core Technology program. This is a collaborative project involving the University of Glasgow, the Albert Einstein Institute at the University of Hannover, EADS Astrium GmbH and TNO in the Netherlands. The bench is intended to be as representative of a potential flight model optical bench as possible and is being designed and constructed in Glasgow, with subsequent testing at the Albert Einstein Institute. EADS Astrium GmbH are the prime contractor and TNO are producers of precision actuators for integration onto the optical bench.

The effort to develop the prototype LISA optical bench is largely built upon

the LISA mission formulation study, commissioned by ESA and completed by EADS Astrium GmbH and EADS Astrium Ltd. The study produced a detailed reference design for LISA, taking the science goal of a peak strain sensitivity of $10^{-20}/\sqrt{\text{Hz}}$ in the mHz region, and deriving a complete set of requirements which must be met to achieve this goal. To be truly representative, the prototype optical bench must conform to the system level requirements derived in the mission formulation study (*i.e.* telescope interfaces etc.), in addition to fulfilling the basic measurement functions and performance required from the measurement principle. A complete discussion of the system design is beyond the scope of this thesis. The discussion which follows is limited to matters specifically concerning the optical bench and is largely derived from [57]. An overview of the complete reference design and top level requirements which resulted from the formulation study can be found in [58].

For the purpose of the following discussion, we will concentrate on a single OB and require a simplified nomenclature compared to that defined in Section 7.1. In this simplified nomenclature the primary beam, that of the laser associated with the OB and the beam transmitted to the far spacecraft is the *Tx* beam. The second beam, the other local beam swapped down the backlink fibre with the other OB of the spacecraft is the *local oscillator* and the third beam, received from the far spacecraft is the *Rx* beam.

7.2.1 Requirements implicit from the measurement principle

Based on the measurement principle outlined above, we can establish a fundamental set of requirements and functions which the prototype optical bench must meet.

- The optical bench needs to provide three distinct phase measurements; a reference phase, a read-out of the test mass position and a measurement of the inter-spacecraft displacement. These are the reference, test mass and science interferometers discussed previously.
- There must be an on-bench optical path between the two fibre injectors, to facilitate the swapping of a fraction of the Tx beam to serve as the local oscillator of the other optical bench, and equivalently deliver the local oscillator beam to this optical bench (the 'backlink' fibre).
- Polarisation optics should be used to allow separation of the beams probing the test mass, and the transmitted and received beams to and from the telescope.

7.2.2 Requirements derived from the formulation study

We can further specify a set of requirements and functions based on the conclusions of the mission formulation study. At the system level the optical bench must be able to interface with the other components of the spacecraft, especially the telescope and the test mass, for which there are stringent optical alignment criteria.

Interface to the spacecraft

The reference design for the LISA payload has the optical bench mounted parallel to the telescope primary mirror, with the inertial sensor housed on the opposite size of the OB to the telescope. This requires that beams must be directed out-of-plane from the OB surface, with the telescope entrance being above the optical bench and the test mass underneath. The test mass reference

location is directly in the centre of the OB, with the telescope entrance approximately 50 mm from the centre. Mirrors, precision manufactured to provide a 45° angle and catalysis bonded to the OB, will be used to provide the out of plane pointing. A CAD rendering showing the relative positioning of the three parts can be seen in Figure 7.3.

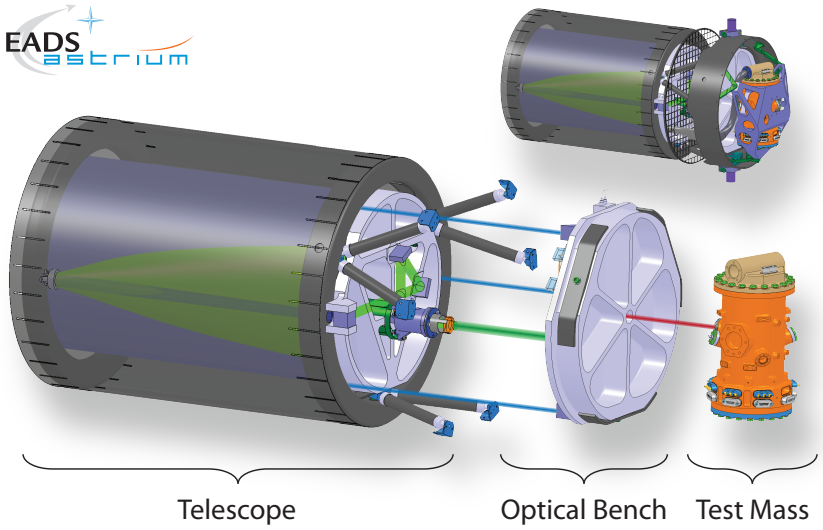

Figure 7.3: *CAD rendering showing the concept LISA architecture, with the telescope, optical bench and inertial reference sensor (Courtesy D. Weise, EADS Astrium GmbH).*

In the orientation depicted in Figure 7.3, the diameter of the optical bench is one of the key components driving the height of the spacecraft. Since an increase in spacecraft height also implies an increase in mission cost, the optical bench must consume as small a footprint as possible. The reference design from the formulation study was of the order 500 mm in diameter so any new design should aim to keep to a similar size as far as is practical. For similar reasons, the telescope cannot have an arbitrarily large magnification, the desired output beam width of 400 mm coupled with the magnification of 80 results in the telescope requiring an input beam diameter of around 5 mm. This is a large diameter and performing all the functions on the optical bench with this

beam size is impractical. Therefore, a beam expander is required to magnify the beam to the telescope to the required size. The Rx beam will also be similarly sized, so the portion of the Tx beam interfered with it at the science interferometer should also be of the larger size to maximise the efficiency. All other beams should be of a smaller size to minimise the size of the optical components, and hence the overall size of the OB. A Gaussian beam of diameter 5 mm still has significant optical power at distances outwith this beam radius. For the 1 W Tx beam, around 80 mW of optical power is outside this diameter. However, the telescope itself has an internal aperture of 5.1 mm. This presents a risk of scattering significant amounts of the Tx beam back onto the optical bench with the incoming low power Rx beam. This has the potential to add phase noise at the science interferometer that could swamp the science signal. To minimise the possibility of straylight scattering back into the Rx path, a clipping aperture will be located in the Tx path to the telescope. This will clip the Tx beam at 5 mm $\pm$ 20 μm, which is slightly smaller than the aperture of the telescope. Enough space must be reserved for this clipping aperture and its associated baffles to absorb the clipped beam power.

To aid in alignment and to monitor the length fluctuations between the primary and secondary mirrors in the telescope, an 'optical truss' will be used. This requires three local oscillator beams to be launched upwards from the OB towards the far end of the telescope. Here they will be interfered with a small sample of the transmitted beam (captured through pinholes at the peripheries of the telescope exit). These optical truss beams must be launched from three points, separated by 120° at a radius of 225 mm from the centre of the OB.

Interface to the constellation

Although the LISA orbit has been carefully chosen for stability, there are still periodic changes in the constellation over the course of an orbit. These periodic changes require a variable angle between the Tx and Rx beam to ensure that the Tx beam stays centred on the far spacecraft. To compensate for these angle changes, the Tx beam requires to be actuated at the level of around $\pm 6\,\mu$rad. Since changes in the telescope would also impact on the Rx beam, this actuation must be implemented on the optical bench level before the two beams are multiplexed at a polarising beam splitter. On the optical bench, the magnification of the telescope ($\times 80$) increases the required angular variation to $\pm 480\,\mu$rad. The required mechanism must be highly stable both in pointing and pathlength. Rising to the challenge, TNO have successfully designed a mechanism which demonstrates the required performance, called the point ahead angle mechanism (PAAM). A picture of a prototype PAAM can be seen in Figure 7.4.

This mechanism, 74 mm $\times$ 40 mm in footprint, must be accommodated on the optical bench at the location of the entrance pupil to the telescope (135 mm from the telescope interface). With the presence of the PAAM on the Tx beam in the critical path, it is desirable to have a direct optical readout of its performance, so we require an additional interferometer, the *PAAM Metrology interferometer*, which combines a sample of the Tx beam (after reflection from the PAAM) with some of the local oscillator. This can directly read out the attitude of the PAAM with DWS and provide direct pathlength stability measurements. It further allows, if necessary, the means to provide a signal to control the PAAM in a feedback loop, or a signal allowing unexpected angular jitter to be corrected for in post-processing.

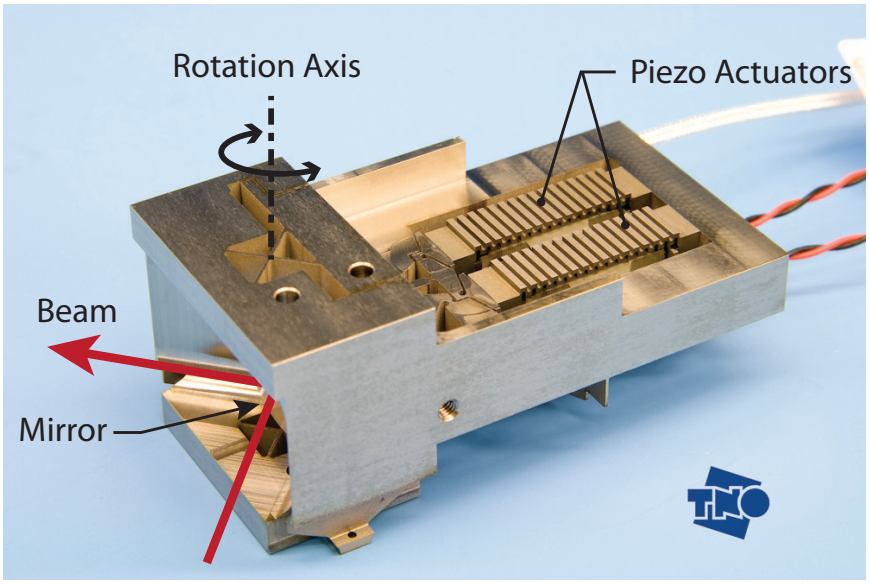

Figure 7.4: *Picture of a prototype point ahead angle mechanism (Courtesy J. Pijnenburg, TNO).*

In the alignment phase of the constellation each spacecraft must align itself in the correct plane and direct its transmit beams to the other spacecraft. To aid in this process, a CCD camera is required. This camera will look into the telescope and is envisaged as both a star tracker to aid with the initial orientation and a wide field of view detector for the Rx beam to control the fine alignment of the spacecraft. Candidate sensors are being studied by the Albert Einstein Institute and have a footprint of around 50 mm × 50 mm.

Optical constraints

Unlike LISA Pathfinder where the heterodyne frequency is ∼ 1.6 kHz, LISA will use multi-MHz heterodyne frequencies. To achieve high bandwidth, it is necessary to use low capacity and hence small diameter photodiodes and also locate suitable front end electronics as close to the diode as possible. This means space must be reserved on the optical bench for representative

electronics at the location of each photodiode. Currently, candidate designs from both EADS Astrium GmbH and the Albert Einstein Institute are of order 50 mm square. The small diameter photodiodes also lead to tight requirements on beam centring at the diodes. Performance simulations to determine the exact tolerance are on-going but initial results suggest that beam centring must be around a few microns. Since both the beam reflected from the test mass and the Rx beam to the science interferometer will potentially be tilted, imaging systems are required in front of the photodiodes at the test mass interferometer and the science interferometer to ensure that the tilt is not converted into a lateral beam displacement at the photodiode. The PAAM metrology interferometer also requires an imaging system since the Tx beam will be moving by very large amounts due to the actuation of the PAAM.

Straylight can introduce unacceptable noise if not controlled carefully. One potential source of straylight are the optical components. All secondary surfaces will be anti reflection coated as a matter of course, but no anti reflection coating is perfect and there will always be second order reflected beams from a component. If the components are parallel sided then the higher order reflected beams will be parallel to the main beam, potentially allowing them to re-enter the main beam by reflecting through another component at 45° and provide a source of phase noise. This is especially dangerous if they scatter back in from an unstable surface as the added phase noise can be larger than the measurement signal. For LISA Pathfinder, the components were parallel sided but were sufficiently thick such that the first and second order reflected beams were separated by $6\,\omega_0$. A detailed study of the propagation of higher order reflected beams was undertaken to confirm that the chosen design was satisfactory [38].

A better, although more complicated, approach would be to use components

which have an angle between the front and back face in the in-plane direction. This would result in the first and second order reflected beams being separated by an angle, greatly reducing the risk of the stray light re-coupling back into the main optical signal. Figure 7.5 shows the difference between the second order reflected beams for parallel and wedged components.

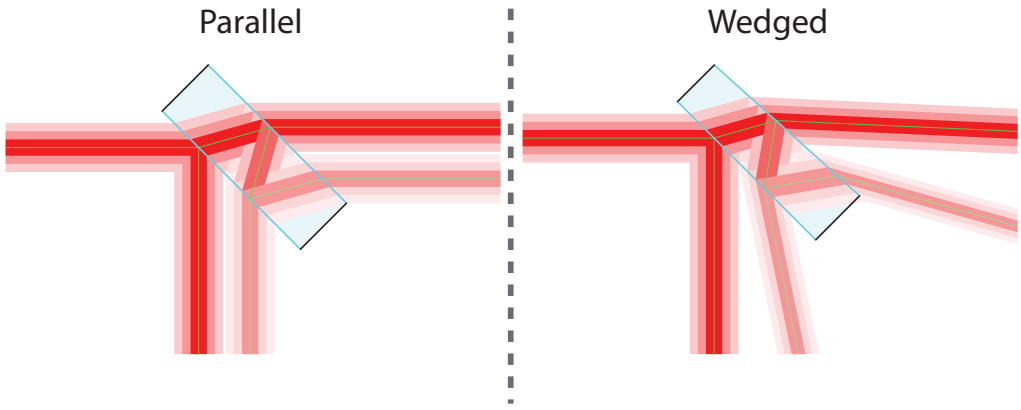

Figure 7.5: *OptoCad [39] model showing the second order reflected beam for a parallel component, and one with a* 3° *wedge.*

LISA will be extremely sensitive to straylight of all forms, especially in the science interferometer where only 200 pW of Rx light is received. As a consequence of this, wedged optics are preferred as they potentially make it easier to minimise the coupling of higher order reflections. Initially, a layout based on the usage of wedged optics for all the optical components was developed. However, simulations based upon the layout brought to light an unexpected consequence of using wedged optics on transmissive components. There are several beams on the optical bench which will have an inherent jitter, such as the beam reflected from the test mass (which is anticipated to have an angular jitter of around 150 nrad/$\sqrt{\text{Hz}}$). This jitter will cause the beam to scan over the surface of a component by a small amount. If the component has a wedge angle, then this movement will cause the beam to travel through a variable length of glass, changing the optical path of the beam and coupling

into the measurement as a direct source of pathlength noise. Figure 7.6 shows the coupling of pathlength noise as a function of wedge angle. The model used to calculate the result is based on geometrical optics, for the specific case of the test mass interferometer. A beam is reflected from the test mass and propagates 300 mm where it is incident on an wedged optical component at angle $\theta_i = 45° + \delta\theta$ (where $\delta\theta$ is the beam jitter of magnitude $150\,\mathrm{nrad}/\sqrt{\mathrm{Hz}}$). The beam exits the component and propagates a further 150 mm to a detector. The simulation computed the peak-to-peak change in optical pathlength from the test mass to the detector caused by the beam jitter, as a function of the wedge angle of the component. For the nominal 3° wedge angle, the added displacement noise is around $7\,\mathrm{nm}/\sqrt{\mathrm{Hz}}$, several orders of magnitude above the measurement signal. Indeed, the simulation shows that to suppress this noise source to an acceptable level (*i.e.* $<< 1\,\mathrm{pm}/\sqrt{\mathrm{Hz}}$) requires that transmissive components are parallel to less than 10^{-4} degrees and ideally around a few 10^{-5} degrees. This corresponds to components which are parallel to within $\sim 1\,\mu$rad, an extremely tight requirement, although not beyond the capabilities of current manufacturing techniques.

As a consequence, the baseline position for LISA is to use parallel components for all optics where there will be a transmitted beam, but to continue to use wedge components for mirrors. The parallel optics must be sufficiently thick to ensure that the main beam is separated from any second order reflections by at least $6\,\omega_0$, as was the case for the LISA Pathfinder optical components. As a further measure, a full analysis of the propagation of second and third order beams will be carried out ensure the design minimises the possibility of these coupling into any measurement signal.

As with LISA Pathfinder, laser frequency noise is an important potential noise source. LISA has far more stringent requirements on laser frequency noise due

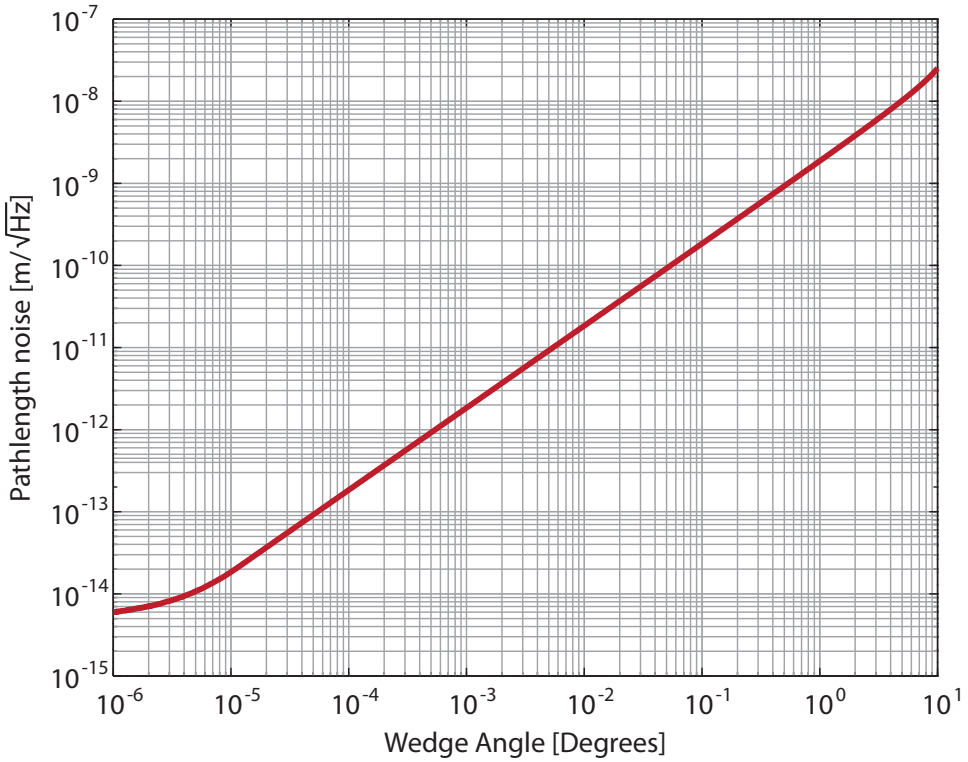

Figure 7.6: *Pathlength noise induced inside a component as a function of wedge angle, for an incident beam with a jitter of magnitude* $150\,\mathrm{nrad}/\sqrt{\mathrm{Hz}}$.

to the huge mismatches in path length caused by the constellation arms being of unequal length. One possible solution is to use a three stage frequency stabilisation scheme to meet the science requirement. The first stage is a laser pre-stabilisation system (such as locking to a cavity). The second stage is to further lock the laser frequency to the arm length of the constellation. This could result in a frequency stability on the optical bench of around $280\,\mathrm{Hz}/\sqrt{\mathrm{Hz}}$. The third stage, required to overcome the huge path length mismatch between the two beams in the science interferometers, is a post-processing technique called time delay interferometry. The technique involves synthesising an equal arm length interferometer by combining the output of one interferometer with a time delayed output of another, such that the frequency noise components are common mode and cancel out [53]. For the optical bench, the frequency stabil-

ity of $280\,\mathrm{Hz}/\sqrt{\mathrm{Hz}}$ can be converted into a path length requirement. A relative path length mismatch between the reference and measurement interferometers of 1 m would couple as a displacement noise of $1\,\mathrm{pm}/\sqrt{\mathrm{Hz}}$. We would ideally like the noise to be an order of magnitude below this, therefore path length mismatches between the reference and the other interferometers should ideally be at the 10 cm level or less.

Implications of redundancy

Due to the LISA mission lifetime of at least 5 years of science operations, ensuring redundancy of all systems is considered to be vital. This includes systems which have no redundancy on LISA Pathfinder such as the laser and associated fibre feeds. On the optical bench level, this requires redundant photodiodes on all interferometers, a redundant acquisition sensor and crucially, redundant fibre feeds to deliver light to the optical bench. In order to achieve redundancy, we must develop a fibre injector system which can switch between two fibre feeds whilst simultaneously maintaining the alignment of the optical bench at the few micron and $10 - 20\,\mu$rad level.

Two fibre injectors will be bonded to a small sub baseplate. The beams from these fibre injectors will have orthogonal polarisation states such that they can be combined into two collinear beams using a polarising beam splitter. A half-wave plate, located inside a rotating mechanism (in development at TNO) can then be used to correct the polarisation of the active beam back to desired state. An output polariser will then be used to clean up the polarisation state to around 1000 : 1. A CAD rendering of the concept design can be seen in Figure 7.7. The two FIOS are conceptually very similar to those constructed for LISA Pathfinder, shown in Figure 5.3 on Page 74. To provide added durability against contamination of the small fibre end, a small wedged cover slip will be

catalysis bonded to the front face of the silica block containing the fibre. This will allow the beam to expand into silica for the first few millimetres and lower the optical power density at the eventual output face.

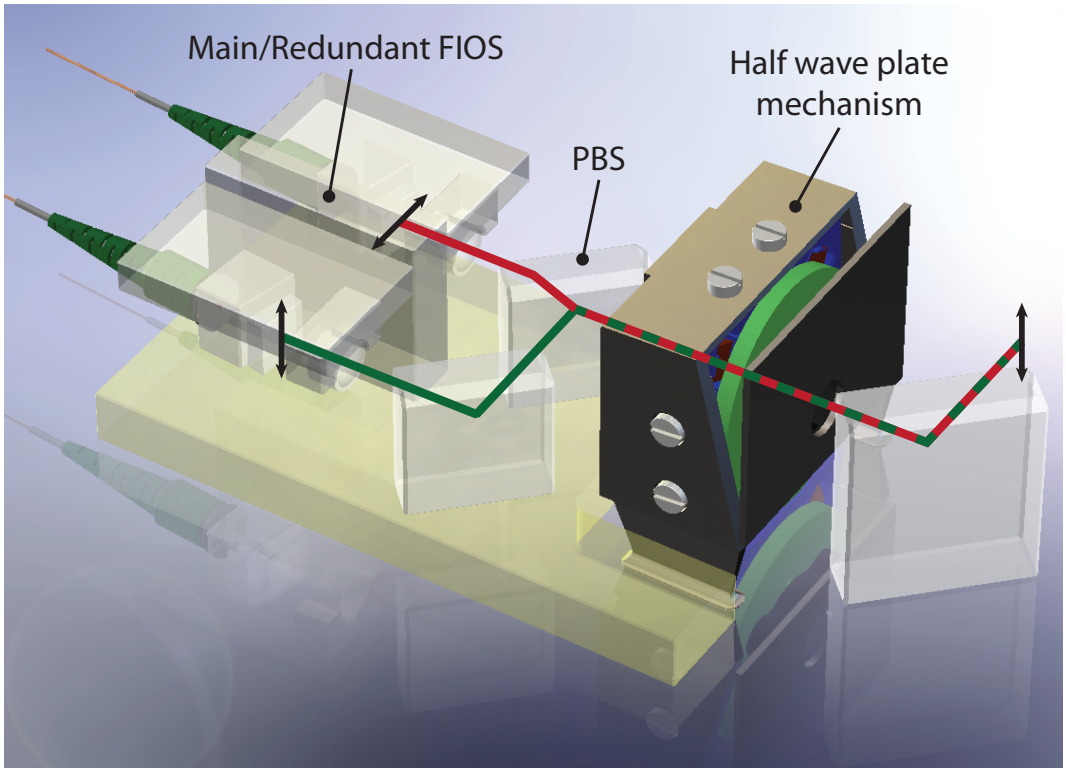

Figure 7.7: *CAD Rendering of the concept LISA redundant fibre injector system.*

The FIOS will be bonded to a mounting post using the same technique as developed for LISA Pathfinder, with the absolute alignment to the sub-baseplate controlling the out-of-plane pointing of the beam for the OB (for a sufficiently parallel sub-baseplate). The relative alignment between the two will control the out-of-plane coaxiality of the main and redundant beams. The PBS can then be precision bonded, controlling the in-plane coaxiality. This subassembly, in combination with the waveplate mechanism and an output polariser, forms a single LISA fibre injector system. The resulting design is relatively large, with a footprint of approximately 130 mm × 60 mm. Two of these must

be accommodated on the optical bench, one for the Tx beam and one for the local oscillator beam.

7.3 Optical bench layout

Working to the requirements outlined above a detailed design for the prototype LISA optical bench has been developed. Significant effort was put into the design to ensure that it is manufacturable, *i.e.* that its design is compatible with the alignment techniques developed for LISA Pathfinder. For example, if a beam which needed to be measured with the CQP to allow the alignment of a beam to the test mass were blocked by an already bonded component, it would potentially render alignment to the test mass impossible. Thus the design must ensure that such situations do not arise.

7.3.1 Constraints on layout

Fixed interface points

The first requirements that must be considered are those of the fixed optical interfaces: the test mass, optical truss and telescope. There is some freedom in the exact positioning of the telescope interface, in that it should be within 50 mm of the centre of the bench. What we are not free do to, however, is arbitrarily define the orientation with which we launch the beam to the telescope. The plane in which the point ahead angle is actuated must be translated to the appropriate direction in the constellation. This requires that, in a reference frame centred on the OB, with the surface forming the x-y plane, the Tx beam must be launched towards the telescope interface mirror

in a positive y direction. Since the centre of the OB is occupied by the mirror reflecting the beam to the test mass, this leaves us only three locations in which the telescope interface mirror can be placed: one to the positive x side of the test mass interface; its mirror image on the negative x side; and a third to the negative y side. This is shown on the left hand side of Figure 7.8. Further restrictions come from consideration of the required beam geometry: firstly the high power Tx beam should ideally experience an all-reflective path to minimise the number of surfaces encountered, and thus the risk of straylight; secondly the Tx and Rx beams must be multiplexed at a polarising beam splitter; and thirdly, to extract a small amount of the Tx beam for the PAAM metrology, and provide a small amount of light for the acquisition sensors, there must be a further beamsplitter between the PBS and the telescope entrance. Taking into account these considerations, plus the requirement to have the PAAM at the entrance pupil to the telescope (135 mm from the interface position), we can derive the arrangement shown on the right hand side of Figure 7.8. Due to the short distance between the PAAM and the telescope entrance, symmetrical versions of this layout through the x-axis are ruled out as they would lead to the PAAM being inside the telescope entrance, or the telescope entrance blocking beams. Therefore only this arrangement, and the symmetrical version through the y axis, satisfy our requirements.

When this arrangement is tested in the three possible locations of the telescope entrance, location 3 places the acquisition sensors off the edge of the baseplate and so is not practical. Since symmetries in the x-axis result in blocked beams or overlapping components, this leaves us with two choices: the exact arrangement depicted in Figure 7.8 in position 1, or its mirror image about the y-axis in position 2. The final constraint is the fixed location of the optical truss interface points. For location 2 the positioning of the acquisition sensors becomes problematic, with the position of one optical truss point conflicting with

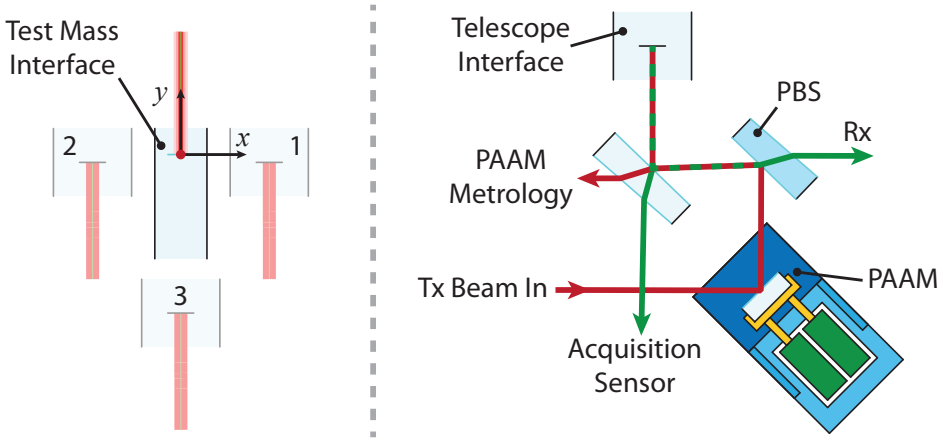

Figure 7.8: *Left hand side: The three possible locations for the telescope interface that meet the requirements. Right hand side: Required beam geometry from constraints on the Tx and Rx beam.*

the required location of the acquisition sensors. This is shown in Figure 7.9. Location 1 does not have this conflict and so is the only viable location for the telescope interface location for these requirements.

With the geometry of the relevant portion of the OB fixed, the number of suitable locations for many other components, especially the acquisition sensors, PAAM metrology interferometer and the Science interferometer, become limited.

Manufacturability

With these elements largely defined, the remaining components (the test mass interferometer, reference interferometer, beam expander and the two fibre injectors) will have their positions determined by:

- the beams already defined by the location of the telescope interface and test mass interface;

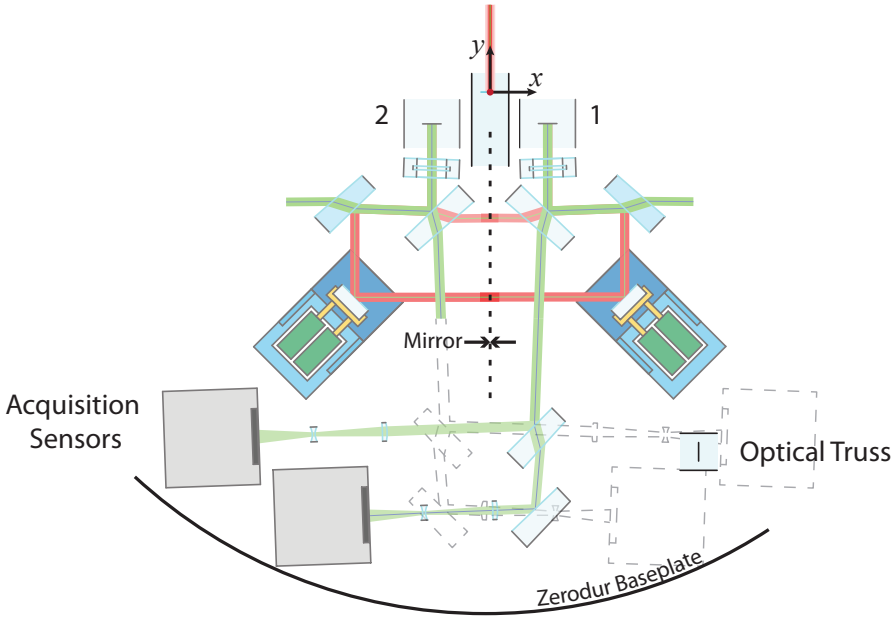

Figure 7.9: *Diagram showing conflicts between the optical truss and telescope interface location two.*

- the desire to have path length matching to around 100 mm or better to minimise the coupling of laser frequency noise;
- required alignment tolerances;
- consideration of manufacturability.

This last criterion is especially important and requires careful planning to ensure that, for a given layout, there are no conflicts between alignment stages. For the LISA OB this is significantly more difficult than for LISA Pathfinder, in part due to the number of components and the complexity of the design, but also due to having tightly toleranced beam alignments in the centre of the OB (the test mass and telescope interfaces). In line with the alignment philosophy described in Chapter 4, the 45° mirrors will only be used to control two degrees of freedom, the other two critical degrees of freedom must be controlled at the component immediately preceding the out-of-plane steering

optics. This requires that for alignment of these interfaces we must be able to measure the beams, *i.e.* there must be a clear path from the centre of the OB to the outside to facilitate beam measuring with the CQP. Maintaining such a clear path is not feasible in the overall layout due to space constraints so these beams must be aligned early in the alignment plan, with later stages 'filling in' the area used to access the beams. As shown in Figure 7.8, these two beams propagate in opposite directions: the test mass beam in a negative y direction, and the telescope beam in a positive y direction.

Since both the beam to the test mass and the telescope originate from the same fibre injector, that of the Tx beam, clearly this subsystem must be in place first. Also, the Tx beam expander and the PAAM are required to direct the Tx beam to the telescope. The local oscillator fibre injector, however, is not required. Nor are any of the interferometers or the acquisition sensors. This leaves them as the possible candidates for placing into the space required for these alignment beams.

Alignment

The layout of the interferometer can also have an effect on the alignment tolerances required of the various subsystems. The primary - or top level - alignment requirements are on the various interfaces [57]:

- the Tx beam to the telescope must be aligned to the received Rx beam to within 20 μm to minimise noise from spacecraft jitter;
- the optical truss beams must be aligned to within 50 μm of their nominal position;
- the beam reflected from the test mass must be aligned to a precision of

better than 35 μm;

- the beams at the reference and test mass interferometers must be aligned to within 50 μm and 100 μrad of each other to achieve good measurement performance;
- the beams at the science interferometer must be aligned to within 25 μm and 50 μrad of each other to achieve good measurement performance;
- all these requirements must be met for both the main and redundant setting of the fibre injectors.

Based on these top level requirements, we can derive a set of secondary requirements. These are requirements placed upon the various subsystems - especially the fibre injector system and the Tx beam expander - that they must meet in order to satisfy the primary requirements. These secondary requirements, however, are layout dependant. The layout dependence of these tolerances is illustrated in Figure 7.10. If a beam from a FIOS is required to meet two alignment tolerances of $\pm 10\,\mu$m at two different distances, then the angular (ϕ) and positional (h) tolerances on the FIOS for which it can meet the two requirements is dependant on the distance to the points, and especially on the distance between them, d. Since reducing d will increase the effective 'field of view', it will also increase the allowable values of ϕ and h. For very small d, or ideally two coincident points, the positional and angular tolerances can be very large, so long as the beam still passes though the one point in space. If they were separated by a metre however, then the beam would have to be within 20 μrad and a few μm of the nominal to be sure of meeting both tolerances. From this, it becomes clear that the optical layout can then be optimised to place all the tight interface alignments so as to minimise d, and thus increase the derived tolerances on the subsystems reducing the complexity of their alignment.

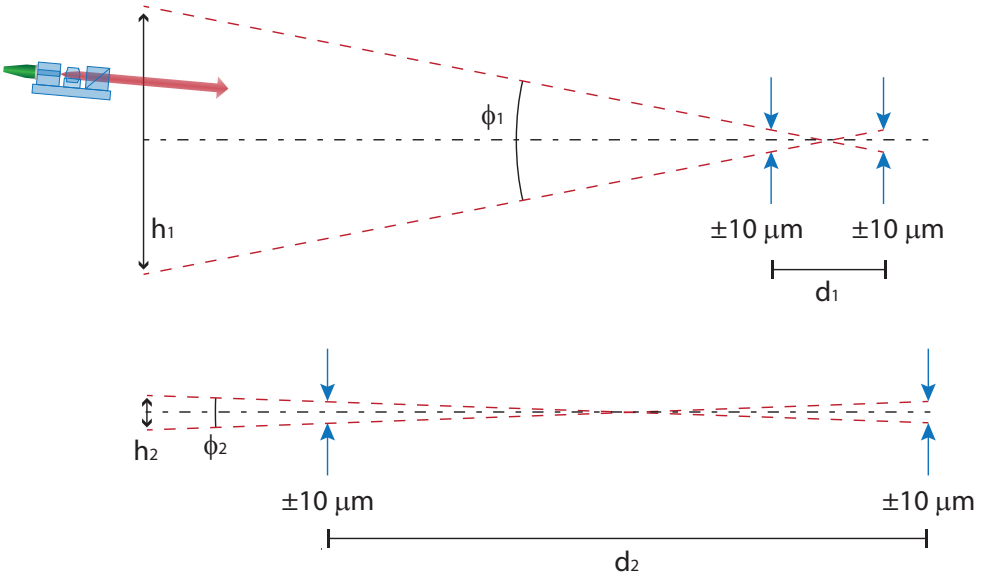

Figure 7.10: *Diagram illustrating the dependance of the layout on the positional tolerances of a fibre injector.*

7.3.2 Optical layout

Based on the requirements outlined in Section 7.2 and the design considerations detailed above, a layout has been developed in Optocad [39]. The full layout is shown in Figure 7.11, with the numbered annotations defined in Table 7.1. Due to the complexity of the design, Figures showing the individual interferometers and optical paths can be found in Appendix A for clarity.

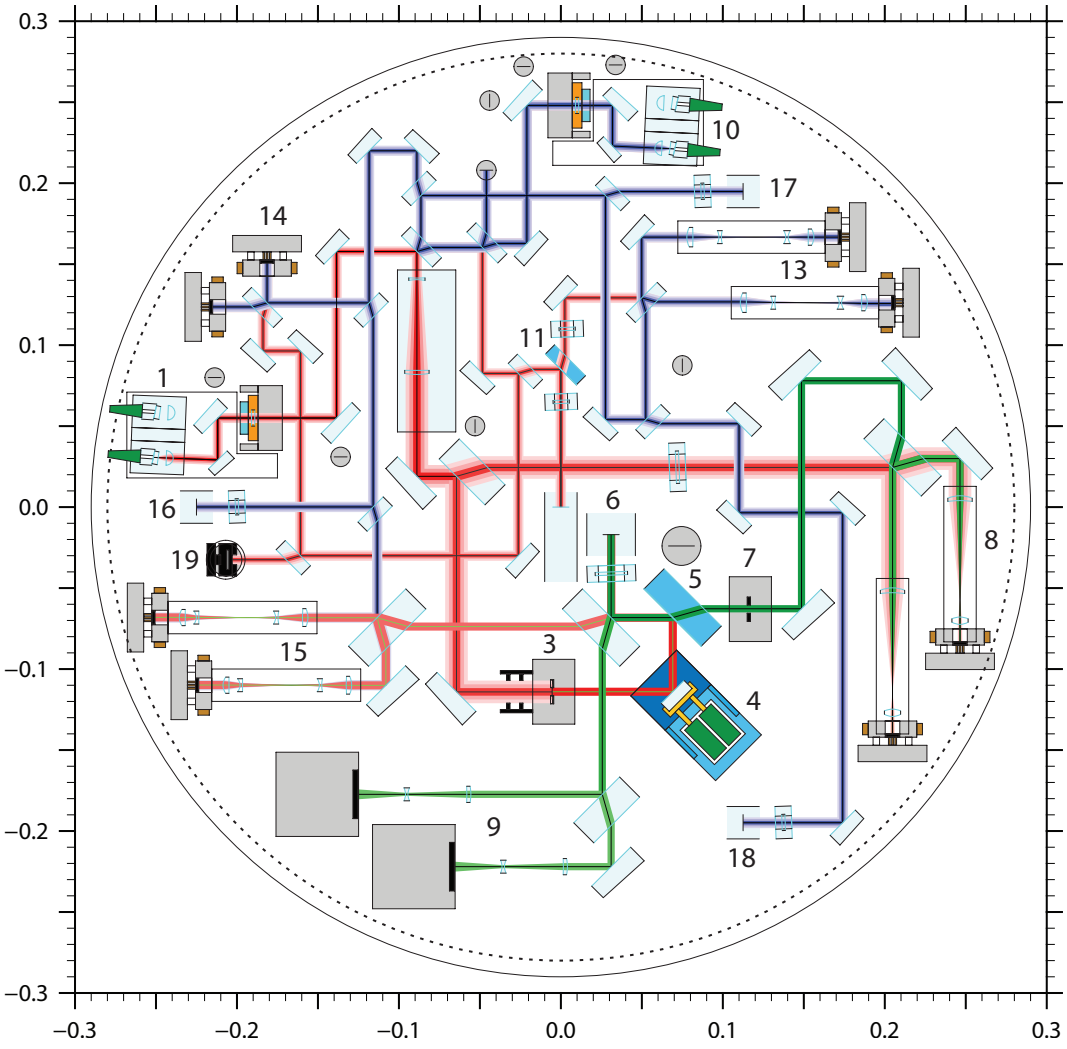

Figure 7.11: *OptoCad [39] model of the prototype LISA optical bench. The numbered annotations are defined in Table 7.1. The scale is in metres.*

Table 7.1: *Legend for annotations in Figure 7.11.*

N°	Description	N°	Description
1	Fibre injector for the Tx beam	11	PBS for beam steering to the test mass
2	Tx Beam Expander	12	Test mass interface
3	Tx Beam Clipping	13	Test mass read-out interferometer
4	PAAM	14	Reference interferometer
5	PBS for Tx/Rx multiplexing	15	PAAM metrology interferometer
6	Telescope interface (Tx up/Rx down)	16	Optical truss 1
7	Rx Beam Clipping	17	Optical truss 2
8	Science interferometer	18	Optical truss 3
9	Acquisition sensors	19	Tx power monitor
10	Fibre injector for the local oscillator beam		

General features of the design

The layout utilises a footprint of diameter 560 mm, with the baseplate for the prototype being 580 mm in diameter. This is slightly larger than the reference design (which was $\sim$ 500 mm). This is due to a number of factors, chief amongst which was the larger than anticipated size of subsystems such as the photodiode imaging systems (designed by Alexander Sohmer from EADS Astrium GmbH), photodiode electronics and redundant fibre injector system.

To help mitigate against second and third order reflections, all reflecting com-

Interferometer	Relative mismatch to reference interferometer	Predicted displacement noise
Test Mass	125 mm	$0.13\,\mathrm{pm}/\sqrt{\mathrm{Hz}}$
Science	78 mm	$0.08\,\mathrm{pm}/\sqrt{\mathrm{Hz}}$
PAAM Metrology	4 mm	negligible

Table 7.2: *Path length matching between the the reference and measurement interferometers for the prototype LISA OB layout. The displacement noise given is based on the predicted laser frequency noise of* $280\,\mathrm{Hz}/\sqrt{\mathrm{Hz}}$ *detailed in Section 7.2.2*

ponents are wedged at an angle of 3°, and all transmissive components are sufficiently thick such that the reflections are separated from the main beams by at least $6\,\omega_0$. These actions alone do not entirely guarantee that a back reflected beam will not re-enter the main beam path, but it does reduce the risk. As a further mitigation, the propagation of all second and third order reflections will be modelled to ensure that no reflections couple into a measurement.

The path length matching requirement was particularly challenging due to the large propagation distance of the Tx beam to the test mass interferometer. This beam path includes the 355 mm round trip of the beam below the OB to the test mass and back. The result is a somewhat elaborate routing of the Tx beam to the reference interferometer but it does result in good path length matching. The values are detailed in Table 7.2.

These path length differences are broadly compliant with the goal of having path length mismatches of around 100 mm or less. For the science interferometer, the mismatch given is between the Tx beam to the reference interferometer and the Tx beam to the science interferometer. The frequency noise of the Rx

beam is cancelled using the time delay interferometry technique discussed in Section 7.2.2.

Manufacturability

Ensuring that the resulting optical bench was manufacturable required the development of an alignment plan as the layout was developed. This is summarised below.

1. Bond the (pre-assembled) Tx beam fibre injector in place.
2. Bond (using a template) the optics between the Tx fibre injector and the PBS directing the beam to the test mass.
3. Precision align and bond the PBS to ensure alignment to the test mass in the in-plane degrees of freedom.
4. Precision align and bond the 45° mirror to direct the beam to the nominal test mass reflection point.
5. Precision align and bond the (pre-assembled) Tx beam expander to align its optical axis in the in-plane degrees of freedom.
6. Template bond the components between the Tx beam expander and the Tx beam clipping.
7. Precision align and attach the Tx beam clipping aperture.
8. Precision align and mount the PAAM.
9. Bond the PBS to multiplex the Tx and Rx beams to/from the telescope.
10. Precision align and bond the beamsplitter to direct the beam to the telescope interface.

11. Precision align and bond the 45° mirror directing the Tx beam up to the telescope.

12. Bond the (pre-assembled) local oscillator beam fibre injector.

13. Couple the Tx beam to the local oscillator fibre injector to establish the backlink by precision bonding the output polariser.

14. Template bond the components directing the Tx and local oscillator beam to the reference interferometer.

15. Precision align and bond the reference interferometer combiner.

16. Precision align and bond the beamsplitter directing the local oscillator beam to optical truss interface 1 for the in-plane degrees of freedom, then the 45° mirror to control the out-of-plane degrees of freedom.

17. Precision align and bond the PAAM metrology combiner.

18. Template bond the optics directing the local oscillator and Tx beams to the test mass interferometer.

19. Precision align and bond the test mass interferometer combiner.

20. Precision align and bond the 45° mirror for optical truss interface 2.

21. Template bond the components directing the local oscillator beam to optical truss interface 3.

22. Precision align and bond in-plane mirror and the 45° mirror for optical truss interface 3.

23. Template bond the optics directing the Tx and Rx beams to the science interferometer.

24. Precision align and bond the science interferometer combiner.

25. Precision align and bond the (pre-assembled) imaging systems for the test mass, PAAM metrology and science interferometers.

26. Align and attach the photodiodes and electronics for the eight interferometer read-outs.

27. Align and attach the acquisition sensors.

This alignment plan ensures that all required beams are visible and measurable at all stages of construction.

Alignment tolerances

One important point of this alignment plan is that it allows simplification in the alignment of the Tx beam to the telescope. As discussed in Section 7.3.1, we require that the Tx and Rx beams are aligned to within 20 μm of each other to minimise the effects of spacecraft jitter. This is a tight tolerance and would be hard to meet in an absolute sense. Here, by aligning the telescope interface before we align the science interferometer (*i.e.* before we define the DWS bias signal for the science interferometer) we can align the Tx beam with considerably looser tolerances. Then, by measuring the aligned Tx beam to the required precision we define where the Rx beam must be received to meet the 20 μm tolerance. With this beam defined, the science interferometer can be aligned and bonded for this Rx beam, with the DWS bias signal then defining the Rx beam vector for which the 20 μm tolerance is fulfilled. On orbit, the spacecraft can be oriented such that the science interferometer has this DWS signal, thus ensuring that the required Tx to Rx alignment is correct.

This strategy also greatly simplifies the alignment of the Tx Beam Expander. Since the alignment to the telescope is less critical, the driving requirement on

how much the Tx beam expander can deviate a beam in pointing is determined by the allowable deviation of the Tx beam at the science interferometer. From Section 7.3.1, the two beams at the science interferometer must be aligned to within 25 μm and 50 μrad of each other. However, we have now created the situation where the position of the Rx beam is dependant on the position of the Tx beam at the telescope. The result is that any height deviation of the Tx beam results in the nominal Rx beam also being deviated in height by the same amount to meet the 20 μm telescope centring tolerance and consequently the beams will end up being matched in height at the science interferometer. So the system is (to first order) insensitive to height deviations of the Tx beam after the Tx beam expander. Further, any angular deviations of the Tx beam can be split out into an angular and a height component at the telescope interface. The height component is compensated by the same mechanism if the path length from the Tx beam expander to the telescope and science interferometers is well matched. For the layout of Figure 7.11 there is a small delta of around 100 mm in this path length matching. The angle of the Tx beam is re-set at the PAAM (to ensure the correct point ahead angle to the far spacecraft), and the Rx beam will be defined to be as close to normal as possible. Therefore, the angular deviation of the Tx beam through the Tx beam expander leads to a tilt offset on the Tx beam at the science interferometer of the same magnitude and a small height component equal to the angular offset propagating over 100 mm. This creates a relatively forgiving set of tolerances of around $\pm 30\,\mu$m and $\pm 50\,\mu$rad for the beam deviation though the Tx beam expander. We can also construct the Tx beam expander for the specific beam which is being launched into it allowing us to define an even looser set of tolerances on the required alignment of the Tx beam before the Tx beam expander.

For deriving the required absolute alignment of the beams from the fibre injectors we are left with the alignment of the beam to the test mass, and the align-

ment of the beams at the reference interferometer as the driving requirements. Apportioning around $10 - 15\,\mu$m of the alignment budget for the coaxiality of the main and redundant beams, we end up with tolerances on the absolute alignment of around $\pm\,20 - 25\,\mu$m. These tolerances are similar in magnitude to those with which the LISA Pathfinder OBI was constructed.

Potentially the most demanding requirement is the collinearity between the main and redundant beams from the fibre injectors. One position where this is potentially challenging is for the alignment of the telescope interface. Although the alignment plan eases the requirements on the *absolute* positioning of the Tx beam at the telescope, the Tx to Rx centring requirement applies to both the main and redundant setting of the Tx fibre injector. Apportioning some reasonable error to the position of the Rx beam (say $10\,\mu$m) we end up with the requirement that the main and redundant Tx beams are within $20 - 30\,\mu$m of each other at the telescope interface. The nominal Rx beam is then defined to be the bisector of these two beams. The magnification of the Tx beam expander further tightens this requirement by a factor of two. The second limiting position for the collinearity of the main and redundant Tx beams is the alignment to the nominal test mass reflection point. Here both beams must be aligned to the nominal reflection point to within $35\,\mu$m. Most of this we wish to apportion to the absolute alignment, leaving us with $10 - 15\,\mu$m for the relative alignment on the main and redundant beams. The third limiting position is the reference interferometer. From a similar argument we can apportion around $20\,\mu$m of error at this point. From the layout, the test mass interface and telescope interface have near identical path lengths from the Tx fibre injector. The reference interferometer is around 150 mm further in path length. This sets the requirement on collinearity for the two beams from the Tx fibre injector to be around $25\,\mu$rad and $10\,\mu$m.

Using this alignment plan, the tolerances derived are all similar in magnitude to those which the LISA Pathfinder OBI was constructed to (see Figure 4.7 on Page 69). The successful completion of the LISA Pathfinder optical bench demonstrates that the metrology and alignment techniques developed for LISA Pathfinder, as well as the constructional approach, are directly applicable to the construction of the LISA optical bench and gives confidence that this approach can produce an optical bench of the required precision and durability for LISA.

Chapter 8

Outlook

The direct detection of gravitational radiation, widely believed to be achievable with second generation ground based detectors (if not before), offers the opportunity to start a new field in astronomy. The gravitational wave spectrum is predicted to be rich in sources, many of which are not visible with standard electromagnetic techniques. LISA will aim to detect sources in the mHz region of the spectrum, a part not visible to ground based detectors. LISA Pathfinder will test key technologies for LISA, paving the way for LISA to potentially fly in the 2020 to 2025 time frame.

With the flight model interferometer for LISA Pathfinder completed, and other components of the spacecraft nearing completion, integration can begin, allowing LISA Pathfinder to fly around 2012 to 2013. Even before launch, significant insight into some of the technology required to make LISA a reality has been gained through the research and development for LISA Pathfinder. Efforts to further the construction, measurement and interferometry techniques developed for LISA Pathfinder to a level suitable for LISA are under way with significant progress already made. By the time LISA Pathfinder launches, a

fully representative prototype of the LISA optical bench will have been built, and its performance tested. In parallel, much of the other technology required for LISA that LISA Pathfinder will not test, such as the telescope and MHz phase measuring systems are under development.

With the launch of LISA Pathfinder, we should unambiguously be able to demonstrate that the technology is suitable for LISA and investigate and characterise the noise performance of the system to inform on design choices for LISA.

Appendix A

LISA optical bench layout diagrams

The layout for the prototype LISA optical bench presented in Chapter 7 is a complicated design. The following Figures show the design broken down into individual interferometers and optical paths for clarity.

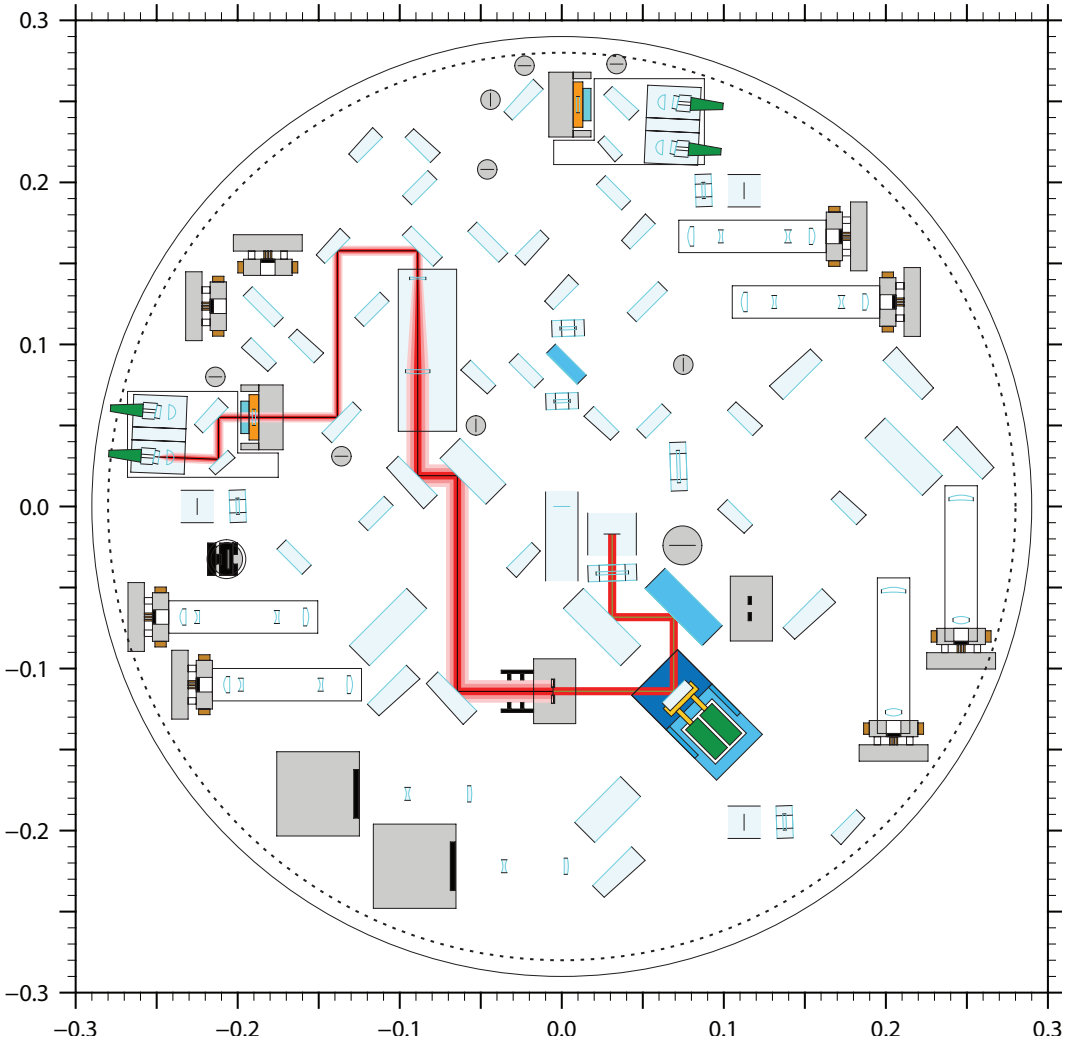

Figure A.1: *OptoCad model of the prototype LISA optical bench showing the path of the Tx beam to the telescope. The scale is in metres.*

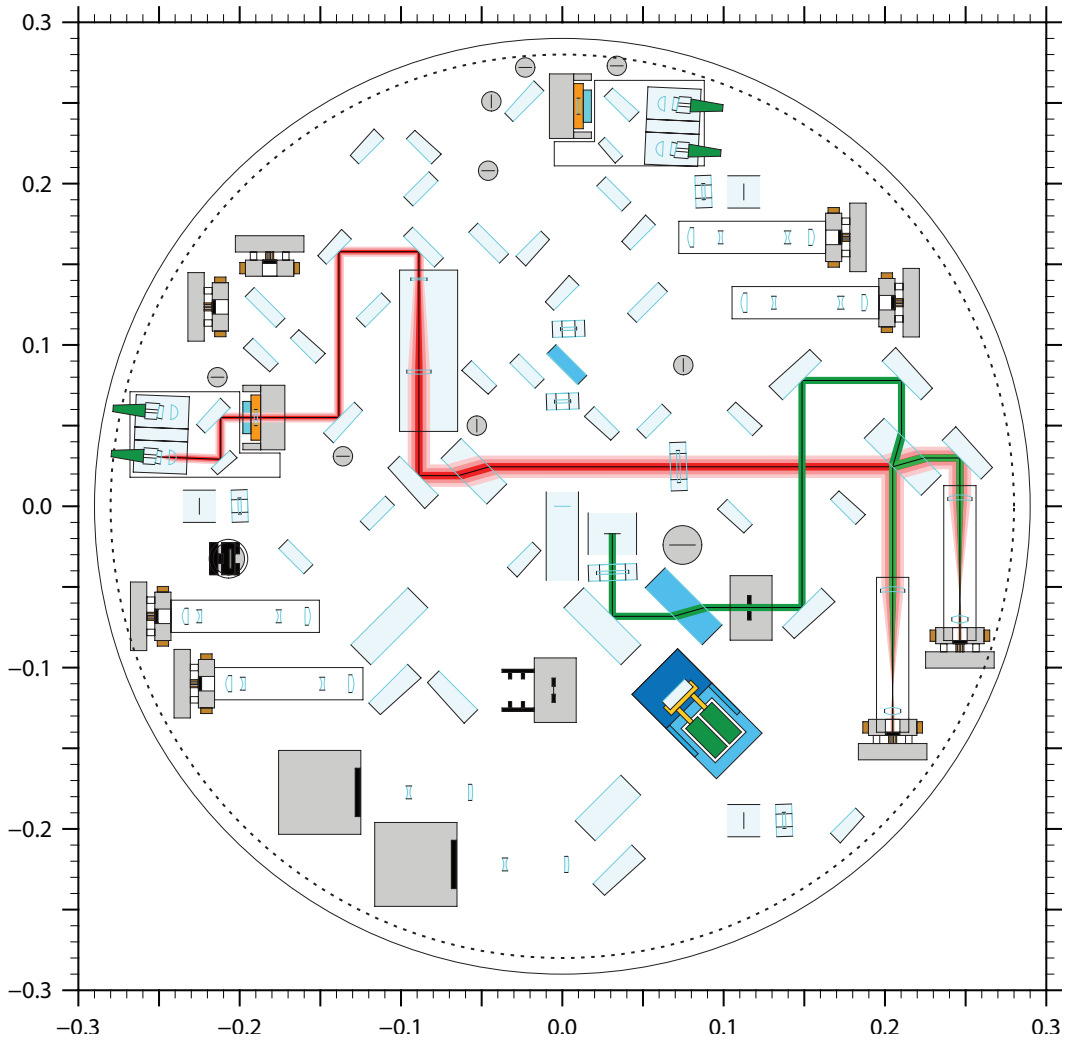

Figure A.2: *OptoCad model of the prototype LISA optical bench showing the science interferometer. The scale is in metres.*

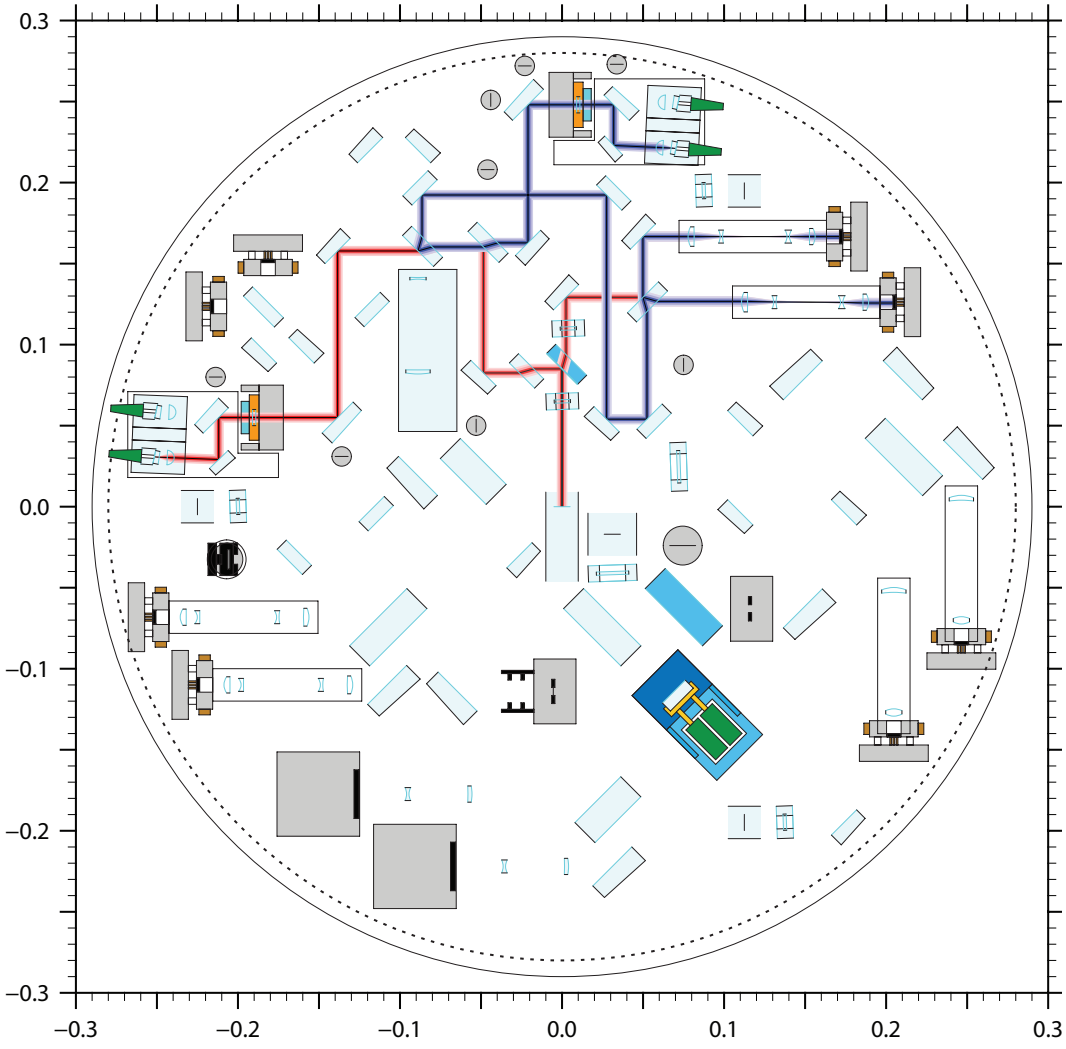

Figure A.3: *OptoCad model of the prototype LISA optical bench showing the test mass read-out interferometer. The scale is in metres.*

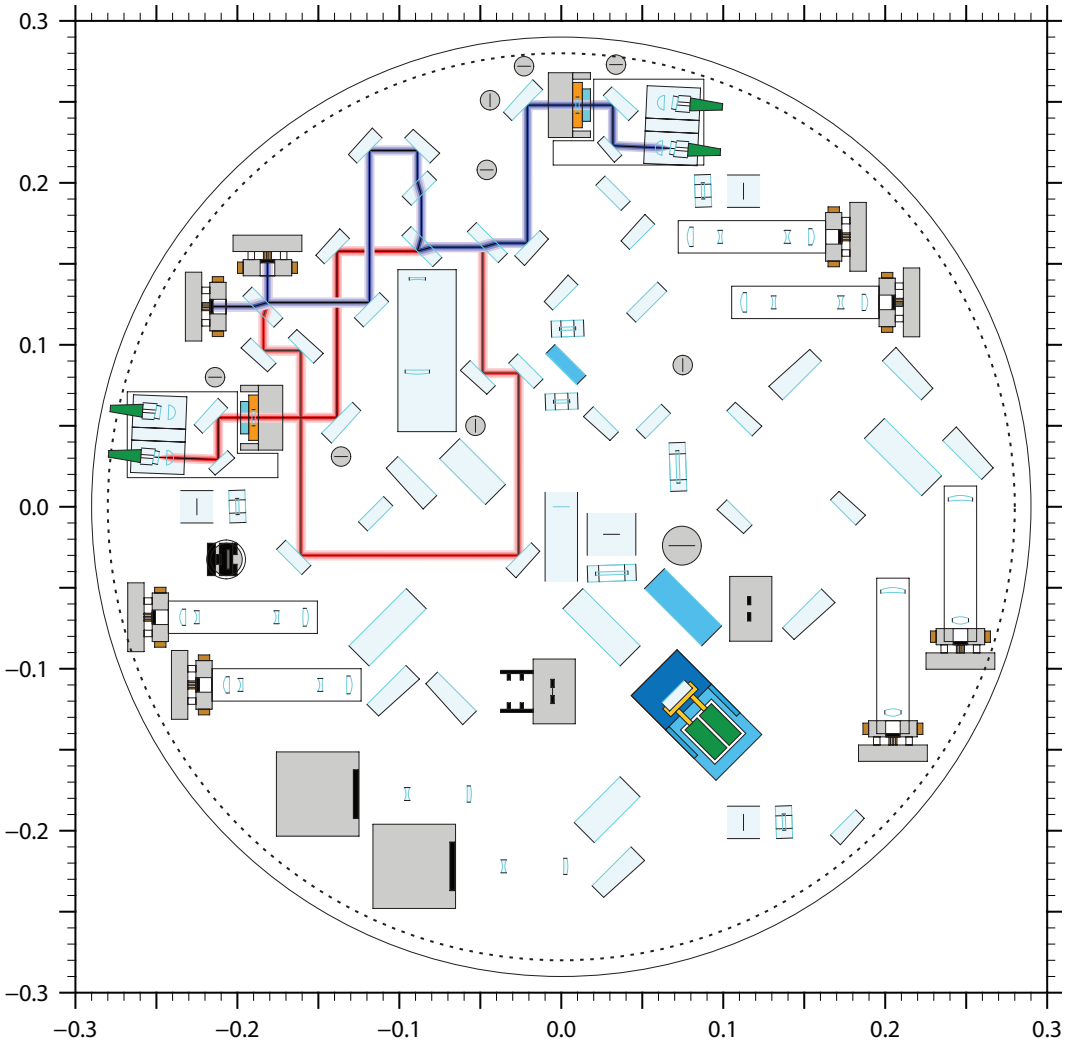

Figure A.4: *OptoCad model of the prototype LISA optical bench showing the reference interferometer. The scale is in metres.*

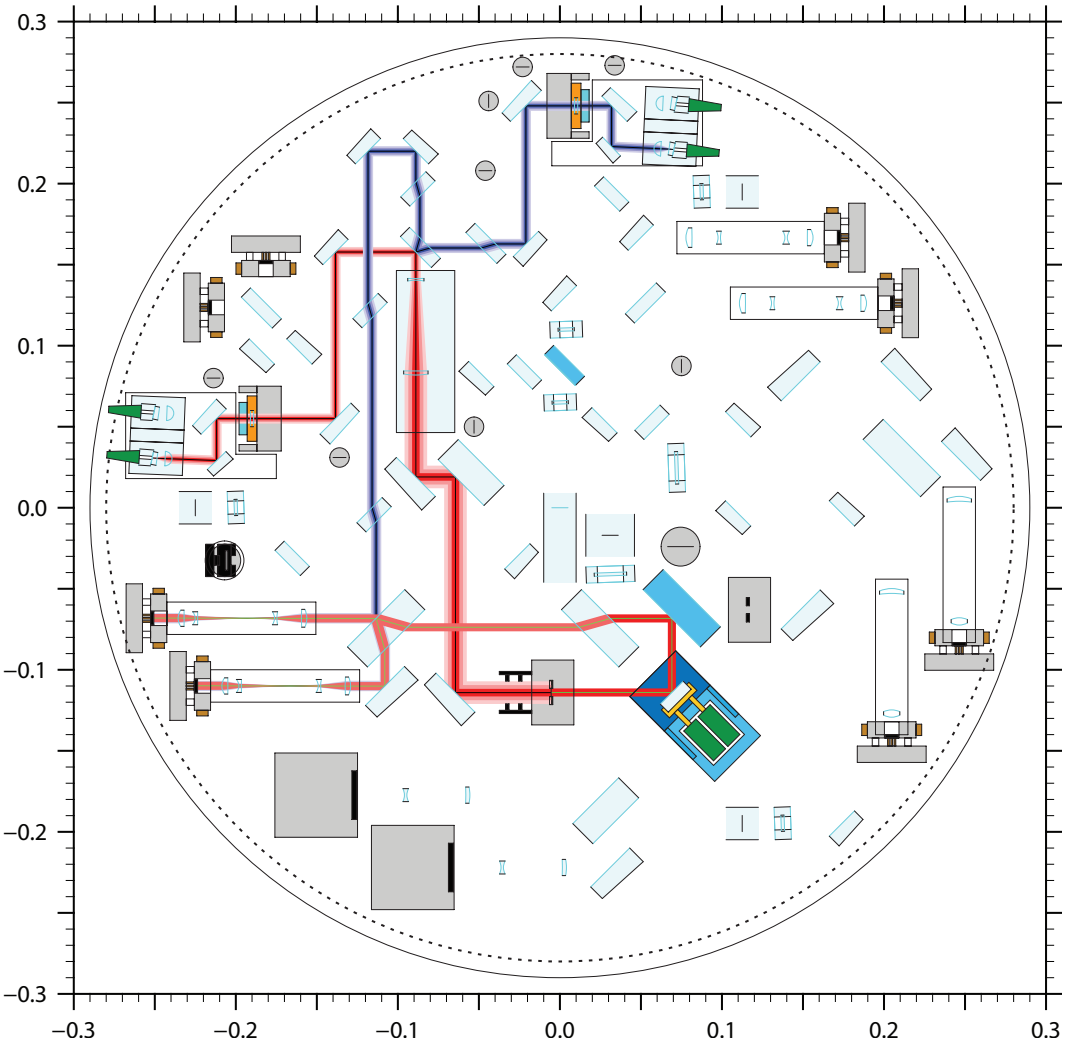

Figure A.5: *OptoCad model of the prototype LISA optical bench showing the PAAM metrology interferometer. The scale is in metres.*

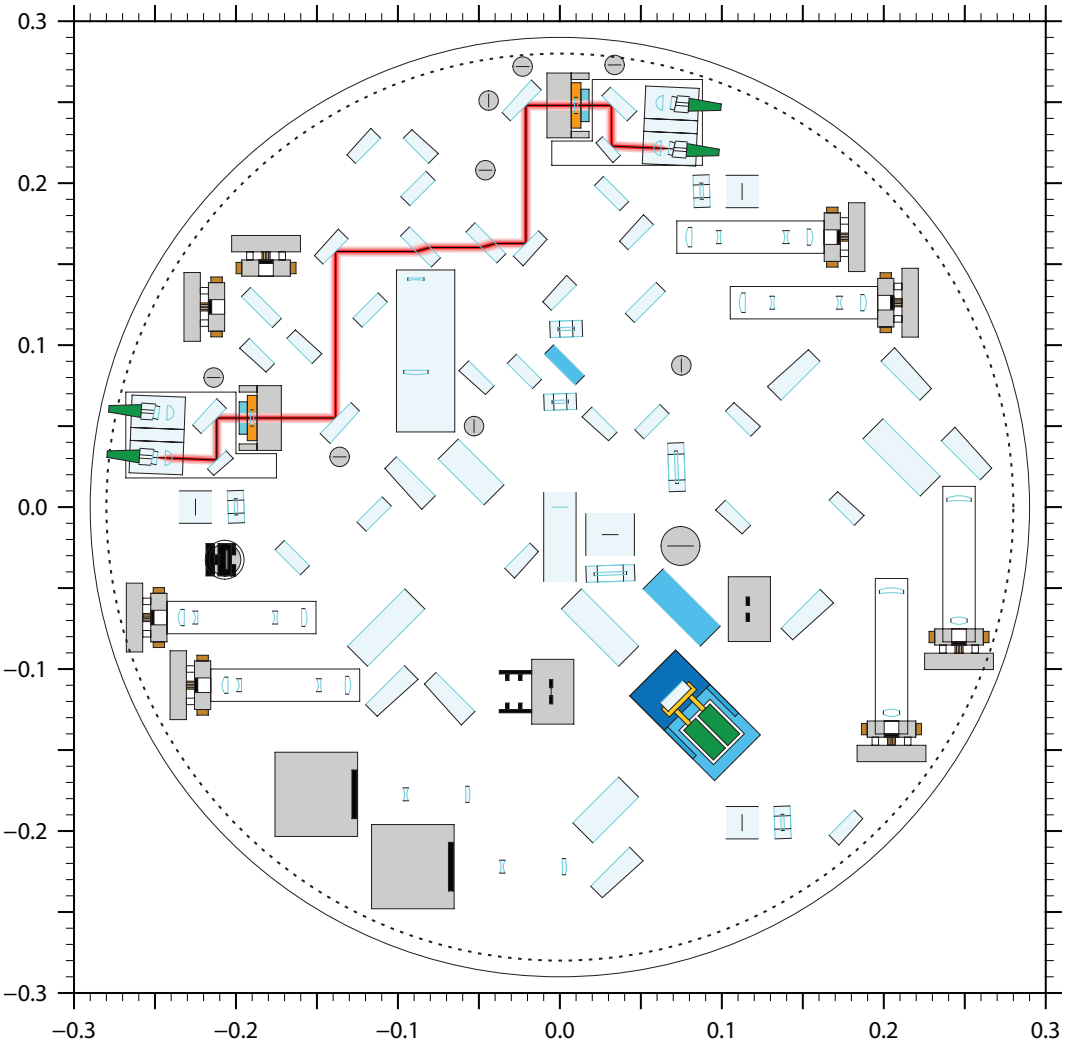

Figure A.6: *OptoCad model of the prototype LISA optical bench showing the Tx beam path to the backlink fibre. The scale is in metres.*

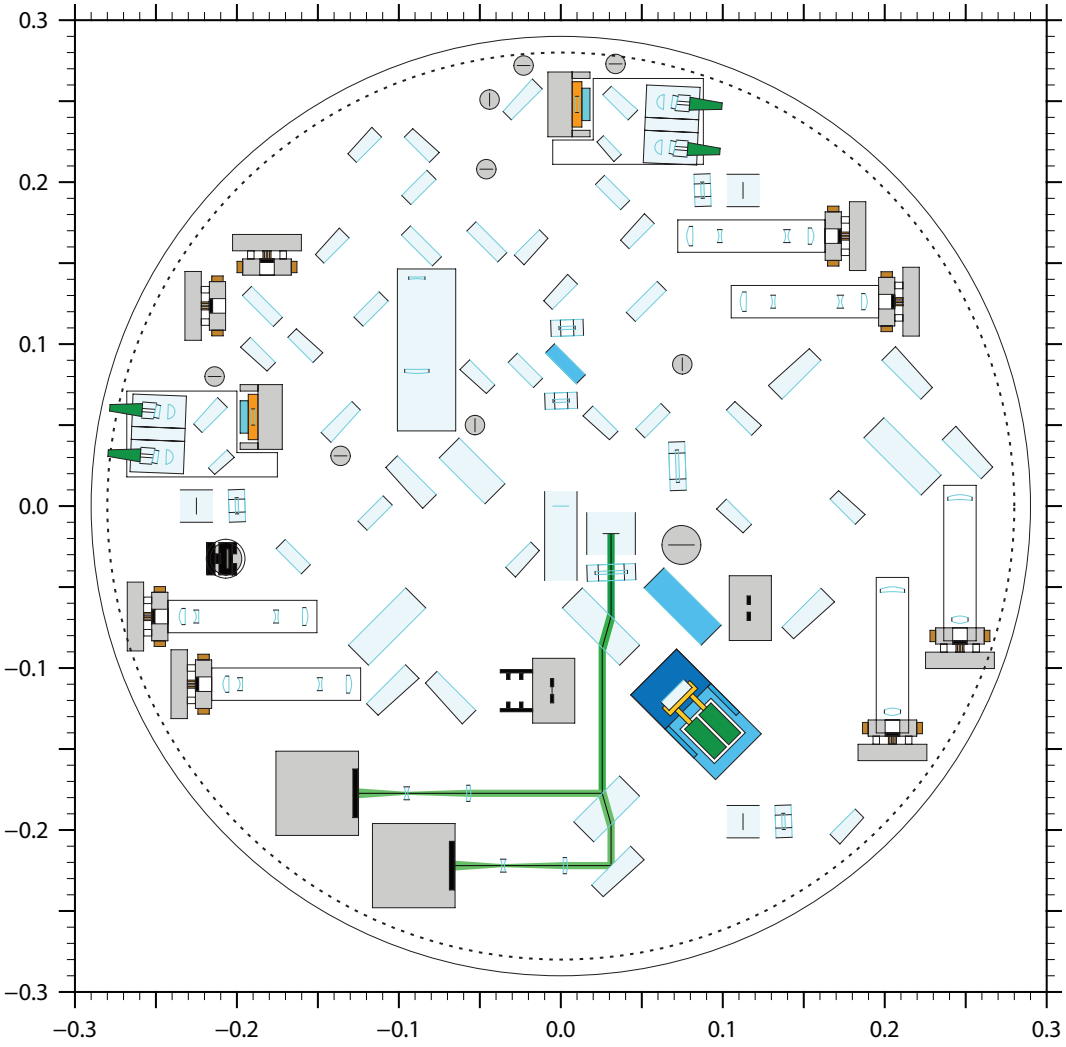

Figure A.7: *OptoCad model of the prototype LISA optical bench showing the acquisition sensors. The scale is in metres.*

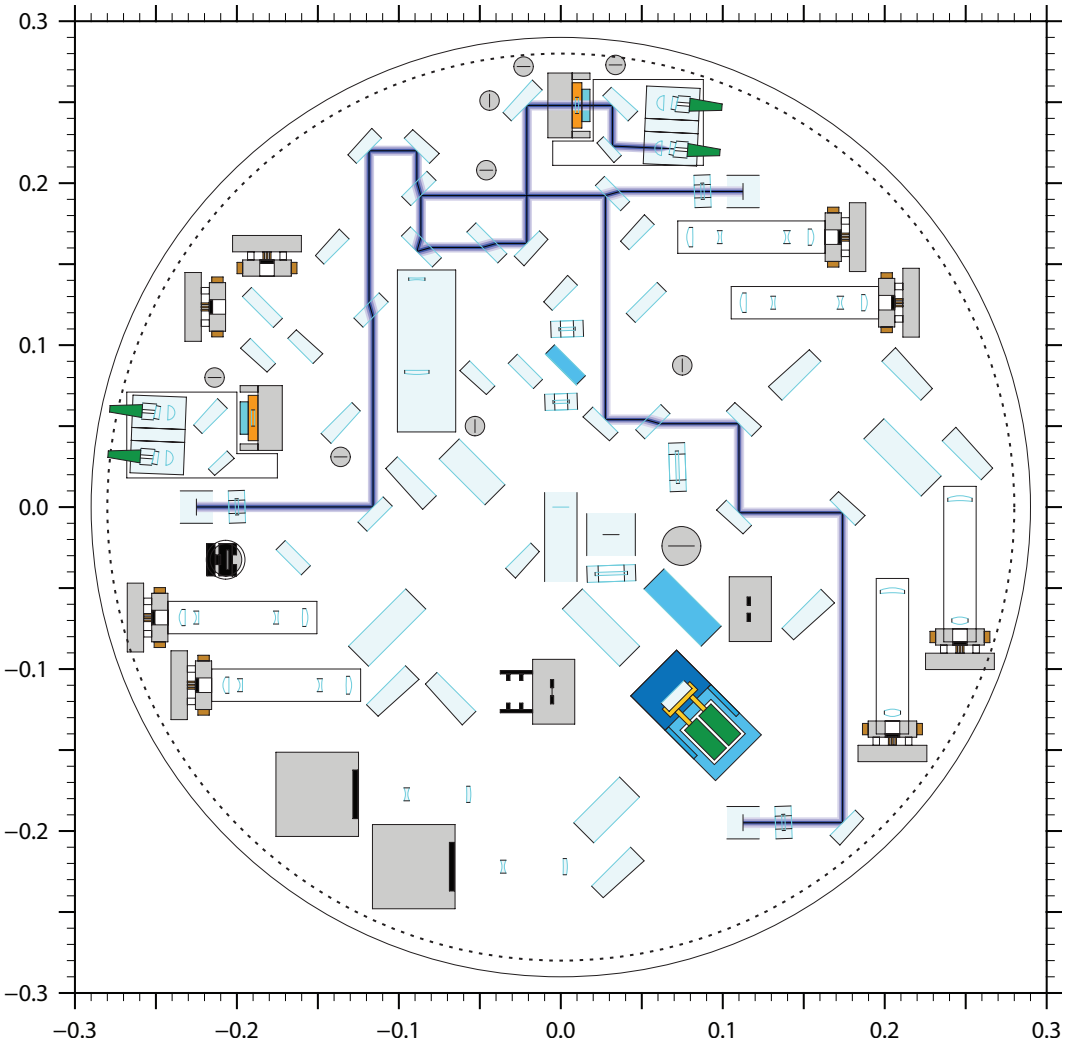

Figure A.8: *OptoCad model of the prototype LISA optical bench showing the path to the three optical truss points. The scale is in metres.*

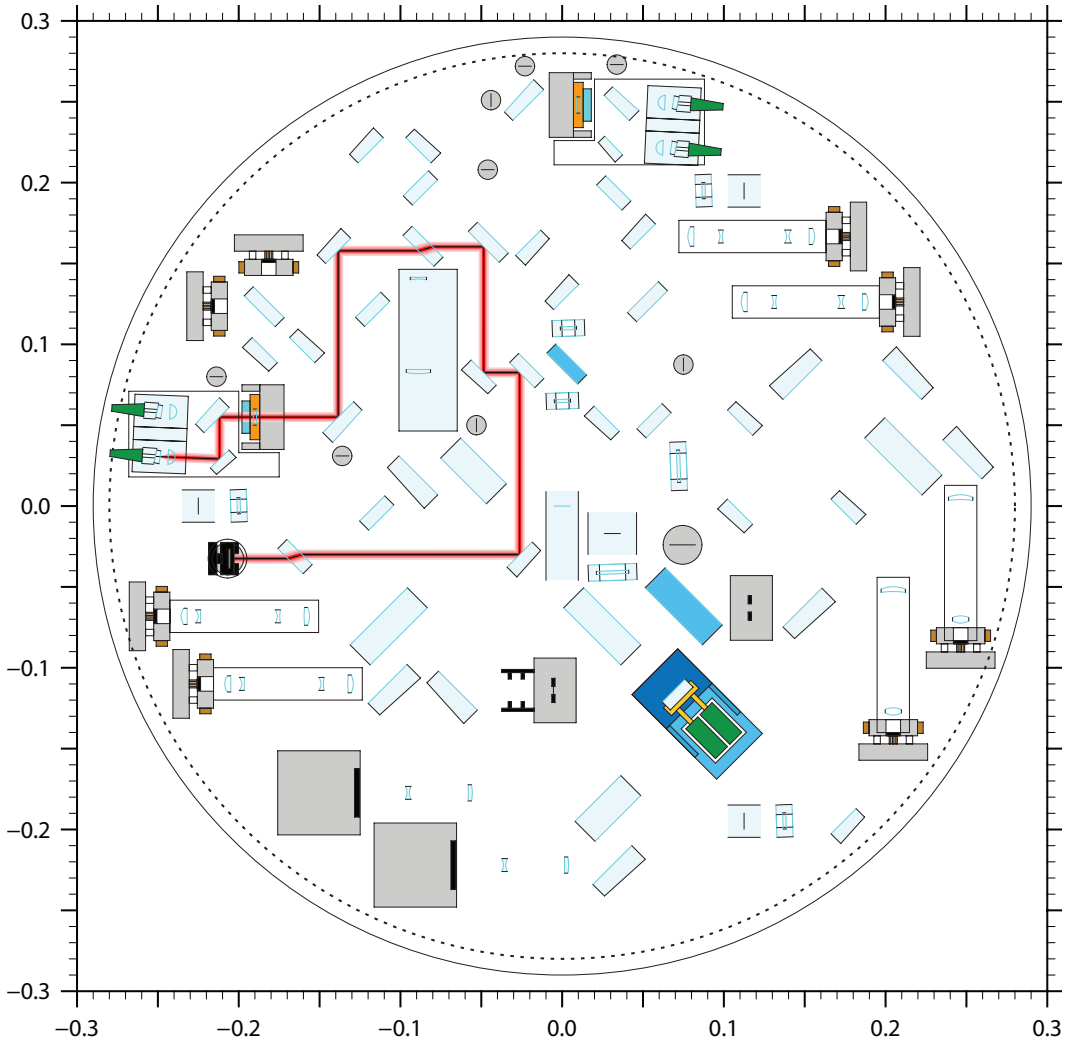

Figure A.9: *OptoCad model of the prototype LISA optical bench showing the Tx beam power monitor. The scale is in metres.*

Bibliography

[1] A. Einstein. *Naherungsweise Integration der Feldgleichungen der Gravitation. Sitzungsber Preuss. Akad. Wiss*, 688, 1916.

[2] Bernard F Schutz. *A first course in general relativity.* Cambridge University Press, 2nd edition, 2009.

[3] B S Sathyaprakash and Bernard F Schutz. *Physics, Astrophysics and Cosmology with Gravitational Waves. Living Reviews in Relativity*, 12(2), 2009.

[4] Bernard F Schutz. *Fundamental physics with LISA. Classical and Quantum Gravity*, 26(9):094020, 2009.

[5] B. Schutz. *Gravitational wave astronomy. Class. Quantum Grav.*, 16:A131–A156, 1999.

[6] Hughes Scott A. *A brief survey of LISA sources and science* laser interferometer space antenna: 6th international lisa symposium. *AIP Conference Proceedings*, 873:13–20, 2006.

[7] B. Abbott et al. *Beating the Spin-Down Limit on Gravitational Wave Emission from the Crab Pulsar. The Astrophysical Journal Letters*, 683(1):L45, 2008.

[8] C W Misner, K S Thorne, and J A Wheeler. *Gravitation*. Freeman, San Francisco, 1973.

[9] Jim Hough, Sheila Rowan, and B S Sathyaprakash. *The search for gravitational waves. Journal of Physics B: Atomic, Molecular and Optical Physics*, 38(9):S497, 2005.

[10] R.A. Hulse and J. H. Taylor. *Discovery of a pulsar in a binary system. Astrophys. J.*, 195:51–53, 1975.

[11] J. Weisberg and J. Taylor. *Relativistic Binary Pulsar B1913+16: Thirty Years of Observations and Analysis. ASP Conferance Series*, 328:25–32, 2004.

[12] J. Weber. *Detection and Generation of Gravitational Waves. Phys. Rev.*, 117:306–313, 1960.

[13] J. Weber. *Evidence for discovery of gravitational radiation. Phys. Rev.*, 22:1320–1324, 1969.

[14] Stanley E Whitcomb. *Ground-based gravitational-wave detection: now and future. Classical and Quantum Gravity*, 25(11):114013, 2008.

[15] B P Abbott et al. *LIGO: the Laser Interferometer Gravitational-Wave Observatory. Reports on Progress in Physics*, 72(7):076901, 2009.

[16] B Abbott et al. *First joint search for gravitational-wave bursts in LIGO and GEO 600 data. Classical and Quantum Gravity*, 25(24):245008, 2008.

[17] K Danzmann. *LISA — an ESA cornerstone mission for the detection and observation of gravitational waves. Adv. Space Res.*, 32:1233–1242, 2003.

[18] GEO600 Project Website, 2010. http://www.geo600.uni-hannover.de/geocurves/.

[19] LIGO Interferometer Sensitivities Website, 2010. http://www.ligo.caltech.edu/~jzweizig/distribution/LSC_Data/.

[20] LIGO Project Document Repository, 2010. https://dcc.ligo.org/cgi-bin/DocDB/ShowDocument?docid=2974.

[21] Shane L. Larson. *JPL LISA noise curve generator*, 2010. http://www.srl.caltech.edu/~shane/sensitivity/.

[22] Leor Barack and Curt Cutler. Confusion noise from lisa capture sources. *Phys. Rev. D*, 70(12):122002, Dec 2004.

[23] Stephen W Hawking et. al. *Three hundred years of gravitation*. Cambridge University Press, 1987.

[24] P McNamara, S Vitale, K Danzmann, and on behalf of the LISA Pathfinder Science Working Team. *LISA Pathfinder. Classical and Quantum Gravity*, 25(11):114034, 2008.

[25] M Armano et al. *LISA Pathfinder: the experiment and the route to LISA. Classical and Quantum Gravity*, 26(9):094001, 2009.

[26] S. Anza and the LTP Team. *The LTP experiment on the LISA Pathfinder mission. Class. Quantum Grav.*, 22:S125–S138, 2005.

[27] C. Killow. *Interferometry Developments for Spaceborne Gravitational Wave Detectors*. PhD Thesis, University of Glasgow, 2006.

[28] David Robertson, Christian Killow, Harry Ward, Jim Hough, Gerhard Heinzel, Antonio García, Vinzenz Wand, Ulrich Johann, and Claus Braxmaier. *LTP interferometer - noise sources and performance. Classical and Quantum Gravity*, 22(10):S155–S163, 2005.

[29] Walter Fichter, Peter Gath, Stefano Vitale, and Daniele Bortoluzzi. *LISA Pathfinder drag-free control and system implications. Classical and Quantum Gravity*, 22(10):S139, 2005.

[30] A Grynagier, W Fichter, and S Vitale. *The LISA Pathfinder drift mode: implementation solutions for a robust algorithm. Classical and Quantum Gravity*, 26(9):094007, 2009.

[31] Euan Morrison, Brian J. Meers, David I. Robertson, and Henry Ward. *Automatic alignment of optical interferometers. Appl. Opt.*, 33(22):5041–5049, 1994.

[32] Euan Morrison, Brian J. Meers, David I. Robertson, and Henry Ward. *Experimental demonstration of an automatic alignment system for optical interferometers. Appl. Opt.*, 33(22):5037–5040, 1994.

[33] G. Heinzel, C. Braxmaier, M. Caldwell, K. Danzmann, F. Draaisma, A. García, J. Hough, O. Jennrich, U. Johann, C. Killow, K. Middleton, M. te Plate, D. Robertson, A. Rüdiger, R. Schilling, F. Steier, V. Wand, and H. Ward. *Successful testing of the LISA Technology Package (LTP) interferometer engineering model. Class. Quantum Grav.*, 22:S149–S154, 2005.

[34] Schott AG., 2010. http://www.schott.com.

[35] Astrium GmbH. *Optical Metrology Subsystem Requirements Specification, ESA Ref: S2-ASD-RS-3010 Issue 3.2*, December 2007.

[36] E. J. Ellife, J. Bogenstahl, A. Deshpande, J. Hough, C. Killow, S. Reid, D. Robertson, S. Rowan, H. Ward, and G. Cagnoli. *Hydroxide-catalysis bonding for stable optical systems for space. Class. Quantum Grav.*, 22:S257–S267, 2005.

[37] Eoin Elliffe. *Aspects of Thermal Noise Modeling in Ground-based Gravitational Wave Detectors and Developments of Hydroxide Catalysis Bonding for Space-based Gravitational Wave Detectors and other Optical Applications*. PhD Thesis, University of Glasgow, 2005.

[38] Felipe Guzmán Cervantes. *Gravitational Wave Observation from Space: optical measurement techniques for LISA and LISA Pathfinder*. PhD Thesis, Leibniz Universität Hannover, 2009.

[39] Roland Schilling. *OptoCad: A Fortran 95 module for tracing Gaussian beams through an optical set-up*, 2010. http://www.rzg.mpg.de/~ros/OptoCad/.

[40] G. Heinzel, V. Wand, A. García, O. Jennrich, C. Braxmaier, D. Robertson, K. Middleton, D. Hoyland, A. Rüdiger, R. Schilling, U. Johann, and K. Danzmann. *The LTP interferometer and phasemeter. Class. Quantum Grav.*, 21:S581–S587, 2004.

[41] R Drever, J Hall, F Kowalski, J Hough, G Ford, A Munley, and H Ward. *Laser phase and frequency stabilization using an optical resonator. Appl. Phys. B*, 31:97–105, 1983.

[42] Frank Steier. *Interferometry techniques for spacebourne gravitational wave detectors*. PhD Thesis, Leibniz Universität Hannover, 2008.

[43] Hexagon Metrology Ltd., 2010. http://www.hexagonmetrology.co.uk/.

[44] Physik Instrumente GmbH, 2010. http://www.physikinstrumente.co.uk/.

[45] HAAS Automation Inc., 2010. http://www.haascnc.com.

[46] H Ward. *OBI - Revised Fibre Injector Design, ESA Ref: S2-UGL-DDD-3004 Issue 1.1*, 2008.

[47] J. Bogenstahl. *Interferometry for the space mission LISA Pathfinder*. PhD Thesis, University of Glasgow, 2010.

[48] D Robertson. *Optical Bench Interferometer Requirements Specification, ESA Ref: S2-UGL-RS-3001 Issue 2.4*, 2009.

[49] Astrium GmbH. *Inertial Sensor Subsystem Requirements Specification, ESA Ref: S2-ASD-RS-3005*, 2007.

[50] Gudrun Wanner. *LTP Alignment Simulation, ESA Ref: S2-AEI-TN-3051 Issue 2*, 2008.

[51] W Folkner, F Hechler, T Sweetser, M Vincent, and P Bender. *LISA orbit selection and stability. Class. Quantum Grav.*, 14:1405–1410, 1997.

[52] O Jennrich. *LISA technology and instrumentation. Classical and Quantum Gravity*, 26(15):153001, 2009.

[53] D A Shaddock. *Space-based gravitational wave detection with LISA. Classical and Quantum Gravity*, 25(11):114012, 2008.

[54] James Ira Thorpe. *LISA long-arm interferometry. Classical and Quantum Gravity*, 27(8):084008, 2010.

[55] G Heinzel, C Braxmaier, K Danzmann, P Gath, J Hough, O Jennrich, U Johann, A Rüdiger, M Sallusti, and H Schulte. *LISA interferometry: recent developments. Classical and Quantum Gravity*, 23(8):S119, 2006.

[56] Volker Leonhardt and Jordan B. Camp. *Space interferometry application of laser frequency stabilization with molecular iodine. Appl. Opt.*, 45(17):4142–4146, 2006.

[57] D Weise. *OB Requirements Specification and Justification, ESA Ref: LOB-ASD-TN-006 Issue 0.3*, 2010.

[58] M Sallusti, P Gath, D Weise, M Berger, and H R Schulte. *LISA system design highlights. Classical and Quantum Gravity*, 26(9):094015, 2009.